

**MAJORANA FERMION IN TOPOLOGICAL
SUPERCONDUCTOR AND MOTT-SUPERFLUID
TRANSITION IN CIRCUIT-QED SYSTEM**

JIA-BIN YOU

NATIONAL UNIVERSITY OF SINGAPORE

2015

**MAJORANA FERMION IN TOPOLOGICAL
SUPERCONDUCTOR AND MOTT-SUPERFLUID
TRANSITION IN CIRCUIT-QED SYSTEM**

JIA-BIN YOU

(M.Sc., XMU)

**CENTRE FOR QUANTUM TECHNOLOGIES
NATIONAL UNIVERSITY OF SINGAPORE**

**A THESIS SUBMITTED FOR THE DEGREE OF
DOCTOR OF PHILOSOPHY**

2015

Declaration

I hereby declare that the thesis is my original work and it has been written by me in its entirety. I have duly acknowledged all the sources of information which have been used in the thesis.

This thesis has also not been submitted for any degree in any university previously.

Jia-Bin You

September 1, 2015

Acknowledgements

I would like to thank my colleagues, friends, and family for their continued support throughout my PhD candidature. Especially, I would like to express my deepest appreciation to my supervisor, Professor Oh Choo Hiap, for giving me the chance to live and study in this beautiful country, and for all his help and guidance during the completion of this research. I also thank Professor Vlatko Vedral for his collaborations and useful advice as my co-supervisor at Centre for Quantum Technologies. Additionally, I would like to acknowledge the members of my Thesis Advisory Committee, Professor Lai Choy Heng, Vlatko Vedral and Phil Chan, for their academic advice during my qualifying exam. The works in this thesis have been funded by the CQT Scholarship, and the National Research Foundation and Ministry of Education of Singapore.

I have benefited tremendously from discussing physics with other colleagues and friends at Centre for Quantum Technologies and Department of Physics. Interactions with them are always enlightening and fruitful. A very partial list includes Chen Qing, Cui Jian, Deng Donglin, Feng Xunli, Guo Chu, Huang Jinsong, Lee Hsin-Han, Li Ying, Lu Xiaoming, Luo Ziyu, Luo Yongzheng, Mei Feng, Nie Wei, Peng Jiebin, Qian Jun, Qiao Youming, Shao Xiaoqiang, Sun Chunfang, Tang Weidong, Tian Guojing, Tong Qingjun, Wang Hui, Wang Yibo, Wang Zhuo, Wu Chunfeng, Yang Wanli, Yao Penghui, Yu Liwei, Yu Sixia, Zeng Shengwei, Zhang Yixing, Zhu Huangjun. I also wish to thank them and many others for enriching my graduate life.

Contents

Contents	iii
Abstract	v
1 Introduction	1
I Majorana fermion in topological superconductor	5
2 Topological quantum phase transition in spin-singlet superconductor	6
2.1 Introduction	6
2.2 Theoretical model for the spin-singlet topological superconductor	8
2.3 <i>s</i> -wave Rashba superconductor	9
2.4 <i>s</i> -wave Dresselhaus superconductor	12
2.5 Topological properties of the spin-singlet superconductor	18
2.5.1 symmetries of the BdG Hamiltonian	18
2.5.2 topological invariants of the BdG Hamiltonian	19
2.5.3 phase diagrams of the BdG Hamiltonian	24
2.5.4 Majorana bound states at the edge of the BdG Hamiltonian	25
3 Majorana transport in superconducting nanowire with Rashba and Dresselhaus spin-orbit couplings	31
3.1 Introduction	31
3.2 Model	33
3.3 NEGF method for the Majorana current	36
3.3.1 general formula	36
3.3.2 <i>dc</i> current response	40
3.3.3 <i>ac</i> current response	43

3.4	Interaction and disorder effects on the Majorana transport	43
3.4.1	brief introduction of bosonization	46
3.4.1.1	left and right movers representation	46
3.4.1.2	bosonization of the Majorana nanowire	51
3.4.2	influence on the Majorana transport	52
II	Mott-superfluid transition in hybrid circuit-QED system	55
4	Phase transition of light in circuit-QED lattices coupled to nitrogen-vacancy centers in diamond	56
4.1	Introduction	56
4.2	Model	57
4.3	Mott-superfluid transition	62
4.4	Dissipative effects	67
4.5	Experimental feasibility	68
5	Summary and outlook	70
A	Edge spectra of topological superconductor with mixed spin-singlet pairings	72
B	Keldysh non-equilibrium Green function	76
C	Green function and self-energy for Majorana nanowire	80
D	Useful expressions for the free Green functions	84
E	Fermion-boson correspondence in one dimension	86
F	Normal-ordered density operator	90
G	Replica method	92
H	Renormalization analysis of correlation function	94
I	Quantum trajectory method	99
	Bibliography	101

Abstract

The thesis contains two parts. Part [I](#) comprises two chapters and concerns Majorana fermion in topological superconductors. Part [II](#) is a study of Mott-superfluid transition in hybrid circuit-QED system.

In Part [I](#), we study the Majorana fermion and its transport in the topological superconductors. In Chapter [2](#), we investigate the edge states and the vortex core states in the spin-singlet (*s*-wave and *d*-wave) superconductor with Rashba and Dresselhaus (110) spin-orbit couplings. We show that there are several topological invariants in the Bogoliubov-de Gennes (BdG) Hamiltonian by symmetry analysis. The edge spectrum of the superconductors is either Dirac cone or flat band which supports the emergence of the Majorana fermion. For the Majorana flat bands, an edge index, namely the Pfaffian invariant $\mathcal{P}(k_y)$ or the winding number $\mathcal{W}(k_y)$, is needed to make them topologically stable. In Chapter [3](#), we use Keldysh non-equilibrium Green function method to study the two-lead tunneling in the superconducting nanowire with Rashba and Dresselhaus spin-orbit couplings. The *dc* and *ac* current responses of the nanowire are considered. Interestingly, due to the exotic property of Majorana fermion, there exists a hole transmission channel which makes the currents asymmetric at the left and right leads. We employ the bosonization and renormalization group method to study the phase diagram of the wire with Coulomb interaction and disorder and discuss the impact on the transport property.

In Part [II](#) (Chapter [4](#)), we propose a hybrid quantum architecture for engineering a photonic Mott insulator-superfluid phase transition in a two-dimensional square lattice of a superconducting transmission line resonator coupled to a single nitrogen-vacancy center encircled by a persistent current qubit. The phase diagrams in the case of real-value and complex-value photonic hopping are obtained using the mean-field approach. Also, the quantum jump technique is employed to describe the phase diagram when the dissipative effects are considered.

Publications

1. Jia-Bin You, Xiao-Qiang Shao, Qing-Jun Tong, A. H. Chan, C. H. Oh, and Vlatko Vedral, *Majorana transport in superconducting nanowire with Rashba and Dresselhaus spin-orbit couplings*. Journal of Physics: Condensed Matter **27**, 225302 (2015).
2. Jia-Bin You, W. L. Yang, Zhen-Yu Xu, A. H. Chan, and C. H. Oh, *Phase transition of light in circuit-QED lattices coupled to nitrogen-vacancy centers in diamond*. Physical Review B **90**, 195112 (2014).
3. Jia-Bin You, A. H. Chan, C. H. Oh and Vlatko Vedral, *Topological quantum phase transitions in the spin-singlet superconductor with Rashba and Dresselhaus (110) spin-orbit couplings*. Annals of Physics **349**, 189 (2014).
4. Jia-Bin You, C. H. Oh and Vlatko Vedral, *Majorana fermions in s-wave noncentrosymmetric superconductor with Dresselhaus (110) spin-orbit coupling*. Physical Review B **87**, 054501 (2013).

Chapter 1

Introduction

The thesis contains two parts. The first part (Chapter 2 and 3) concerns Majorana fermions in two dimensional and one dimensional topological superconductors. The second part (Chapter 4) concerns Mott insulator-superfluid transition in hybrid circuit quantum electrodynamics (QED) system.

In Chapter 2, we study the topological phase in the Rashba and Dresselhaus spin-singlet superconductors. It is amazing that the various phases in our world can be understood systematically by Landau symmetry breaking theory. However, in the last several decades, it was discovered that there are even more interesting phases that are beyond Landau symmetry breaking theory [163]. One of these new phases is topological superconductor which is new state of quantum matter that is characterized by topological order such as Chern number or Pfaffian invariant [3; 4; 14; 33; 45; 66; 79; 88; 125; 131; 132; 134; 139; 146; 166]. The topologically ordered phases have a full superconducting gap in the bulk and localized states in the edge or surface. Interestingly, these localized edge states can host Majorana fermions which are neutral particles that are their own antiparticles [45; 104; 119; 125; 131]. The solid-state Majorana fermions can be used for a topological quantum computer, in which the non-Abelian exchange statistics of the Majorana fermions are used to process quantum information nonlocally, evading error-inducing local perturbations [29; 40; 79; 113]. In this Chapter, we investigate the edge states and the vortex core states in the s -wave superconductor with Rashba and Dresselhaus (110) spin-orbit couplings. Particularly, we demonstrate that there exists a semimetal phase characterized by the dispersionless Majorana flat bands in the phase diagram of the s -wave Dresselhaus superconductor which supports the emergence of Majorana fermions. We then extend our study to the spin-singlet (s -wave and d -wave) superconductor with Rashba and Dresselhaus (110) spin-orbit couplings. We show that there are several topo-

logical invariants in the Bogoliubov-de Gennes (BdG) Hamiltonian by symmetry analysis. The Pfaffian invariant \mathcal{P} for the particle-hole symmetry can be used to demonstrate all the possible phase diagrams of the BdG Hamiltonian. We find that the edge spectrum is either Dirac cone or flat band which supports the emergence of the Majorana fermion. For the Majorana flat bands, an edge index, namely the Pfaffian invariant $\mathcal{P}(k_y)$ or the winding number $\mathcal{W}(k_y)$, is needed to make them topologically stable. These edge indices can also be used in determining the location of the Majorana flat bands. The main results of this Chapter were published in our following papers:

- Jia-Bin You, C. H. Oh and Vlatko Vedral, *Majorana fermions in s-wave noncentrosymmetric superconductor with Dresselhaus (110) spin-orbit coupling*. Physical Review B **87**, 054501 (2013).
- Jia-Bin You, A. H. Chan, C. H. Oh and Vlatko Vedral, *Topological quantum phase transitions in the spin-singlet superconductor with Rashba and Dresselhaus (110) spin-orbit couplings*. Annals of Physics **349**, 189 (2014).

In Chapter 3, we use Keldysh non-equilibrium Green function method to study two-lead tunneling in superconducting nanowire with Rashba and Dresselhaus spin-orbit couplings [12; 30; 32; 36; 42; 71; 86; 100; 106; 173; 175]. The tunneling spectroscopy is a key probe for detecting Majorana fermions [40; 42; 90; 122; 135; 142]. The Majorana fermions would manifest as a conductance peak at zero voltage as long as they are spatially separated from each other. Indeed, numerous experimental results have reported zero-bias conductance peak in devices inspired by the theoretical proposals [19; 23; 27; 28; 31; 40; 91; 109]. In this Chapter, we first study the zero-bias *dc* conductance peak appearing in our two-lead setup. Interestingly, due to the exotic property of Majorana fermion, there exists a hole transmission channel which makes the currents asymmetric at the left and right leads. The *ac* current response mediated by Majorana fermion is also studied in the thesis. To discuss the impacts of Coulomb interaction and disorder on the transport property of Majorana nanowire, we use the renormalization group method to study the phase diagram of the wire. It is found that there is a topological phase transition under the interplay of superconductivity and disorder. We find that the Majorana transport is preserved in the superconducting-dominated topological phase and destroyed in the disorder-dominated non-topological insulator phase. The main results of this Chapter are from the following paper:

- Jia-Bin You, Xiao-Qiang Shao, Qing-Jun Tong, A. H. Chan, C. H. Oh, and Vlatko Vedral, *Majorana transport in superconducting nanowire with Rashba and Dres-*

selhaus spin-orbit couplings. Journal of Physics: Condensed Matter **27**, 225302 (2015).

In Part II (Chapter 4), we study the Mott insulator-superfluid transition in the hybrid circuit-QED system. The circuit-QED [93; 124; 138; 167] is implemented by combining microwave resonators and superconducting qubits on a microchip with unprecedented experimental control. These circuits are fabricated with optical and electron-beam lithography and can therefore access a wide range of geometries for large-scale quantum simulators [34; 55; 65; 81; 98; 103; 114; 118; 151; 153]. Moreover, because the particles being simulated are just circuit excitations, particle number is not necessarily conserved. Unavoidable photon loss, coupled with the ease of feeding in additional photons through continuous external driving, makes such lattices open quantum systems, which can be studied in a non-equilibrium steady state [16; 123]. Due to the genuine openness of photonic systems, circuit-QED lattices offer the possibility to study the intricate interplay of collective behavior, strong correlations and non-equilibrium physics. Thus, turning circuit-QED into an architecture for quantum simulation, i.e., using a well-controlled system to mimic the intricate quantum behavior of another system is an exciting idea and now also catching on in experiments [22; 50; 65; 73; 160]. In this Chapter, we propose a hybrid quantum architecture for engineering a photonic Mott insulator-superfluid phase transition in a two-dimensional square lattice of a superconducting transmission line resonator (TLR) coupled to a single nitrogen-vacancy center encircled by a persistent current qubit. The main results of this Chapter already appeared in the following paper:

- Jia-Bin You, W. L. Yang, Zhen-Yu Xu, A. H. Chan, and C. H. Oh, *Phase transition of light in circuit-QED lattices coupled to nitrogen-vacancy centers in diamond*. Physical Review B **90**, 195112 (2014).

For the photonic Mott insulator-superfluid transition, each circuit excitation is spread out over the entire lattice in the superfluid phase with long-range phase coherence. But in the insulating phase, exact numbers of circuit excitations are localized at individual lattice sites, with no phase coherence across the lattice [57]. This localization-delocalization transition results from the interplay between the on-site repulsion and the nonlocal tunneling. The phase boundary in the case of real-value and complex-value photon hoppings can be obtained using the mean-field approach. Also, the quantum jump technique is employed to describe the phase diagram when the dissipative effects are considered [16; 123]. The unique feature of our architecture is the good tunability of effective on-site repulsion and photon-hopping rate [38; 94], and the local statistical property of TLRs which can

be analyzed readily using present microwave techniques [43; 74; 92; 141; 144; 149]. Our work gives new perspectives in quantum simulation of condensed-matter and many-body physics using a hybrid circuit-QED system. The experimental challenges are realizable using current technologies.

Part I

Majorana fermion in topological superconductor

Chapter 2

Topological quantum phase transition in spin-singlet superconductor

2.1 Introduction

Topological phase of condensed matter systems refers to a quantum many-body state with nontrivial topology in the momentum or coordinate space [3; 8; 45; 46; 58; 66; 76; 77; 83; 119; 125; 129; 131; 134; 147; 148; 158]. Recent newly discovered topological superconductor (TSC) has spawned considerable interests since this kind of topological phase supports the emergence of Majorana fermion (MF) [45; 104; 119; 125; 131] which is a promising candidate for the fault-tolerant topological quantum computation [80]. There are several proposals for hosting MFs in TSC, for example, chiral p -wave superconductor [125], Cu-doped topological insulator Bi_2Se_3 [66], superconducting proximity devices [3; 4; 45; 79; 88; 134] and noncentrosymmetric superconductor such as CePt_3Si and $\text{Li}_2\text{Pd}_x\text{Pt}_{3-x}\text{B}$ [14; 33; 131; 132; 139; 146; 166]. The signatures of MFs have also been reported in the transport measurement of superconducting InSb nanowire [28; 109], $\text{Cu}_x\text{Bi}_2\text{Se}_3$ [7; 127] and topological insulator Josephson junction [164].

There are two kinds of gapless edge states in the topological superconductor. One is a Dirac cone, the other is a flat band, namely, dispersionless zero-energy state [14; 33; 88; 132; 139; 166; 170]. The Dirac cone can be found in the fully gapped topological superconductors when the Chern number of the occupied energy bands is nonzero. However, the flat band can appear in the gapless topological superconductors which, apart from

the particle-hole symmetry, have some extra symmetries in the Hamiltonian. Such flat bands are known to occur at the zigzag and bearded edge in graphene [110], in the non-centrosymmetric superconductor [14; 132; 139] and in other systems with topologically stable Dirac points [159].

In Sec. 2.2, we give a model for the spin-singlet superconductor with Rashba and Dresselhaus (110) spin-orbit (SO) couplings. In Sec. 2.3, we briefly discuss the topological number and the edge spectrum of the s -wave Rashba superconductor. In Sec. 2.4, we focus on the topological phase and the Majorana fermion at the edge and in the vortex core of the s -wave Dresselhaus superconductor. Interestingly, we find that there is a novel semimetal phase in the Dresselhaus superconductor, where the energy gap closes and different kinds of flat band emerge. We demonstrate that these flat bands support the emergence of MFs analytically and numerically. It is known that the Chern number is not a well-defined topological invariant in the gapless energy-band structure, however, we find that the topologically different semimetal phases can still be distinguished by the Pfaffian invariant of the particle-hole symmetric Hamiltonian.

In Sec. 2.5, we generalize our study to the spin-singlet superconductor with the Rashba and Dresselhaus (110) spin-orbit couplings. We focus on the Hamiltonian with spin-orbit coupling of Dresselhaus (110) type which is a gapless topological system containing two kinds of edge states mentioned above. For the topological numbers of the Hamiltonian of the spin-singlet superconductor, the Bogoliubov-de Gennes (BdG) Hamiltonian of the superconductor is particle-hole symmetric so that we can associate a Pfaffian invariant \mathcal{P} with it as a topological invariant of the system. In particular, the Pfaffian invariant \mathcal{P} can be used in distinguishing the topologically nontrivial phase from the trivial one and we find all the possible phase diagrams of the BdG Hamiltonian in Sec. 2.5.3. The nontrivial topological phase in this BdG Hamiltonian is Majorana type which can be exploited for implementing the fault-tolerant topological quantum computing schemes [79; 113]. Furthermore, we find that the BdG Hamiltonian can have partial particle-hole symmetry and chiral symmetry which can be used to define the one dimensional Pfaffian invariant $\mathcal{P}(k_y)$ and the winding number $\mathcal{W}(k_y)$. Interestingly, we find that the Pfaffian invariant $\mathcal{P}(k_y)$ or the winding number $\mathcal{W}(k_y)$ can be used as a topological index in determining the location of the zero-energy Majorana flat bands.

The main results of this chapter were published in the following two papers:

- Jia-Bin You, C. H. Oh and Vlatko Vedral, *Majorana fermions in s -wave noncentrosymmetric superconductor with Dresselhaus (110) spin-orbit coupling*. Physical Review B **87**, 054501 (2013);

- Jia-Bin You, A. H. Chan, C. H. Oh and Vlatko Vedral, *Topological quantum phase transitions in the spin-singlet superconductor with Rashba and Dresselhaus (110) spin-orbit couplings*. *Annals of Physics* **349**, 189 (2014).

2.2 Theoretical model for the spin-singlet topological superconductor

We begin with modeling Hamiltonian of a two dimensional spin-singlet superconductor on a square lattice, the hopping term is

$$H_{\text{kin}} = -t \sum_{is} \sum_{\hat{\nu}=\hat{x},\hat{y}} (c_{i+\hat{\nu}s}^\dagger c_{is} + c_{i-\hat{\nu}s}^\dagger c_{is}) - \mu \sum_{is} c_{is}^\dagger c_{is}, \quad (2.1)$$

where c_{is}^\dagger (c_{is}) is the creation (annihilation) operator of the electron with spin $s = (\uparrow, \downarrow)$ at site $i = (i_x, i_y)$, \hat{x} (\hat{y}) is the unit vector in the x (y) direction, t is the hopping amplitude and μ is the chemical potential. For the spin-singlet superconductor, we study the s -wave and d -wave pairings in this thesis. The s -wave superconducting term in the square lattice is

$$H_s = \sum_i [(\Delta_{s_1} + i\Delta_{s_2})c_{i\uparrow}^\dagger c_{i\downarrow}^\dagger + \text{H.c.}]. \quad (2.2)$$

Similarly, the d -wave superconducting term is

$$H_d = \sum_i \left[\frac{\Delta_{d_1}}{2} (c_{i-\hat{y}\uparrow}^\dagger c_{i\downarrow}^\dagger + c_{i+\hat{y}\uparrow}^\dagger c_{i\downarrow}^\dagger - c_{i-\hat{x}\uparrow}^\dagger c_{i\downarrow}^\dagger - c_{i+\hat{x}\uparrow}^\dagger c_{i\downarrow}^\dagger) \right. \\ \left. + i \frac{\Delta_{d_2}}{4} (c_{i-\hat{x}+\hat{y}\uparrow}^\dagger c_{i\downarrow}^\dagger + c_{i+\hat{x}-\hat{y}\uparrow}^\dagger c_{i\downarrow}^\dagger - c_{i+\hat{x}+\hat{y}\uparrow}^\dagger c_{i\downarrow}^\dagger - c_{i-\hat{x}-\hat{y}\uparrow}^\dagger c_{i\downarrow}^\dagger) + \text{H.c.} \right]. \quad (2.3)$$

We assume that all the superconducting gaps Δ_{s_1} , Δ_{s_2} , Δ_{d_1} and Δ_{d_2} are uniform in the whole superconductor. The spin-orbit couplings can arise from structure inversion asymmetry of a confinement potential (e.g., external electric field) or bulk inversion asymmetry of an underlying crystal (e.g., the zinc blende structure) [165]. These two kinds of asymmetries lead to the well-known Rashba and Dresselhaus spin-orbit couplings. The Rashba spin-orbit coupling in the square lattice is of the form

$$H_R = -\frac{\alpha}{2} \sum_i [(c_{i-\hat{x}\downarrow}^\dagger c_{i\uparrow} - c_{i+\hat{x}\downarrow}^\dagger c_{i\uparrow}) + i(c_{i-\hat{y}\downarrow}^\dagger c_{i\uparrow} - c_{i+\hat{y}\downarrow}^\dagger c_{i\uparrow}) + \text{H.c.}], \quad (2.4)$$

where α is the coupling strength of the Rashba spin-orbit coupling. The Dresselhaus (110) spin-orbit coupling is formulated as

$$H_D^{110} = -i\frac{\beta}{2} \sum_{iss'} (\tau_z)_{ss'} (c_{i-\hat{x}s}^\dagger c_{is'} - c_{i+\hat{x}s}^\dagger c_{is'}), \quad (2.5)$$

where β is the coupling strength for the Dresselhaus (110) spin-orbit coupling. (110) is the common-used Miller index. We also apply an arbitrary magnetic field to the superconductor. Neglecting the orbital effect of the magnetic field \mathbf{B} , we consider the Zeeman effect as

$$H_Z = \sum_{iss'} (\mathbf{V} \cdot \boldsymbol{\tau})_{ss'} c_{is}^\dagger c_{is'}, \quad (2.6)$$

where $\mathbf{V} = \frac{g\mu_B}{2}(B_x, B_y, B_z) \equiv (V_x, V_y, V_z)$ and $\boldsymbol{\tau} = (\tau_x, \tau_y, \tau_z)$ are Pauli matrices operating on spin space. Here μ_B is the Bohr magneton and g is the Landé g -factor. Therefore, the spin-singlet superconductor with the Rashba and Dresselhaus (110) spin-orbit couplings in an arbitrary magnetic field is dictated by the Hamiltonian $H = H_{\text{kin}} + H_s + H_d + H_R + H_D^{110} + H_Z$. In the momentum space, the Hamiltonian is recast into $H = \frac{1}{2} \sum_{\mathbf{k}} \psi_{\mathbf{k}}^\dagger \mathcal{H}(\mathbf{k}) \psi_{\mathbf{k}}$ with $\psi_{\mathbf{k}}^\dagger = (c_{\mathbf{k}\uparrow}^\dagger, c_{\mathbf{k}\downarrow}^\dagger, c_{-\mathbf{k}\uparrow}, c_{-\mathbf{k}\downarrow})$ where $c_{\mathbf{k}s}^\dagger = (1/\sqrt{N}) \sum_{\mathbf{l}} e^{i\mathbf{k}\cdot\mathbf{l}} c_{\mathbf{l}s}^\dagger$, $\mathbf{k} = (k_x, k_y)$, $\mathbf{l} = (l_x, l_y)$ and N is the number of unit cells in the lattice. After some calculations, the Bogoliubov-de Gennes Hamiltonian for the superconductor is

$$\mathcal{H}(\mathbf{k}) = \begin{bmatrix} \xi(\mathbf{k}) + (\mathcal{L}(\mathbf{k}) + \mathbf{V}) \cdot \boldsymbol{\tau} & i\Delta(\mathbf{k})\tau_y \\ -i\Delta^*(\mathbf{k})\tau_y & -\xi(\mathbf{k}) + (\mathcal{L}(\mathbf{k}) - \mathbf{V}) \cdot \boldsymbol{\tau}^* \end{bmatrix}, \quad (2.7)$$

where $\xi(\mathbf{k}) = -2t(\cos k_x + \cos k_y) - \mu$, $\Delta(\mathbf{k}) = (\Delta_{s_1} + i\Delta_{s_2}) + [\Delta_{d_1}(\cos k_y - \cos k_x) + i\Delta_{d_2} \sin k_x \sin k_y]$ and $\mathcal{L}(\mathbf{k}) = (\alpha \sin k_y, -\alpha \sin k_x, \beta \sin k_x)$.

2.3 s -wave Rashba superconductor

As a prototype, we first consider the s -wave superconductor with Rashba spin-orbit coupling in a perpendicular magnetic field. The imaginary part of the s -wave pairing Δ_{s_2} does not have significant effect on the edge spectrum, thus here we set $\Delta_{s_2} = 0$. The Hamiltonian is $H = H_{\text{kin}} + H_s + H_R + H_Z$, where $\mathbf{V} = (0, 0, V_z)$. In the momentum space,

the Bogoliubov-de Gennes Hamiltonian is given by

$$\mathcal{H}(\mathbf{k}) = \xi(\mathbf{k})\sigma_z + \alpha \sin k_y \tau_x - \alpha \sin k_x \sigma_z \tau_y + V_z \sigma_z \tau_z - \Delta_{s_1} \sigma_y \tau_y, \quad (2.8)$$

where $\sigma = (\sigma_x, \sigma_y, \sigma_z)$ are the Pauli matrices operating on the particle-hole space.

We can use the Chern number to characterize the nontrivial topology of the Rashba superconductor. The Chern number defined for the fully gapped Hamiltonian is

$$\mathcal{C} = \frac{1}{2\pi} \int_{T^2} dk_x dk_y \mathcal{F}(\mathbf{k}), \quad (2.9)$$

where $\mathcal{F}(\mathbf{k}) = \partial_{k_x} A_y(\mathbf{k}) - \partial_{k_y} A_x(\mathbf{k})$ is the strength of the gauge field $A_j(\mathbf{k}) = i \sum_{n=occ.} \langle \psi_n(\mathbf{k}) | \partial_{k_j} \psi_n(\mathbf{k}) \rangle (j = x, y)$ and $\psi_n(\mathbf{k})$ are the eigenstates of the Hamiltonian. The integral is carried out in the first Brillouin zone T^2 and the summation is carried out for the occupied states. We say the topological quantum phase transition does not happen if the Chern number remains unchanged. Since the topological quantum phase transition happens when the energy gap closes, the phase diagram of Rashba superconductor can be obtained by studying the gap-closing condition of the BdG Hamiltonian Eq. (2.8). We diagonalize the BdG Hamiltonian and find that the energy spectra are

$$E(\mathbf{k}) = \pm \sqrt{\xi^2(\mathbf{k}) + \mathcal{L}^2(\mathbf{k}) + V_z^2 + \Delta_{s_1}^2 \pm 2\sqrt{\xi^2(\mathbf{k})\mathcal{L}^2(\mathbf{k}) + V_z^2(\xi^2(\mathbf{k}) + \Delta_{s_1}^2)}}, \quad (2.10)$$

where $\mathcal{L}^2(\mathbf{k}) = \alpha^2(\sin^2 k_x + \sin^2 k_y)$. Therefore, we can find that the energy gap closes at

$$\xi^2(\mathbf{k}) + \mathcal{L}^2(\mathbf{k}) + V_z^2 + \Delta_{s_1}^2 = 2\sqrt{\xi^2(\mathbf{k})\mathcal{L}^2(\mathbf{k}) + V_z^2(\xi^2(\mathbf{k}) + \Delta_{s_1}^2)}. \quad (2.11)$$

After some straightforward calculations, we find that the gap closes at $(k_x, k_y) = (0, 0), (0, \pi), (\pi, 0), (\pi, \pi)$ when $(\mu \pm 4t)^2 + \Delta_{s_1}^2 = V_z^2$ or $\mu^2 + \Delta_{s_1}^2 = V_z^2$. The phase diagram is depicted in Fig. 2.1(a) and the Chern number is attached to each region of the phase diagram.

To study the edge spectra of the topological superconductor, we can diagonalize the general Hamiltonian $H = H_{\text{kin}} + H_s + H_d + H_R + H_D^{110} + H_Z$ in the boundary conditions of x -direction to be open and y to be periodic. By the partial Fourier transform $c_{l_x, k_y, s}^\dagger = (1/\sqrt{N_y}) \sum_{l_y} e^{ik_y l_y} c_{l_x, l_y, s}^\dagger$, we can write the Hamiltonian in the basis of $\psi_{k_y}^\dagger = (c_{1, k_y, \uparrow}^\dagger, c_{1, -k_y, \downarrow}, c_{1, k_y, \downarrow}^\dagger, c_{1, -k_y, \uparrow}, \dots, c_{N_x, k_y, \uparrow}^\dagger, c_{N_x, -k_y, \downarrow}, c_{N_x, k_y, \downarrow}^\dagger, c_{N_x, -k_y, \uparrow})$ where $N_x(y)$ is the number of unit cells in the $x(y)$ -direction and k_y is the momentum in the y -direction.

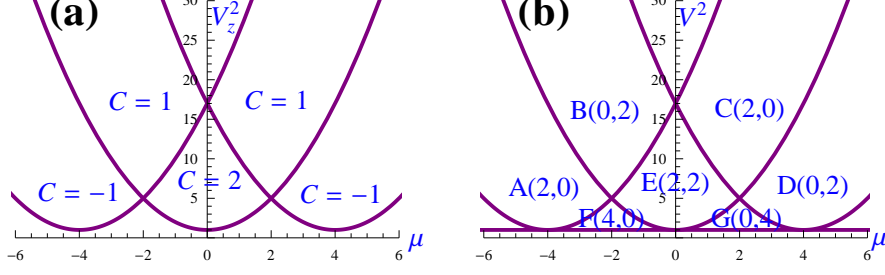


Figure 2.1: The phase diagrams of the s -wave (a) Rashba and (b) Dresselhaus superconductor. The parameters are $t = 1$ and $\Delta_{s_1} = 1$. In (b), $V^2 = V_x^2 + V_y^2$. The Chern number in different regions is indicated in (a). The number of gap-closing points at $k_x = 0$ and $k_x = \pi$ in different regions of the phase diagram are also shown as a pair (ν_1, ν_2) in (b).

The Hamiltonian in this cylindrical symmetry is $H = \frac{1}{2} \sum_{k_y} \psi_{k_y}^\dagger H(k_y) \psi_{k_y}$, where

$$H(k_y) = \begin{bmatrix} A & B & & & \\ B^\dagger & A & B & & \\ & B^\dagger & A & B & \\ & & B^\dagger & A & \dots \\ & & & \dots & \dots \end{bmatrix}. \quad (2.12)$$

Here

$$A = \begin{bmatrix} -2t \cos k_y - \mu + V_z & \Delta_{s_1} + i\Delta_{s_2} + \Delta_{d_1} \cos k_y & V_x - iV_y + \alpha \sin k_y & 0 \\ \Delta_{s_1} - i\Delta_{s_2} + \Delta_{d_1} \cos k_y & 2t \cos k_y + \mu + V_z & 0 & -V_x + iV_y + \alpha \sin k_y \\ V_x + iV_y + \alpha \sin k_y & 0 & -2t \cos k_y - \mu - V_z & -\Delta_{s_1} - i\Delta_{s_2} - \Delta_{d_1} \cos k_y \\ 0 & -V_x - iV_y + \alpha \sin k_y & -\Delta_{s_1} + i\Delta_{s_2} - \Delta_{d_1} \cos k_y & 2t \cos k_y + \mu - V_z \end{bmatrix} \quad (2.13)$$

and

$$B = \begin{bmatrix} -t - i\beta/2 & -(\Delta_{d_1} - \Delta_{d_2} \sin k_y)/2 & \alpha/2 & 0 \\ -(\Delta_{d_1} + \Delta_{d_2} \sin k_y)/2 & t + i\beta/2 & 0 & \alpha/2 \\ -\alpha/2 & 0 & -t + i\beta/2 & (\Delta_{d_1} - \Delta_{d_2} \sin k_y)/2 \\ 0 & -\alpha/2 & (\Delta_{d_1} + \Delta_{d_2} \sin k_y)/2 & t - i\beta/2 \end{bmatrix}. \quad (2.14)$$

For the Rashba superconductor Eq. (2.8), we diagonalize the Hamiltonian Eq. (2.12) by setting $\beta = 0$, $\Delta_{d_1} = \Delta_{d_2} = 0$ and $V_x = V_y = 0$, and obtain the edge spectra of the Hamiltonian as shown in Fig. 2.2. It is easy to check that the number of Dirac cones in the edge Brillouin zone is consistent with the Chern number in the corresponding regions of the phase diagram in Fig. 2.1(a).

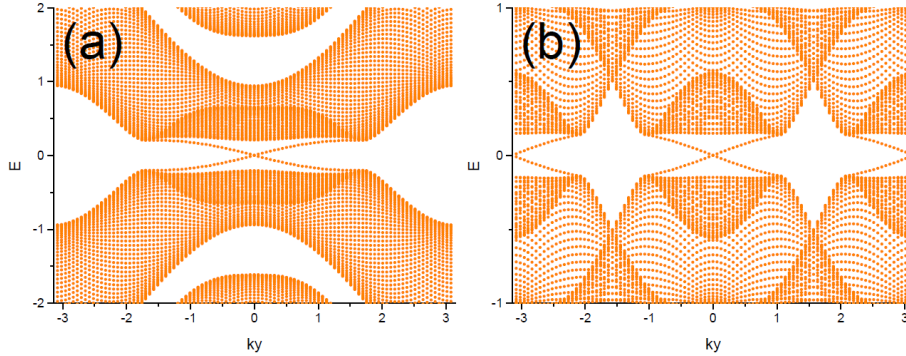


Figure 2.2: (a) and (b) are the edge spectra of the s -wave Rashba superconductor. The open edges are at $i_x = 0$ and $i_x = 50$, k_y denotes the momentum in the y -direction and $k_y \in (-\pi, \pi]$. The parameters are $t = 1$, $\alpha = 1$, $\Delta_{s_1} = 1$ and (a) $\mu = -4$, $V_z^2 = 5$, (b) $\mu = 0$, $V_z^2 = 9$.

2.4 s -wave Dresselhaus superconductor

We would like to explore the topological properties in gapless system. An interesting example is the s -wave superconductor with Dresselhaus (110) spin-orbit coupling in an in-plane magnetic field. This in-plane magnetic field will close the bulk gap and lead to the gapless system. The Hamiltonian of Dresselhaus superconductor is dictated by $H = H_{\text{kin}} + H_s + H_D^{110} + H_Z$, where $\mathbf{V} = (V_x, V_y, 0)$ in the Zeeman term H_Z in Eq. (2.6). In the momentum space, the corresponding BdG Hamiltonian is

$$\mathcal{H}(\mathbf{k}) = \xi(\mathbf{k})\sigma_z + \beta \sin k_x \tau_z + V_x \sigma_z \tau_x + V_y \tau_y - \Delta_{s_1} \sigma_y \tau_y. \quad (2.15)$$

Here we shall show that the phase diagram of the Dresselhaus superconductor has a gapless region that makes the Chern number ill-defined and new topological invariants are needed to characterize the topological property of the Dresselhaus superconductor. For that purposes, we diagonalize the BdG Hamiltonian Eq. (2.15) in the periodic boundary conditions of x and y directions and get the energy spectra

$$E(\mathbf{k}) = \pm \sqrt{\xi^2(\mathbf{k}) + \mathcal{L}^2(\mathbf{k}) + V^2 + \Delta_{s_1}^2} \pm 2\sqrt{\xi^2(\mathbf{k})\mathcal{L}^2(\mathbf{k}) + V^2(\xi^2(\mathbf{k}) + \Delta_{s_1}^2)}, \quad (2.16)$$

where $V = \sqrt{V_x^2 + V_y^2}$ and $\mathcal{L}(\mathbf{k}) = \beta \sin k_x$. Similarly, the following gap-closing conditions: $\xi^2(\mathbf{k}) + \Delta_{s_1}^2 = V^2$, $\mathcal{L}(\mathbf{k}) = 0$ can be obtained. Explicitly, the gap is vanished when $k_x = 0$, $(\mu + 2t + 2t \cos k_y)^2 + \Delta_{s_1}^2 = V^2$ or $k_x = \pi$, $(\mu - 2t + 2t \cos k_y)^2 + \Delta_{s_1}^2 = V^2$. Finally,

the gap closes at $\{k_x = 0, \cos k_y = \frac{\pm\sqrt{V^2 - \Delta_{s_1}^2} - \mu}{2t} - 1\}$ or $\{k_x = \pi, \cos k_y = \frac{\pm\sqrt{V^2 - \Delta_{s_1}^2} - \mu}{2t} + 1\}$ subjected to $|\cos k_y| \leq 1$. Therefore, the gap closes in the regions from A to G as shown in Fig. 2.1(b). The number of gap-closing points at $k_x = 0$ and $k_x = \pi$ are also shown as a pair (ν_1, ν_2) . Later we shall derive a relation between the number of gap-closing points in the first Brillouin zone and the topological invariant of the Hamiltonian. Interestingly, different from the phase diagram of the Rashba superconductor in Fig. 2.1(a), where the gap closes in some boundary lines and each gapped region between them has a distinct Chern number, the phase diagram of the Dresselhaus superconductor has a gapless region from A to G as shown in Fig. 2.1(b), which means that the system is in a semimetal phase in the whole region. Inside the gapless region, the Chern number is not well-defined. However, several other topological invariants which are obtained from symmetry analysis of the Hamiltonian can still be used to characterize the topologically different semimetal phases in the gapless region. For the Hamiltonian Eq. (2.15), we enumerate several symmetries as follows: (i) particle-hole symmetry, $\Xi^{-1}\mathcal{H}(\mathbf{k})\Xi = -\mathcal{H}(-\mathbf{k})$; (ii) partial particle-hole symmetry, $\Xi^{-1}\mathcal{H}(k_x, k_y)\Xi = -\mathcal{H}(-k_x, k_y)$ and (iii) chiral symmetry, $\Sigma^{-1}\mathcal{H}(\mathbf{k})\Sigma = -\mathcal{H}(\mathbf{k})$, where $\Xi = \sigma_x K$, $\Sigma = i\sigma_y \tau_x$ and K is the complex conjugation operator. The Pfaffian invariant [51] for the particle-hole symmetric Hamiltonian can be defined as

$$\mathcal{P} = \text{sgn} \left\{ \frac{\text{Pf}[\mathcal{H}(\mathbf{K}_1)\sigma_x]\text{Pf}[\mathcal{H}(\mathbf{K}_4)\sigma_x]}{\text{Pf}[\mathcal{H}(\mathbf{K}_2)\sigma_x]\text{Pf}[\mathcal{H}(\mathbf{K}_3)\sigma_x]} \right\}, \quad (2.17)$$

where $\mathbf{K}_1 = (0, 0)$, $\mathbf{K}_2 = (\pi, 0)$, $\mathbf{K}_3 = (0, \pi)$ and $\mathbf{K}_4 = (\pi, \pi)$ are the four particle-hole symmetric momenta in the first Brillouin zone of the square lattice. The Pfaffian for a skew-symmetric matrix \mathbf{A} is defined as $\text{Pf}(\mathbf{A})^2 = \text{Det}(\mathbf{A})$. Similarly, the Pfaffian invariant [147] for the partial particle-hole symmetric system is

$$\mathcal{P}(k_y) = \text{sgn} \left\{ \frac{\text{Pf}[\mathcal{H}(\pi, k_y)\sigma_x]}{\text{Pf}[\mathcal{H}(0, k_y)\sigma_x]} \right\}. \quad (2.18)$$

For the chiral symmetry, if we take the basis where Σ is diagonal, $\Sigma = \text{diag}(i, i, -i, -i)$, then the Hamiltonian in this chiral basis becomes off-diagonal, $\mathcal{H}(\mathbf{k}) = \begin{bmatrix} \mathbf{0} & q(\mathbf{k}) \\ q^\dagger(\mathbf{k}) & \mathbf{0} \end{bmatrix}$. Using this $q(\mathbf{k})$, we can define the winding number [132] as

$$\mathcal{W}(k_y) = \frac{i}{2\pi} \int_{-\pi}^{\pi} dk_x \text{tr}[q^{-1}(\mathbf{k})\partial_{k_x} q(\mathbf{k})]. \quad (2.19)$$

The Pfaffian invariant \mathcal{P} can be used for identifying topologically different semimetal phases of the Hamiltonian Eq. (2.15). It is easy to check that $\mathcal{P}_A = \mathcal{P}_B = \mathcal{P}_C = \mathcal{P}_D = -1$ and $\mathcal{P}_E = \mathcal{P}_F = \mathcal{P}_G = 1$ in the phase diagram of the Dresselhaus superconductor as shown in Fig. 2.1(b). Therefore, the semimetal phases in the region of A, B, C, D and the region of E, F, G are topologically inequivalent. As for the other two topological invariants $\mathcal{P}(k_y)$ and $\mathcal{W}(k_y)$, below we shall show that they can be used to determine the range of edge states in the edge Brillouin zone.

To demonstrate the novel properties in the semimetal phase of the Dresselhaus superconductor, we study the Majorana Fermions at the edge and in the vortex core of it. We first study the Majorana flat bands at the edge of the Dresselhaus superconductor. By diagonalizing the Hamiltonian Eq. (2.12) with the parameters $\alpha = 0$, $\Delta_{d_1} = \Delta_{d_2} = 0$ and $V_z = 0$, we get the edge spectra of the Dresselhaus superconductor. Interestingly, although the gap closes in the semimetal phase from region A to G as shown in Fig. 2.1(b), there exist Majorana flat bands at the edge of the system. The Majorana flat bands in the two topologically different semimetal phases in the region A and E are depicted in Fig. 2.3(a) and 2.3(b) respectively. Second, we would like to study the number and range of the Majorana flat bands in these two different semimetal phases. By the Pfaffian invariant Eq. (2.18) or winding number Eq. (2.19), the range where the Majorana flat bands exist in the edge Brillouin zone can be exactly obtained as shown in Fig. 2.3(c) and 2.3(d). The number of Majorana flat bands is half of the number of gap-closing points in the first Brillouin zone. From the Hamiltonian in the chiral basis, we can see that the gap closes when $\text{Det } q(\mathbf{k}) = 0$. In the complex plane of $z(\mathbf{k}) = \text{Det } q(\mathbf{k}) / |\text{Det } q(\mathbf{k})|$, a winding number can be assigned to each gap-closing point \mathbf{k}_0 as

$$\mathcal{W}(\mathbf{k}_0) = \frac{1}{2\pi i} \oint_{\gamma} \frac{dz(\mathbf{k})}{z(\mathbf{k}) - z(\mathbf{k}_0)}, \quad (2.20)$$

where γ is a contour enclosing the gap-closing point. Due to the particle-hole symmetry, $\mathcal{W}(\mathbf{k}_0) = -\mathcal{W}(-\mathbf{k}_0)$; therefore, the gap-closing points with opposite winding number are equal in number. The function $z(\mathbf{k})$ in the region A and E are shown in Fig. 2.3(e) and 2.3(f). As long as the projection of opposite winding number gap-closing points does not completely overlap in the edge Brillouin zone, there will be Majorana flat bands connecting them [161]. Therefore, the number of Majorana flat bands is $\nu = (\nu_1 + \nu_2)/2$ and it is easy to check that the Pfaffian invariant \mathcal{P} in Eq. (2.17) is the parity of ν , $\mathcal{P} = (-1)^\nu$. The corresponding densities of states of these two different semimetal phases are shown in Fig. 2.3(g) and 2.3(h). We find that there is a peak at zero energy which

is clearly visible in the tunneling conductance measurements. Therefore, the Majorana flat bands have clear experimental signature in the tunneling conductance measurements and should be experimentally observable. As for the robustness of the Majorana flat bands against disorder or impurity, we can discuss it from the topological point of view. As long as the disorder or impurity does not break the symmetries of Hamiltonian Eq. (2.15), these Majorana flat bands will be protected by the three topological invariants mentioned above.

The existence of the edge states implies the nontrivial momentum space topology in the Dresselhaus superconductor so that the Majorana fermions emerge at the edge of the system. In the following, we explicitly calculate the zero-energy Majorana flat bands at the edge of the Dresselhaus superconductor in the cylindrical symmetry. Let x -direction to be open and y to be periodic, then by setting $k_x \rightarrow -i\partial_x$, we solve the Schrödinger equation of the Hamiltonian Eq. (2.15) in the real space, $H(k_x \rightarrow -i\partial_x, k_y)\Psi = 0$, where $\Psi = (u_\uparrow, u_\downarrow, v_\uparrow, v_\downarrow)^T$. Due to the particle-hole symmetry in the Dresselhaus superconductor, we have $u_\uparrow = v_\uparrow^*$ and $u_\downarrow = v_\downarrow^*$ at zero energy. Thus, we only need to consider the upper block of the Hamiltonian Eq. (2.15). For simplicity, we consider the low energy theory at $k_x = 0$, up to the first order, we have

$$\begin{aligned}(\varepsilon(k_y) - i\beta\partial_x)u_\uparrow + (V_x - iV_y)u_\downarrow + \Delta_{s_1}u_\downarrow^* &= 0, \\(\varepsilon(k_y) + i\beta\partial_x)u_\downarrow + (V_x + iV_y)u_\uparrow - \Delta_{s_1}u_\uparrow^* &= 0,\end{aligned}\tag{2.21}$$

where $\varepsilon(k_y) = -2t(1 + \cos k_y) - \mu$. Observing that $u_\uparrow = \pm iu_\downarrow^*$ in Eq. (2.21), we obtain when $u_\uparrow = iu_\downarrow^*$, the solution is $u_\uparrow(x) = c_1u_\uparrow^1(x) + c_2u_\uparrow^2(x)$, where c_1 and c_2 are real numbers and

$$\begin{aligned}u_\uparrow^1(x) &= A_1e^{\lambda_1x} + A_2e^{\lambda_2x}, \\u_\uparrow^2(x) &= iB_1e^{\lambda_1x} + iB_2e^{\lambda_2x}.\end{aligned}\tag{2.22}$$

Here

$$\begin{aligned}\lambda_1 &= \frac{-\Delta_{s_1} - \sqrt{V^2 - \varepsilon^2(k_y)}}{\beta}, \\ \lambda_2 &= \frac{-\Delta_{s_1} + \sqrt{V^2 - \varepsilon^2(k_y)}}{\beta},\end{aligned}\tag{2.23}$$

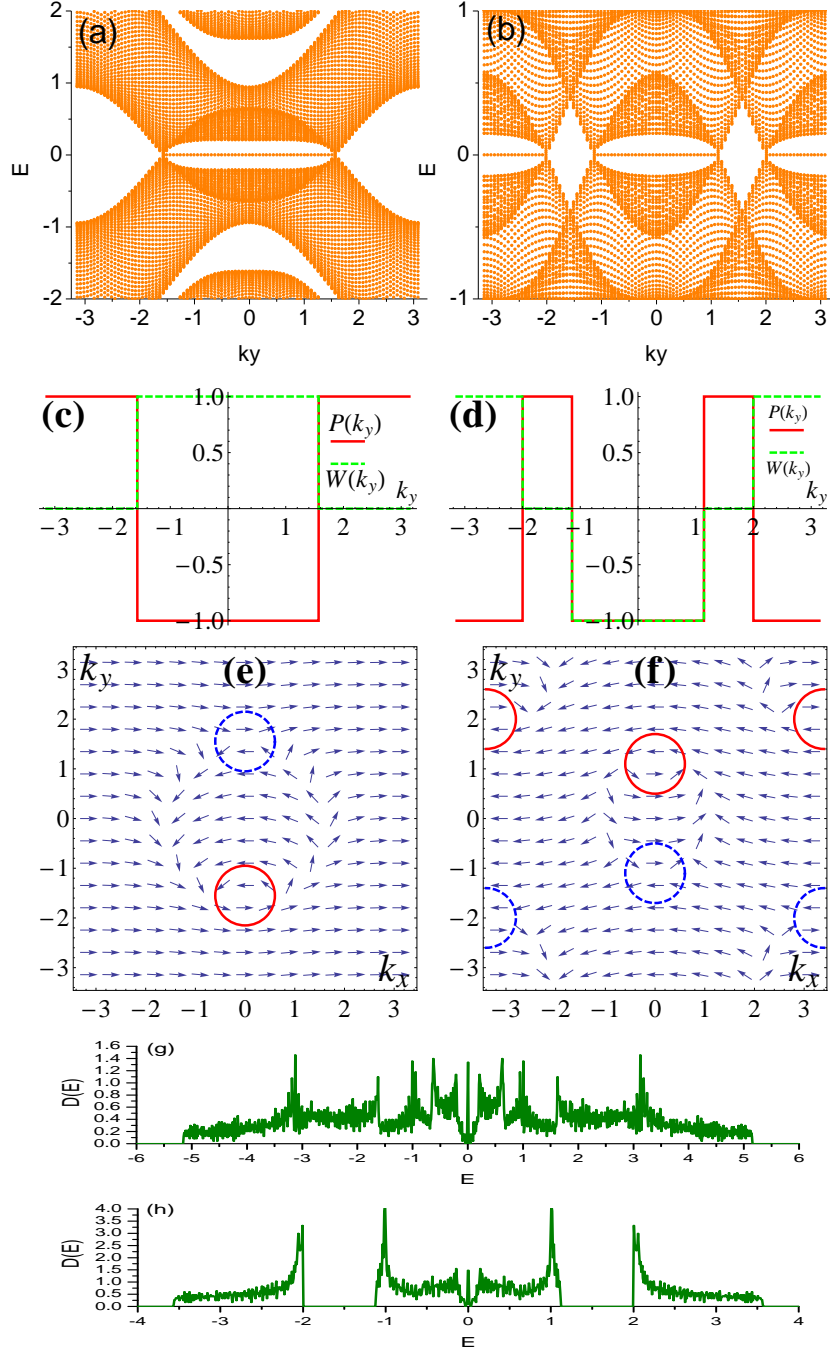


Figure 2.3: (a) and (b) are the edge spectra of the s -wave superconductor with Dresselhaus SO interaction. The open edges are at $i_x = 0$ and $i_x = 50$, k_y denotes the momentum in the y direction and $k_y \in (-\pi, \pi]$. The parameters are $t = 1$, $\beta = 1$, $\Delta_{s_1} = 1$ and (a) $\mu = -4$, $V^2 = 5$, (b) $\mu = 0$, $V^2 = 9$, which correspond to region A and E in Fig. 2.1(b) respectively. (c) and (d) are the Pfaffian invariant Eq. (2.18) and winding number Eq. (2.19) for (a) and (b). (e) and (f) are the function $z(\mathbf{k})$ for (a) and (b). The winding number of gap-closing point enclosed by the red solid circle is 1 and by the blue dashed circle is -1 respectively. (g) and (h) are the densities of states for (a) and (b) respectively.

and

$$\begin{aligned} A_1 &= \frac{1}{2} \left[1 - \frac{V_x - i(V_y + \varepsilon)}{\sqrt{V^2 - \varepsilon^2}} \right], A_2 = \frac{1}{2} \left[1 + \frac{V_x - i(V_y + \varepsilon)}{\sqrt{V^2 - \varepsilon^2}} \right], \\ B_1 &= \frac{1}{2} \left[1 + \frac{V_x - i(V_y - \varepsilon)}{\sqrt{V^2 - \varepsilon^2}} \right], B_2 = \frac{1}{2} \left[1 - \frac{V_x - i(V_y - \varepsilon)}{\sqrt{V^2 - \varepsilon^2}} \right]. \end{aligned} \quad (2.24)$$

When $u_\uparrow = -iu_\downarrow^*$, the solution is similar to the case of $u_\uparrow = iu_\downarrow^*$. We consider the Dresselhaus superconductor in the positive x plane with the edge located at $x = 0$. Let us assume $\Delta_{s_1} > 0$ for simplicity, then from the solutions to Eq. (2.21), the critical point for existing a normalizable wavefunction under this boundary condition is determined by $V^2 - \varepsilon(k_y)^2 = \Delta_{s_1}^2$, which is consistent with the gap-closing condition $(\mu + 2t + 2t \cos k_y)^2 + \Delta_{s_1}^2 = V^2$ at $k_x = 0$. By the same reason, the condition for normalizable wavefunctions is consistent with the gap-closing condition $(\mu - 2t + 2t \cos k_y)^2 + \Delta_{s_1}^2 = V^2$ if we consider the low energy theory at $k_x = \pi$. Therefore, the Majorana flat band is $(u_\uparrow, iu_\uparrow^*, u_\uparrow^*, -iu_\uparrow)^T$, where u_\uparrow is the solution to Eq. (2.21).

To further study the Majorana fermions in the Dresselhaus superconductor, we consider the zero energy vortex core states by solving the BdG equation for the superconducting order parameter of a single vortex $\Delta(r, \theta) = \Delta e^{i\theta}$ [128]. To do this, the s -wave superconducting term in the Hamiltonian Eq. (2.2) is modified to be position-dependent,

$$H_s = \sum_i (\Delta e^{i\theta_i} c_{i\uparrow}^\dagger c_{i\downarrow}^\dagger + \text{H.c.}). \quad (2.25)$$

We numerically solve the Schrödinger equation $H\Psi = E\Psi$ for the Hamiltonian in Eq. (2.15) in real space, where $\Psi = (u_\uparrow, u_\downarrow, v_\uparrow, v_\downarrow)^T$. At zero energy we have $u_\uparrow = v_\uparrow^*$ and $u_\downarrow = v_\downarrow^*$ as the particle-hole symmetry in the Dresselhaus superconductor, then the Bogoliubov quasiparticle operator,

$$\gamma^\dagger(E) = \sum_i (u_{i\uparrow} c_{i\uparrow}^\dagger + u_{i\downarrow} c_{i\downarrow}^\dagger + v_{i\uparrow} c_{i\uparrow} + v_{i\downarrow} c_{i\downarrow}) \quad (2.26)$$

becomes Majorana operator $\gamma^\dagger(0) = \gamma(0)$. Below we only consider the zero energy vortex core states for discussing the MFs in the vortex core. Setting the x and y directions to be open boundary, we then solve the BdG equations numerically and calculate the density profile of quasiparticle for the zero energy vortex core states. The density of quasiparticle at site i is defined as $u_{i\uparrow}^* u_{i\uparrow} + u_{i\downarrow}^* u_{i\downarrow}$. Previously, we have shown in Fig. 2.3 that there is a novel semimetal phase in the Dresselhaus superconductor where the zero-energy flat

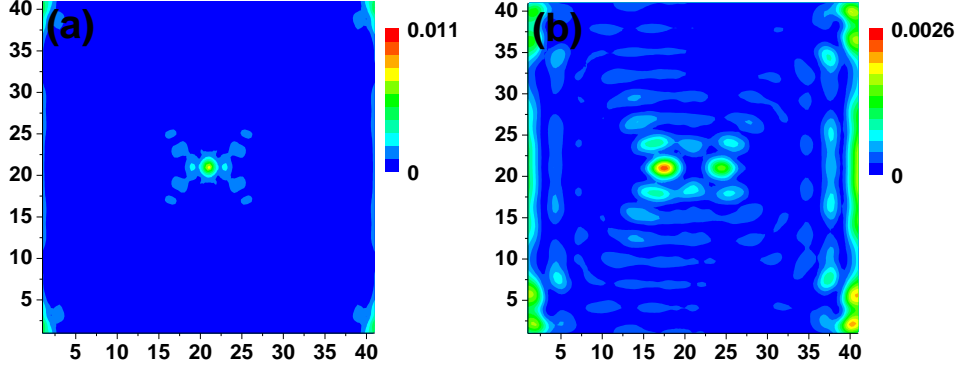


Figure 2.4: The probability distribution of quasiparticle for the Dresselhaus superconductor plotted on the 41×41 square lattice. The parameters are $t = 1$, $\beta = 1$, $\Delta_{s_1} = 1$. The chemical potential and in-plane magnetic field are (a) $\mu = -4, V^2 = 5$ and (b) $\mu = 0, V^2 = 9$.

bands host MFs. Here we shall ascertain if there exist zero energy vortex core states hosting MFs in this semimetal phase. The density profiles of quasiparticle of the zero energy vortex core states are shown in Fig. 2.4(a) and 2.4(b), which correspond to the region A and E in the phase diagram of Fig. 2.1(b) respectively. The numerical results of the energy for the zero energy vortex core states are $E = 2.54 \times 10^{-3}$ for Fig. 2.4(a) and $E = 6.68 \times 10^{-3}$ for Fig. 2.4(b) respectively. It is clear to see from Fig. 2.4 that there are zero-energy states in the vortex core. Therefore, the Majorana fermions exist in the vortex core of the s -wave Dresselhaus superconductor.

2.5 Topological properties of the spin-singlet superconductor

2.5.1 symmetries of the BdG Hamiltonian

For the general BdG Hamiltonian of the spin-singlet superconductor Eq. (2.7), it satisfies the particle-hole symmetry

$$\Xi^{-1}\mathcal{H}(\mathbf{k})\Xi = -\mathcal{H}(-\mathbf{k}), \quad (2.27)$$

where $\Xi = \Lambda K$, $\Lambda = \sigma_x \otimes \tau_0$ and K is the complex conjugation operator. We find that apart from the particle-hole symmetry, the BdG Hamiltonian can satisfy some extra

symmetries, namely, partial particle-hole symmetry, chiral symmetry and partial chiral symmetry when some parameters in the Hamiltonian Eq. (2.7) are vanishing. The particle-hole- k_x and particle-hole- k_y symmetries are defined as

$$\Xi_{k_x}^{-1} \mathcal{H}(k_x, k_y) \Xi_{k_x} = -\mathcal{H}(-k_x, k_y) \quad (2.28)$$

and

$$\Xi_{k_y}^{-1} \mathcal{H}(k_x, k_y) \Xi_{k_y} = -\mathcal{H}(k_x, -k_y), \quad (2.29)$$

where Ξ_{k_x} (Ξ_{k_y}) takes the k_x (k_y) in the Hamiltonian to $-k_x$ ($-k_y$). The chiral symmetry is given by

$$\Sigma^{-1} \mathcal{H}(\mathbf{k}) \Sigma = -\mathcal{H}(\mathbf{k}). \quad (2.30)$$

The chiral- k_x and chiral- k_y symmetries are defined as

$$\Sigma_{k_x}^{-1} \mathcal{H}(k_x, k_y) \Sigma_{k_x} = -\mathcal{H}(-k_x, k_y) \quad (2.31)$$

and

$$\Sigma_{k_y}^{-1} \mathcal{H}(k_x, k_y) \Sigma_{k_y} = -\mathcal{H}(k_x, -k_y), \quad (2.32)$$

where Σ_{k_x} (Σ_{k_y}) takes the k_x (k_y) in the Hamiltonian to $-k_x$ ($-k_y$).

We are interested in the BdG Hamiltonian which has one or more extra symmetries. In the following, we would like to consider these kinds of the BdG Hamiltonian as listed in Tab. 2.1. The spin-singlet superconductor with Rashba spin-orbit coupling has been investigated in Ref. [131]. Here we only consider the general $d_{x^2-y^2} + id_{xy} + s$ pairing in case (a) for the spin-singlet Rashba superconductor. We shall focus on the topological properties of the superconductor with Dresselhaus (110) spin-orbit coupling as shown in case (b)-(g) of Tab. 2.1.

2.5.2 topological invariants of the BdG Hamiltonian

For the fully gapped Hamiltonian, we can always define the Chern number as a topological invariant of the Hamiltonian as shown in Eq. (2.9). If the Hamiltonian has some

case	spin-orbit coupling	magnetic field	pairing symmetry	Hamiltonian symmetry	topological invariant
(a)	α	V_z	$\Delta_{s_1}, \Delta_{d_1}, \Delta_{d_2}$	Ξ, Σ_{k_x}	\mathcal{P}, \mathcal{W}
(b)	β	V_x, V_y	Δ_{s_1}	$\Xi, \Xi_{k_x}, \Sigma, \Sigma_{k_y}$	$\mathcal{P}, \mathcal{P}(k_y), \mathcal{W}, \mathcal{W}(k_y)$
(c)			$\Delta_{s_1}, \Delta_{s_2}$	Ξ, Ξ_{k_x}	$\mathcal{P}, \mathcal{P}(k_y)$
(d)			Δ_{d_1}	$\Xi, \Xi_{k_x}, \Sigma, \Sigma_{k_y}$	$\mathcal{P}, \mathcal{P}(k_y), \mathcal{W}, \mathcal{W}(k_y)$
(e)			$\Delta_{d_1}, \Delta_{d_2}$	Ξ, Σ_{k_y}	\mathcal{P}, \mathcal{W}
(f)			$\Delta_{s_1}, \Delta_{d_1}$	Ξ, Ξ_{k_x}, Σ	$\mathcal{P}, \mathcal{P}(k_y), \mathcal{W}(k_y)$
(g)			$\Delta_{s_1}, \Delta_{d_1}, \Delta_{d_2}$	Ξ, Σ_{k_y}	\mathcal{P}, \mathcal{W}

Table 2.1: The BdG Hamiltonian with extra symmetries, namely, the particle-hole symmetry and the particle-hole- k_x symmetry, $\Xi = \Xi_{k_x} = \sigma_x K$, the chiral symmetry and the chiral- k_y symmetry, $\Sigma = \Sigma_{k_y} = i\sigma_y \tau_x$, and the chiral- k_x symmetry, $\Sigma_{k_x} = i\sigma_y \tau_z$. The topological invariants corresponding to these extra symmetries are also shown in the last column.

extra symmetries, more topological invariants can be introduced into the system.

We first consider the particle-hole symmetry Eq. (2.27) which can be reduced to $\Lambda \mathcal{H}(\mathbf{k}) \Lambda = -\mathcal{H}^*(-\mathbf{k})$. We find that under this symmetry $\mathcal{H}(\mathbf{K}) \Lambda$ is an antisymmetric matrix with $(\mathcal{H}(\mathbf{K}) \Lambda)^T = -\mathcal{H}(\mathbf{K}) \Lambda$, where \mathbf{K} is the particle-hole symmetric momenta satisfying $\mathbf{K} = -\mathbf{K} + \mathbf{G}$ and \mathbf{G} is the reciprocal lattice vector of the square lattice. With this property, we can define the Pfaffian invariant for the particle-hole symmetric Hamiltonian as [51]

$$\mathcal{P} = \text{sgn} \left\{ \frac{\text{Pf}[\mathcal{H}(\mathbf{K}_1) \Lambda] \text{Pf}[\mathcal{H}(\mathbf{K}_4) \Lambda]}{\text{Pf}[\mathcal{H}(\mathbf{K}_2) \Lambda] \text{Pf}[\mathcal{H}(\mathbf{K}_3) \Lambda]} \right\}, \quad (2.33)$$

where $\mathbf{K}_1 = (0, 0)$, $\mathbf{K}_2 = (\pi, 0)$, $\mathbf{K}_3 = (0, \pi)$ and $\mathbf{K}_4 = (\pi, \pi)$ are the four particle-hole symmetric momenta in the first Brillouin zone of the square lattice. Here we shall show that the Pfaffian invariant \mathcal{P} is the parity of the Chern number \mathcal{C} , $\mathcal{P} = (-1)^{\mathcal{C}}$. For the $2n \times 2n$ antisymmetric matrix $\mathcal{H}(\mathbf{K}) \Lambda$, we have $\text{Pf}[\mathcal{H}(\mathbf{K}) \Lambda]^* = (-1)^n \text{Pf}[\mathcal{H}(\mathbf{K}) \Lambda]$. Therefore, $(i^n \text{Pf}[\mathcal{H}(\mathbf{K}) \Lambda])^* = i^n \text{Pf}[\mathcal{H}(\mathbf{K}) \Lambda]$ is real and we can associate a quantity $S[\mathcal{H}(\mathbf{K})] = \text{sgn}\{i^n \text{Pf}[\mathcal{H}(\mathbf{K}) \Lambda]\}$ with any particle-hole symmetric Hamiltonian. Suppose $\mathcal{H}(\mathbf{K})$ is diagonalized by the transformation $\mathcal{H}(\mathbf{K}) = U(\mathbf{K}) D(\mathbf{K}) U^\dagger(\mathbf{K})$, where $D(\mathbf{K})$ is a diagonal matrix of eigenvalues $\text{diag}\{E_n(\mathbf{K}), \dots, E_1(\mathbf{K}), -E_1(\mathbf{K}), \dots, -E_n(\mathbf{K})\}$ and the columns of the unitary matrix $U(\mathbf{K})$ are the eigenvectors of $\mathcal{H}(\mathbf{K})$. The eigenvectors for the positive eigenvalues in $U(\mathbf{K})$ are chosen to be related to the eigenvectors for negative eigenvalues by the particle-hole symmetry [131]. With this convention, we find that $U^\dagger \Lambda = \Gamma U^T$,

where $\Gamma = \sigma_x \tau_x$. Therefore, $S[\mathcal{H}(\mathbf{K})]$ can be further reduced to

$$\begin{aligned}
S[\mathcal{H}(\mathbf{K})] &= \text{sgn}\{i^n \text{Pf}[\mathcal{H}(\mathbf{K})\Lambda]\}, \\
&= \text{sgn}\{i^n \text{Pf}[U(\mathbf{K})D(\mathbf{K})U^\dagger(\mathbf{K})\Lambda]\}, \\
&= \text{sgn}\{i^n \text{Pf}[U(\mathbf{K})D(\mathbf{K})\Gamma U^T(\mathbf{K})]\}, \\
&= \text{sgn}\{i^n \text{Det } U(\mathbf{K}) \text{Pf}[D(\mathbf{K})\Gamma]\}.
\end{aligned} \tag{2.34}$$

Since $\text{Pf}[D(\mathbf{K})\Gamma] = \prod_{n>0} E_n(\mathbf{K}) > 0$ and $|\text{Det } U(\mathbf{K})| = 1$, we arrive at

$$S[\mathcal{H}(\mathbf{K})] = i^n \text{Det } U(\mathbf{K}). \tag{2.35}$$

Note that $\mathbf{A}(\mathbf{k}) = i \sum_n \langle \psi_n(\mathbf{k}) | \nabla \psi_n(\mathbf{k}) \rangle$ is a total derivative [131], $\mathbf{A}(\mathbf{k}) = i \nabla \ln[\text{Det } U(\mathbf{k})]$. Therefore, consider a pair of particle-hole symmetric momenta \mathbf{K}_1 and \mathbf{K}_2 , we find that

$$\frac{\text{Det } U(\mathbf{K}_2)}{\text{Det } U(\mathbf{K}_1)} = e^{-iS_{1,2}}, \tag{2.36}$$

where $S_{1,2} = \int_{\mathbf{K}_1}^{\mathbf{K}_2} \mathbf{A}(\mathbf{k}) \cdot d\mathbf{k}$ and the line integral runs from \mathbf{K}_1 to \mathbf{K}_2 . Since $\mathbf{A}^+(\mathbf{k}) = i \sum_{n>0} \langle \psi_n(\mathbf{k}) | \nabla \psi_n(\mathbf{k}) \rangle = \mathbf{A}^-(\mathbf{k})$, we find that $S_{1,2} = \int_{\gamma_1} \mathbf{A}^-(\mathbf{k}) \cdot d\mathbf{k}$, where γ_1 is the line from $(-\pi, 0)$ to $(\pi, 0)$. Similarly,

$$\frac{\text{Det } U(\mathbf{K}_4)}{\text{Det } U(\mathbf{K}_3)} = e^{-iS_{3,4}}, \tag{2.37}$$

where $S_{3,4} = \int_{\gamma_2} \mathbf{A}^-(\mathbf{k}) \cdot d\mathbf{k}$ and γ_2 is the line from $(-\pi, \pi)$ to (π, π) . Therefore,

$$\frac{\text{Det } U(\mathbf{K}_1) \text{Det } U(\mathbf{K}_4)}{\text{Det } U(\mathbf{K}_2) \text{Det } U(\mathbf{K}_3)} = e^{iS_\gamma}, \tag{2.38}$$

where $S_\gamma = \oint_\gamma \mathbf{A}^-(\mathbf{k}) \cdot d\mathbf{k}$ and γ is the directed line surrounding the upper half Brillouin zone (UHBZ) in the anticlockwise direction. Since $\mathcal{F}^-(\mathbf{k}) = \partial_{k_x} A_y^-(\mathbf{k}) - \partial_{k_y} A_x^-(\mathbf{k}) =$

$\mathcal{F}^-(-\mathbf{k})$, we have

$$\begin{aligned}
S_\gamma &= \oint_\gamma \mathbf{A}^-(\mathbf{k}) \cdot d\mathbf{k}, \\
&= \int_{UHBZ} d^2\mathbf{k} \mathcal{F}^-(\mathbf{k}), \\
&= \frac{1}{2} \int_{FBZ} d^2\mathbf{k} \mathcal{F}^-(\mathbf{k}), \\
&= \pi \mathcal{C}.
\end{aligned} \tag{2.39}$$

Finally, we obtain that

$$\begin{aligned}
\mathcal{P} &= \text{sgn} \left\{ \frac{\text{Pf}[\mathcal{H}(\mathbf{K}_1)\Lambda] \text{Pf}[\mathcal{H}(\mathbf{K}_4)\Lambda]}{\text{Pf}[\mathcal{H}(\mathbf{K}_2)\Lambda] \text{Pf}[\mathcal{H}(\mathbf{K}_3)\Lambda]} \right\}, \\
&= \frac{\text{Det } U(\mathbf{K}_1) \text{Det } U(\mathbf{K}_4)}{\text{Det } U(\mathbf{K}_2) \text{Det } U(\mathbf{K}_3)}, \\
&= (-1)^c.
\end{aligned} \tag{2.40}$$

Therefore, the Pfaffian invariant \mathcal{P} is the parity of the Chern number.

Similarly, if the Hamiltonian has partial particle-hole symmetry, for example, the particle-hole- k_x symmetry Eq. (2.28), then we can treat k_y as a parameter and define the Pfaffian invariant $\mathcal{P}(k_y)$ to identify the location of the edge states in the edge Brillouin zone [147; 166],

$$\mathcal{P}(k_y) = \text{sgn} \left\{ \frac{\text{Pf}[\mathcal{H}(\pi, k_y)\Lambda]}{\text{Pf}[\mathcal{H}(0, k_y)\Lambda]} \right\}, \tag{2.41}$$

where $k_x = 0$ and $k_x = \pi$ are the two particle-hole symmetric momenta in the edge Brillouin zone. Similar to the Eq. (2.40), we can get an expression of $\mathcal{P}(k_y)$ in terms of the line integral of the vector potential $A_x^-(\mathbf{k})$ as

$$\mathcal{P}(k_y) = (-1)^{\frac{1}{\pi} \int_{-\pi}^{\pi} dk_x A_x^-(\mathbf{k})}. \tag{2.42}$$

If the Hamiltonian has chiral symmetry Eq. (2.30), then the winding number can be introduced as a topological invariant of the system. Here the chiral symmetry $\Sigma = i\sigma_y\tau_x$ can be diagonalized as $\Sigma = TDT^\dagger$ with $TT^\dagger = 1$ and $D = \text{diag}\{i, i, -i, -i\}$. The Hamiltonian $\mathcal{H}(\mathbf{k})$ is then simultaneously off-diagonalized as $\mathcal{H}(\mathbf{k}) = TQ(\mathbf{k})T^\dagger$, where

$Q(\mathbf{k})$ is of the form $\begin{bmatrix} 0 & q(\mathbf{k}) \\ q^\dagger(\mathbf{k}) & 0 \end{bmatrix}$. We can thus define the winding number as

$$\begin{aligned} \mathcal{W}(k_y) &= -\frac{1}{4\pi} \int_{-\pi}^{\pi} dk_x \text{tr}[\Sigma \mathcal{H}^{-1}(\mathbf{k}) \partial_{k_x} \mathcal{H}(\mathbf{k})], \\ &= -\frac{1}{4\pi} \int_{-\pi}^{\pi} dk_x \text{tr}[DQ^{-1}(\mathbf{k}) \partial_{k_x} Q(\mathbf{k})], \\ &= \frac{i}{4\pi} \int_{-\pi}^{\pi} dk_x \text{tr}[q^{-1}(\mathbf{k}) \partial_{k_x} q(\mathbf{k}) - q^{\dagger-1}(\mathbf{k}) \partial_{k_x} q^\dagger(\mathbf{k})], \\ &= -\frac{1}{2\pi} \text{Im} \int_{-\pi}^{\pi} dk_x \text{tr}[q^{-1}(\mathbf{k}) \partial_{k_x} q(\mathbf{k})]. \end{aligned} \quad (2.43)$$

Here we show that $\int_{-\pi}^{\pi} dk_x \text{tr}[q^{-1}(\mathbf{k}) \partial_{k_x} q(\mathbf{k})]$ is pure imaginary. It is easy to see that $\text{tr}[q^{-1} \partial_{k_x} q]^* = -\text{tr}[q^\dagger \partial_{k_x} q^{\dagger-1}]$. From the eigen equation of $Q(\mathbf{k})$, we find that $qq^\dagger|\psi_n\rangle = E_n^2|\psi_n\rangle$ which leads to the identity $qq^\dagger\Psi = \Psi\Pi$, where $\Pi = \text{diag}\{E_1^2, E_2^2\}$ and the unitary matrix $\Psi = (|\psi_1\rangle, |\psi_2\rangle)$. Therefore, $q^\dagger = q^{-1}\Psi\Pi\Psi^{-1}$ and we obtain $\text{tr}[q^\dagger \partial_{k_x} q^{\dagger-1}] = \text{tr}[q^{-1} \partial_{k_x} q] + \text{tr}[\Pi \partial_{k_x} \Pi^{-1}]$; accordingly,

$$\int_{-\pi}^{\pi} dk_x \text{tr}[q^{-1} \partial_{k_x} q]^* = -\int_{-\pi}^{\pi} dk_x \text{tr}[q^{-1} \partial_{k_x} q] - \int_{-\pi}^{\pi} dk_x \text{tr}[\Pi \partial_{k_x} \Pi^{-1}]. \quad (2.44)$$

Due to the periodic boundary condition, we have $E_n(k_x = -\pi, k_y) = E_n(k_x = \pi, k_y)$ so that

$$\int_{-\pi}^{\pi} dk_x \text{tr}[\Pi \partial_{k_x} \Pi^{-1}] = -2 \sum_{n=1}^2 \int_{-\pi}^{\pi} dk_x \partial_{k_x} \ln E_n(\mathbf{k}) = 0. \quad (2.45)$$

Thus $\int_{-\pi}^{\pi} dk_x \text{tr}[q^{-1} \partial_{k_x} q]^* = -\int_{-\pi}^{\pi} dk_x \text{tr}[q^{-1} \partial_{k_x} q]$ is pure imaginary. Finally, the winding number for the chiral symmetry Eq. (2.30) is obtained,

$$\mathcal{W}(k_y) = -\frac{1}{2\pi i} \int_{-\pi}^{\pi} dk_x \text{tr}[q^{-1}(\mathbf{k}) \partial_{k_x} q(\mathbf{k})]. \quad (2.46)$$

When the Hamiltonian has partial particle-hole symmetry and chiral symmetry simultaneously, we can find a relation between the Pfaffian invariant $\mathcal{P}(k_y)$ and the winding number $\mathcal{W}(k_y)$. According to the Ref. [131], $\frac{1}{\pi} \int_{-\pi}^{\pi} A_x^-(\mathbf{k}) = \frac{1}{2\pi i} \int_{-\pi}^{\pi} \text{tr}[q(\mathbf{k})^{-1} \partial_{k_x} q(\mathbf{k})] + 2N$, where N is an integer. Substituting this relation into Eq. (2.42), we get that $\mathcal{P}(k_y) = (-1)^{\mathcal{W}(k_y)}$. Therefore, the Pfaffian invariant $\mathcal{P}(k_y)$ is the parity of the winding number $\mathcal{W}(k_y)$.

If the Hamiltonian has partial chiral symmetry, for example, the chiral- k_y symmetry Eq. (2.32), then we can only define the winding number $\mathcal{W}(k_y)$ at $k_y = 0$ and $k_y = \pi$. Consequently, we can associate a topological invariant \mathcal{W} with the chiral- k_y symmetry as [131]

$$\mathcal{W} = (-1)^{\mathcal{W}(0) - \mathcal{W}(\pi)}. \quad (2.47)$$

The topological invariant \mathcal{W} is also the parity of the Chern number, $\mathcal{W} = (-1)^{\mathcal{C}}$. Therefore, the Pfaffian invariant \mathcal{P} for the particle-hole symmetry is equivalent to the topological invariant \mathcal{W} for the partial chiral symmetry.

2.5.3 phase diagrams of the BdG Hamiltonian

In contrast to the even number of Majorana bound states in the trivial topological phase, the number of Majorana bound states is odd in the nontrivial topological phase. The Pfaffian invariant \mathcal{P} is in fact the parity of the number of Majorana bound states. Therefore, we can use the Pfaffian invariant \mathcal{P} to investigate the topological quantum phase transitions in the BdG Hamiltonian Eq. (2.7). The phase diagrams are shown in Fig. 2.5. We now focus on the red region where the Pfaffian invariant $\mathcal{P} = -1$ which means that the system has an odd number of Majorana bound states at the edge and is thus in the nontrivial topological phase. The explicit expression of the Pfaffian invariant Eq. (2.33) for the general case of the BdG Hamiltonian is

$$\mathcal{P} = \text{sgn} \left\{ \frac{[(\mu + 4t)^2 + (\Delta_{s_1}^2 + \Delta_{s_2}^2) - V^2][(\mu - 4t)^2 + (\Delta_{s_1}^2 + \Delta_{s_2}^2) - V^2]}{[\mu^2 + (\Delta_{s_1} + 2\Delta_{d_1})^2 + \Delta_{s_2}^2 - V^2][\mu^2 + (\Delta_{s_1} - 2\Delta_{d_1})^2 + \Delta_{s_2}^2 - V^2]} \right\}. \quad (2.48)$$

Therefore, the phase diagram is divided by the following four parabolas in the plane of $V^2 \sim \mu$:

$$\begin{aligned} (i)V^2 &= (\mu + 4t)^2 + (\Delta_{s_1}^2 + \Delta_{s_2}^2); \\ (ii)V^2 &= (\mu - 4t)^2 + (\Delta_{s_1}^2 + \Delta_{s_2}^2); \\ (iii)V^2 &= \mu^2 + (\Delta_{s_1} + 2\Delta_{d_1})^2 + \Delta_{s_2}^2; \\ (iv)V^2 &= \mu^2 + (\Delta_{s_1} - 2\Delta_{d_1})^2 + \Delta_{s_2}^2, \end{aligned} \quad (2.49)$$

where $V^2 = V_x^2 + V_y^2 + V_z^2$. Notice that the Pfaffian invariant \mathcal{P} has nothing to do with the spin-orbit couplings. Thus the topological phases can exist even without the spin-orbit couplings. However, the spin-orbit couplings can open a gap to render the Majorana

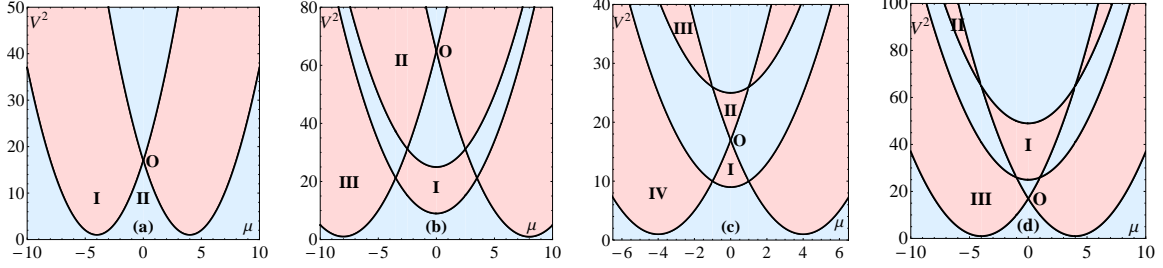


Figure 2.5: The possible phase diagrams of the spin-singlet superconductor with Rashba and Dresselhaus (110) spin-orbit couplings. (a) is the phase diagram for the pure s -wave or d -wave superconductor. (b), (c) and (d) are the phase diagrams for the $d + s$ -wave superconductor.

fermion located at the edge of the system; otherwise the Majorana fermion will spread into the bulk. Now we turn to discuss all the possible phase diagrams in the BdG Hamiltonian. When $\Delta_{s_1}\Delta_{d_1} = 0$, the phase diagram is only divided by the parabolas (i) and (ii) and is shown in Fig. 2.5(a). When $\Delta_{s_1}\Delta_{d_1} \neq 0$, there are three topologically different cases in the phase diagrams as follows. Let us first define the intersection point of the parabolas (i) and (ii) as O , then the phase diagram where the parabolas (iii) and (iv) are both below O is shown in Fig. 2.5(b); the phase diagram where the parabolas (iii) and (iv) are on either side of O is shown in Fig. 2.5(c); the phase diagram where the parabolas (iii) and (iv) are both above O is shown in Fig. 2.5(d). Furthermore, if we assume $\Delta_{s_1}\Delta_{d_1} > 0$, then the phase diagram is as Fig. 2.5(b) when $\Delta_{d_1}^2 - \Delta_{s_1}\Delta_{d_1} < \Delta_{d_1}^2 + \Delta_{s_1}\Delta_{d_1} < 4t^2$; the phase diagram is as Fig. 2.5(c) when $\Delta_{d_1}^2 - \Delta_{s_1}\Delta_{d_1} < 4t^2 < \Delta_{d_1}^2 + \Delta_{s_1}\Delta_{d_1}$; the phase diagram is as Fig. 2.5(d) when $4t^2 < \Delta_{d_1}^2 - \Delta_{s_1}\Delta_{d_1} < \Delta_{d_1}^2 + \Delta_{s_1}\Delta_{d_1}$. Therefore, we have exhibited all the possible phase diagrams in the BdG Hamiltonian Eq. (2.7). For the pure s -wave and d -wave superconductors, the phase diagrams are topologically equivalent to Fig. 2.5(a); for the superconductors with mixed s -wave and d -wave pairing symmetries, the phase diagrams are topologically equivalent to Fig. 2.5(b), Fig. 2.5(c) and Fig. 2.5(d) depending on the hopping amplitude t .

2.5.4 Majorana bound states at the edge of the BdG Hamiltonian

In this section, we demonstrate the Majorana bound states at the edge of the spin-singlet superconductor in the different cases as listed in Tab. 2.1. By setting the boundary conditions of x direction to be open and y direction to be periodic, we diagonalize the

Hamiltonian Eq. (2.7) in this cylindrical symmetry and get the edge spectra of the Hamiltonian. Generally, the solution is $\Psi = (\Psi_1, \dots, \Psi_{N_x})^T$, where N_x is the number of unit cells in the x direction and $\Psi_i = (u_{i\uparrow}, u_{i\downarrow}, v_{i\uparrow}, v_{i\downarrow})$ is the wave function at cell i . In particular, at zero energy we have $u_\uparrow = v_\uparrow^*$ and $u_\downarrow = v_\downarrow^*$ due to the particle-hole symmetry in the superconductor, then the Bogoliubov quasiparticle operator, $\gamma^\dagger(E) = \sum_{j=(i_x, k_y)} (u_{j\uparrow} c_{j\uparrow}^\dagger + u_{j\downarrow} c_{j\downarrow}^\dagger + v_{j\uparrow} c_{j\uparrow} + v_{j\downarrow} c_{j\downarrow})$, becomes Majorana operator $\gamma^\dagger(0) = \gamma(0)$. Therefore, once the zero-energy states exists in the edge spectrum, the Majorana fermion will emerge at the edge of the system.

We first discuss the pure s -wave and d -wave superconductors in case (b)-(e) of Tab. 2.1. Note that the appearance of imaginary part of the superconducting gap function, Δ_{s_2} and Δ_{d_2} , will lower the symmetry of the BdG Hamiltonian Eq. (2.7) by breaking the chiral symmetry or partial particle-hole symmetry. The four topological indices, \mathcal{P} , \mathcal{W} , $\mathcal{P}(k_y)$ and $\mathcal{W}(k_y)$, play different roles in characterizing the topological properties of the system. On one hand, \mathcal{P} or \mathcal{W} can be interpreted as a bulk index to indicate whether or not a region in the phase diagram is topological; on the other hand, $\mathcal{P}(k_y)$ or $\mathcal{W}(k_y)$ serves as an edge index to indicate that if there exists topological phase at each k_y in the edge Brillouin zone. More specifically, when $\mathcal{P}(k_y) = -1$ or $\mathcal{W}(k_y)$ is odd, the Hamiltonian is topologically nontrivial and the Majorana bound states will emerge at some range of k_y . Therefore, these continuous zero-energy Majorana bound states in the edge Brillouin zone will form a stable Majorana flat band when the edge index exists. Note that the winding number $\mathcal{W}(k_y)$ can be changed by some even number in the same phase. However, its parity, the Pfaffian invariant $\mathcal{P}(k_y)$ is unchanged in the same phase since $\mathcal{P}(k_y) = (-1)^{\mathcal{W}(k_y)}$. The phase diagrams of case (b)-(e) are topologically equivalent and shown in Fig. 2.5(a). From Tab. 2.1, we find that there exists edge index, $\mathcal{P}(k_y)$ or $\mathcal{W}(k_y)$, in all cases except case (e). Therefore, the edge spectra of pure s -wave and $d_{x^2-y^2}$ -wave superconductors are Majorana flat bands and exhibited in Fig. 2.6(a) and 2.6(c) which correspond to case (c) and (d) respectively. From the edge spectra, we observe that there are odd number of Majorana flat bands in the nontrivial topological phase. The edge indices, $\mathcal{P}(k_y)$ and/or $\mathcal{W}(k_y)$, are also depicted in Fig. 2.6(b) and 2.6(d). We find that there is only one edge index survived in case (c) due to the breaking of chiral symmetry. Comparing the edge spectra with the edge indices in Fig. 2.6(a)-2.6(d), we can see that the location of the Majorana flat bands is consistent with the Pfaffian invariant $\mathcal{P}(k_y)$ and/or the winding number $\mathcal{W}(k_y)$. In addition, due to the lack of edge index in the $d_{x^2-y^2} + id_{xy}$ -wave superconductor, the Majorana flat band disappears and becomes Dirac cone as shown in Fig. (2.7).

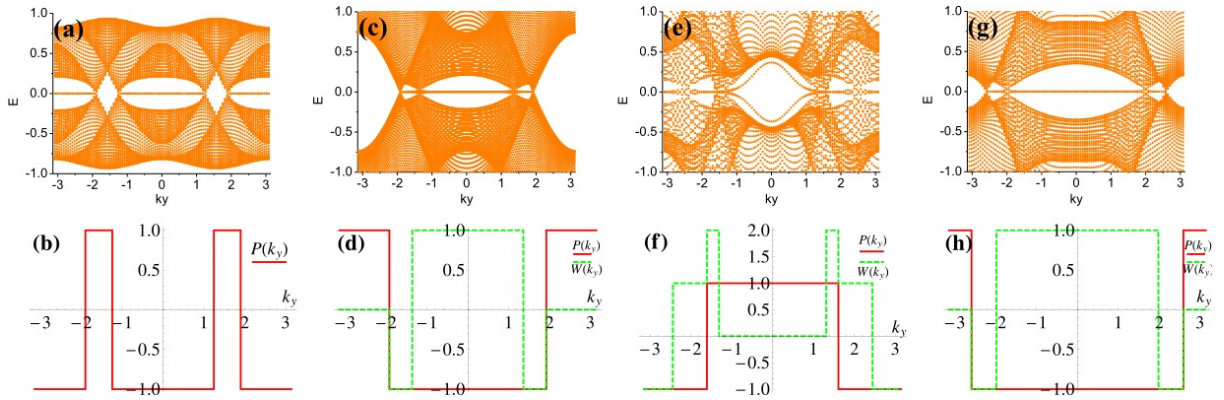


Figure 2.6: The edge spectra and topological invariants of the spin-singlet superconductor with Dresselhaus (110) spin-orbit coupling. The open edges are at $i_x = 0$ and $i_x = 50$, k_y denotes the momentum in the y direction and $k_y \in (-\pi, \pi]$. (a) is the edge spectrum of s -wave superconductor. The parameters are $t = 1$, $\beta = 1$, $\Delta_{s_1} = 1$, $\Delta_{s_2} = 1$, $\mu = 0$, $V^2 = 9$ and correspond to a point in region II of Fig. 2.5(a). (c) is the edge spectrum of $d_{x^2-y^2}$ -wave superconductor. The parameters are $t = 1$, $\beta = 1$, $\Delta_{d_1} = 1$, $\Delta_{d_2} = 0$, $\mu = -4$, $V^2 = 9$ and correspond to a point in region I of Fig. 2.5(a). (e) and (g) are the edge spectra of $d_{x^2-y^2} + s$ -wave superconductor. The parameters are $\beta = 1$, $\Delta_{s_1} = 1$, $\Delta_{d_1} = 2$ and (e) $t = 2$, $\mu = 0$, $V^2 = 16$, (g) $t = 1$, $\mu = -4.5$, $V^2 = 25$ which correspond to region I of Fig. 2.5(b) and region IV of Fig. 2.5(c) respectively. (b), (d), (f) and (h) are the Pfaffian invariant $\mathcal{P}(k_y)$ and/or winding number $\mathcal{W}(k_y)$ for the corresponding cases.

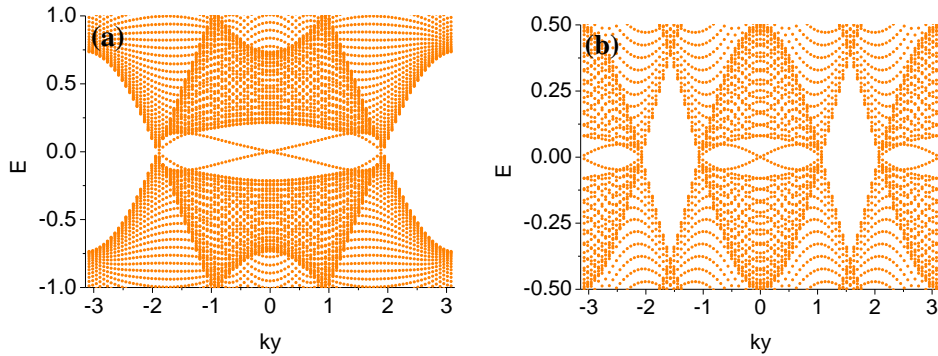


Figure 2.7: (a) and (b) are the edge spectra of the $d_{x^2-y^2} + id_{xy}$ -wave superconductor with Dresselhaus (110) spin-orbit coupling in case (e). The parameters are $t = 1$, $\beta = 1$, $\Delta_{d_1} = 1$, $\Delta_{d_2} = 1$ and (a) $\mu = -4$, $V^2 = 9$, (b) $\mu = 0$, $V^2 = 9$, which correspond to regions I and II in Fig. 2.5(a).

We now turn to discuss the superconductors with mixed s -wave and d -wave pairing symmetries as listed in case (a), (f) and (g) of Tab. 2.1. For each case, there are three different kinds of phase diagrams depending on the hopping amplitude t as demonstrated in Fig. 2.5(b)-2.5(d). The edge spectra for the mixed pairing superconductors are similar to their pure pairing counterparts. Notice that the Majorana flat bands will emerge only in $d_{x^2-y^2} + s$ -wave superconductor in case (f) because in the other two cases there is no edge index to make the Majorana flat bands stable. The edge spectra for the $d_{x^2-y^2} + s$ -wave superconductor with Dresselhaus (110) spin-orbit coupling are shown in Fig. 2.6(e) and 2.6(g) which correspond to region I in Fig. 2.5(b) and region IV in Fig. 2.5(c) respectively. The edge indices associated with them are also depicted in Fig. 2.6(f) and 2.6(h) (for fully details of this case, please see Appendix A). Note that the winding number $\mathcal{W}(k_y)$ in some range of k_y can be 2, however, it is topologically trivial because its parity, namely the Pfaffian invariant $\mathcal{P}(k_y)$ is 1. For the $d_{x^2-y^2} + id_{xy} + s$ -wave superconductor with Rashba/Dresselhaus (110) spin-orbit coupling in case (a) and (g), without the protection of edge indices, the edge spectra become Dirac cones and have no qualitative differences to the $d_{x^2-y^2} + id_{xy}$ -wave superconductor. We have put the details into Appendix A.

Comparing the edge spectra with the edge indices in Fig. 2.6, we find that the location of Majorana flat bands can be determined by the edge indices. This result holds true for the switched boundary condition, namely, periodic boundary in the x direction and open in the y direction. From the symmetries of Hamiltonian exhibited in Tab. 2.1, only for the Hamiltonian with chiral symmetry Eq. (2.30) can we define edge index $\mathcal{W}(k_x)$ in the switched boundary condition,

$$\begin{aligned}\mathcal{W}(k_x) &= -\frac{1}{4\pi} \int_{-\pi}^{\pi} dk_y \text{tr}[\Sigma \mathcal{H}^{-1}(\mathbf{k}) \partial_{k_y} \mathcal{H}(\mathbf{k})], \\ &= -\frac{1}{2\pi i} \int_{-\pi}^{\pi} dk_y \text{tr}[q^{-1}(\mathbf{k}) \partial_{k_y} q(\mathbf{k})].\end{aligned}\tag{2.50}$$

Therefore, we will consider cases (b), (d) and (f) in the switched boundary condition. It is worth noting that $\mathcal{W}(k_x)$ is always zero in these three cases. Thus we obtain an interesting result that the Majorana flat bands only exist along the y direction. This is due to the space asymmetry of Dresselhaus (110) spin-orbit coupling Eq. (2.5). Here we directly give the edge spectra and edge index in the switched boundary condition as shown in Fig. 2.8. The parameters chosen in Fig. 2.8 are the same as the one in Fig. 2.6 except that Fig. 2.8(a) is the same as Fig. 2.3(a). We can see that $\mathcal{W}(k_x) = 0$ in

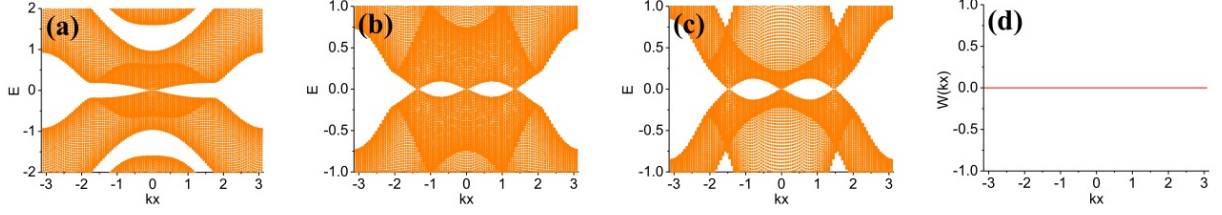


Figure 2.8: The edge spectra and edge index in the switched boundary condition. The open edges are at $i_y = 0$ and $i_y = 100$, k_x denotes the momentum in the x direction and $k_x \in (-\pi, \pi]$. (a) is the edge spectrum of the s -wave superconductor. The parameters are $t = 1$, $\beta = 1$, $\Delta_{s_1} = 1$, $\Delta_{s_2} = 0$, $\mu = -4$, $V^2 = 5$ and correspond to a point in region I of Fig. 2.5(a). (b) is the edge spectrum of the $d_{x^2-y^2}$ -wave superconductor. The parameters are $t = 1$, $\beta = 1$, $\Delta_{d_1} = 1$, $\Delta_{d_2} = 0$, $\mu = -4$, $V^2 = 9$ and correspond to a point in region I of Fig. 2.5(a). (c) is the edge spectrum of the $d_{x^2-y^2} + s$ -wave superconductor. The parameters are $t = 1$, $\beta = 1$, $\Delta_{s_1} = 1$, $\Delta_{d_1} = 2$, $\mu = -4.5$, $V^2 = 25$ and correspond to a point in region IV of Fig. 2.5(c). (d) is the edge index $\mathcal{W}(k_x) = 0$ for all the cases.

the whole edge Brillouin zone and there is no Majorana flat band along the x direction. However, the parameters chosen are in the topological nontrivial phase and we indeed find the Majorana flat bands along the y direction as shown in Fig. 2.6.

Notice that the Majorana flat band does not always situate at the edge of the system. At a fixed k_y , the bigger the gap of bulk state is, the more localized the Majorana bound state is. Let us take the edge spectra of the $d_{x^2-y^2}$ -wave superconductor with the Dresselhaus (110) spin-orbit coupling in Fig. 2.6(c) as an example. The probability distribution of the quasiparticle at $k_y = 0, 1, 1.3$ are shown in Fig. 2.9. From Fig. 2.6(c), we see that the gap of the bulk state decreases as k_y increases from 0 to 1.3. At the same time, the probability distribution of the quasiparticle becomes more and more delocalized and finally extends into the bulk. Therefore, only the big-gap Majorana bound states in the flat bands are well-defined Majorana particles.

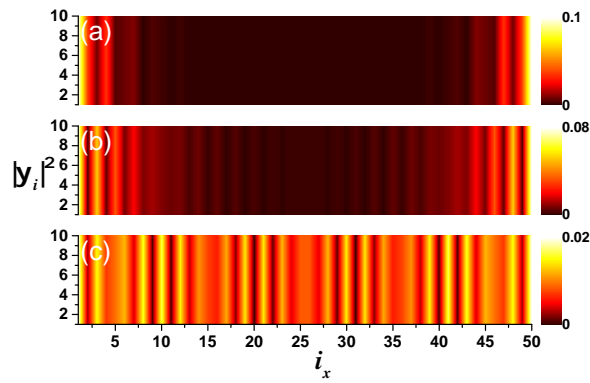


Figure 2.9: The probability distributions of the Majorana fermion in the $d_{x^2-y^2}$ -wave superconductor with Dresselhaus (110) spin-orbit coupling in the edge Brillouin zone of $k_y = 0, 1, 1.3$. i_x is the lattice site. $|\psi_{i_x}|^2$ is the probability of quasiparticle at site i_x .

Chapter 3

Majorana transport in superconducting nanowire with Rashba and Dresselhaus spin-orbit couplings

3.1 Introduction

An intensive search is ongoing in experimental realization of topological superconductor for topological quantum computing [3; 51; 90; 125; 130; 131; 134; 166; 169; 170]. The basic idea is to embed qubit in a nonlocal, intrinsically decoherence-free way. The prototype is a spinless p -wave superconductor [70; 79; 80]. Edge excitations in such a state are Majorana fermions (MFs) which obey non-Abelian statistics and can be manipulated by braiding operations. The nonlocal MFs are robust against local perturbations and have been proposed for topological quantum information processing [4; 24].

A hybrid semiconducting-superconducting nanostructure has become a mainstream experimental setup recently for realizing topological superconductor and Majorana fermion [3; 45; 99; 119; 134]. The signature of MFs characterized by a zero-bias conductance peak (ZBP) has been reported in the tunneling experiments of the InSb nanowire [23; 27; 31; 40; 91; 109]. Motivated by this, we propose a two-lead setup for studying the tunneling transport of MFs as shown in Fig. 3.1. A spin-orbit coupled InSb nanowire is deposited on an s -wave superconductor. Due to the superconducting proximity effect, the wire is effectively equivalent to the spinless p -wave superconductor and hosts

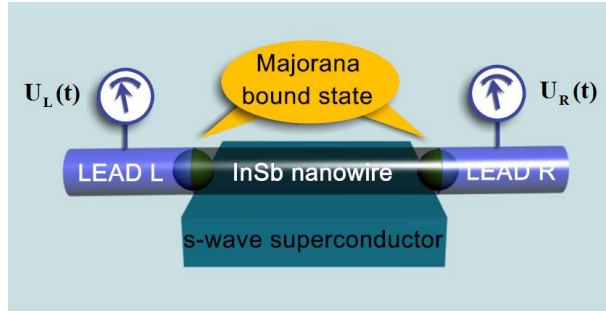


Figure 3.1: Experimental setup for tunneling experiment. An InSb nanowire is deposited on an s -wave superconductor and coupled to two normal metal leads.

MFs at the ends. The nanowire is then coupled to two normal metal leads so as to measure the currents. For our study, we apply the Keldysh non-equilibrium Green function (NEGF) method to obtain the current response of the tunneling Hamiltonian [12; 30; 32; 36; 42; 71; 86; 100; 106; 173; 175]. Curiously in the two-lead case, we observe that the currents at left and right leads are asymmetric as shown in Fig. 3.2. This is due to the exotic commutation relation of MFs, $\{\gamma_i, \gamma_j\} = 2\delta_{i,j}$. From another standpoint, the zero-energy fermion b_0 combined by the end-Majorana modes ($\gamma_{L,R}$) is so highly nonlocal, $b_0 = (\gamma_L + i\gamma_R)/2$, as to make the Majorana transport deviate from the ordinary transport mediated by electron. Different from the ordinary one, there is a hole transmission channel in Eq. (3.28) in Majorana transport. This makes the left and right currents asymmetric. The current asymmetry may be used as a criterion to further confirm the existence of Majorana fermion in our two-lead setup. We also give the ac current response in the thesis and find that the current is enhanced in step with the increase of level broadening and the decrease of temperature, and finally saturates at high voltage. We use the bosonization and renormalization group (RG) methods to consider the transport property of the Majorana nanowire with short-range Coulomb interaction and disorder [20; 39; 44; 48; 52; 53; 69; 96; 97; 133; 145]. We observe that there is a topological quantum phase transition under the interplay of superconductivity and disorder. It is found that the Majorana transport is preserved in the superconducting-dominated topological phase and destroyed in the disorder-dominated non-topological insulator phase. The phase diagram and the condition in which the Majorana transport exists are given.

The main results of this chapter were published in the following paper:

- Jia-Bin You, Xiao-Qiang Shao, Qing-Jun Tong, A. H. Chan, C. H. Oh, and Vlatko

Vedral, *Majorana transport in superconducting nanowire with Rashba and Dresselhaus spin-orbit couplings*. *Journal of Physics: Condensed Matter* **27**, 225302 (2015).

3.2 Model

The model is depicted in Fig. 3.1. Two normal metal leads are connected to the superconducting wire through ohmic contacts at the two ends. When the chemical potential of superconducting wire lies within the energy gap, two MFs will appear at the two ends of the wire respectively. The topological superconducting wire is made of a spin-orbit coupled semiconductor (InSb wire) deposited on an s -wave superconducting substrate. Via the superconducting proximity effect [45], the Cooper pair will tunnel into the semiconductor and generate the s -wave superconductivity in the semiconducting wire.

The one dimensional spin-orbit coupled s -wave superconducting nanowire can be modeled as $H_{\text{nw}} = H_0 + H_\Delta$ [37; 145], where

$$\begin{aligned} H_0 &= \int dk \Psi_k^\dagger [\xi_k + (\alpha\tau_y + \beta\tau_x)k + V_z\tau_z] \Psi_k, \\ H_\Delta &= \Delta \int dk (a_{k\uparrow}a_{-k\downarrow} + \text{H.c.}). \end{aligned} \quad (3.1)$$

Here $\xi_k = k^2/2m - \mu$ where k is the momentum and μ is the chemical potential, τ_x and τ_y are spin Pauli matrices, α and β are the Rashba and Dresselhaus spin-orbit strengths, Δ is the s -wave gap function and $\Psi_k = (a_{k\uparrow}, a_{k\downarrow})^T$ where $a_{k\uparrow}$ ($a_{k\downarrow}$) is the annihilation operator for spin up (down) electron. We also exert a perpendicular magnetic field V_z on the wire and consider the Zeeman effect.

In the Nambu basis $\Phi_k^\dagger = (\Psi_k^\dagger, \Psi_{-k})$, the Hamiltonian Eq. (3.1) can be recast into $H = \frac{1}{2} \int dk \Phi_k^\dagger \mathcal{H}(k) \Phi_k$, where

$$\mathcal{H}(k) = \xi_k\tau_z + \alpha k\tau_z\sigma_y + \beta k\sigma_x + \Delta\tau_y\sigma_y + V_z\tau_z\sigma_z. \quad (3.2)$$

Here σ_x , σ_y and σ_z are the Pauli matrices in the particle-hole space. It is known that the BdG Hamiltonian Eq. (3.2) satisfies the particle-hole symmetry, $\Xi^{-1}\mathcal{H}(k)\Xi = -\mathcal{H}(-k)$, where $\Xi = \tau_x K$ and K is the complex conjugation operator [169; 170]. The topological

property of this BdG Hamiltonian can be examined by the Pfaffian invariant [79],

$$\mathcal{P} = \text{sgn} \{ \text{Pf}[\mathcal{H}(k=0)\tau_x] \} = \text{sgn}(\mu^2 + \Delta^2 - V_z^2). \quad (3.3)$$

Therefore, a topological quantum phase transition occurs when $\mu^2 + \Delta^2 = V_z^2$. For $\mu^2 + \Delta^2 < V_z^2$, $\mathcal{P} = -1$, the gap is dominated by the magnetic field and the wire is in the topological phase with Majorana fermion at the ends of the nanowire. For $\mu^2 + \Delta^2 > V_z^2$, $\mathcal{P} = 1$, the gap is dominated by pairing with no end states. In this thesis, we study the case where the nanowire is in the topological phase. This can be realized by putting the chemical potential inside the energy gap. The low energy theory of the Hamiltonian Eq. (3.1) can then be obtained as follow. By diagonalizing the Hamiltonian H_0 , we get two energy bands, $\varepsilon_{\pm}(k) = \frac{k^2}{2m} - \mu \pm \sqrt{(\alpha^2 + \beta^2)k^2 + V_z^2}$. For these two bands, the eigenstates are

$$|\chi_+(k)\rangle = \begin{bmatrix} e^{-i\theta/2} \cos \frac{\gamma_k}{2} \\ e^{i\theta/2} \sin \frac{\gamma_k}{2} \end{bmatrix}, |\chi_-(k)\rangle = \begin{bmatrix} -e^{-i\theta/2} \sin \frac{\gamma_k}{2} \\ e^{i\theta/2} \cos \frac{\gamma_k}{2} \end{bmatrix}, \quad (3.4)$$

respectively, where $\tan \theta = \alpha/\beta$ and $\tan \gamma_k = \sqrt{\alpha^2 + \beta^2}k/V_z$. When the magnetic field is dominant than the spin-orbit interactions ($V_z \gg \alpha, \beta$), $\gamma_k \approx 0$, then the spins will be forced to be nearly polarized within each band. Because the chemical potential lies within the gap, only the low energy band is near the Fermi points and activated. We can thus restrict the Hilbert space to the lower band in this case [45]. To achieve this, we unitarily transform the electron operator from spin basis to band basis, $(a_{k+}^\dagger, a_{k-}^\dagger) = (a_{k\uparrow}^\dagger, a_{k\downarrow}^\dagger)U$, where $U = (|\chi_+(k)\rangle, |\chi_-(k)\rangle)$. Here a_{k+}^\dagger (a_{k-}^\dagger) is the creation operator for upper (lower) band. Then we neglect the upper band and obtain the low energy approximation of the Hamiltonian

$$H_0 = \int dk \varepsilon_-(k) d_k^\dagger d_k, \quad (3.5)$$

where $d_k \equiv a_{k-}$. Similarly, projecting the superconducting term onto the lower band $|\chi_-(k)\rangle$, we have

$$H_\Delta = -\frac{\Delta}{2} \int dk (\sin \gamma_k d_k d_{-k} + \text{H.c.}). \quad (3.6)$$

Therefore, the low energy theory for the topological superconductivity in the spin-orbit coupled semiconducting nanowire deposited on an *s*-wave superconductor is exhibited

by $H_{\text{nw}} = \int dk(k^2/2m - \mu_{\text{eff}})d_k^\dagger d_k - \Delta_{\text{eff}}(kd_k d_{-k} + \text{H.c.})$, where $\mu_{\text{eff}} = \mu + |V_z|$ and $\Delta_{\text{eff}} = \frac{\Delta\sqrt{\alpha^2 + \beta^2}}{2|V_z|}$. The Hamiltonian H_{nw} is exactly the spinless p -wave superconductor and has been shown that [79] there exist unpaired Majorana fermions at the left and right end sides of the nanowire. The effective Hamiltonian for this piece of the system is

$$H_{\text{mf}} = \frac{i}{2}t(\gamma_L\gamma_R - \gamma_R\gamma_L), \quad (3.7)$$

where $\gamma_{L/R}$ is the Majorana operator at the left/right end side and $t \sim e^{-L/l_0}$ describes the coupling energy between the two MFs, L is the length of wire, and l_0 is the superconducting coherence length.

We next focus on the tunneling transport of Majorana nanowire described by H_{mf} . Guided by the typical experimental setup in which the leads are made of gold, we view electrons in the leads as noninteracting. We then apply time-dependent bias voltages on the left and right leads respectively. This can be physically described by

$$H_s = \sum_p \xi_{p,s}(t)c_{p,s}^\dagger c_{p,s}, \quad (3.8)$$

where $s = L, R$, and $c_{p,s}$ is the electron annihilation operator for the lead. Here $\xi_{p,s}(t) = \varepsilon_{p,s} - eU_s(t)$, where $\varepsilon_{p,s}$ is the dispersion relation for the metallic lead and $U_s(t)$ is the time-dependent bias voltage on the lead. Note that the occupation for each lead is determined by the equilibrium distribution function established before the time-dependent bias voltage and tunneling are turned on. The tunneling between the leads and the wire is dependent upon the geometry of experimental layout and upon the self-consistent response of charge in the leads to the time-dependent bias voltages [71]. We can simply express the tunneling as

$$H_{T,s} = \sum_{pi} [V_{pi,s}^*(t)c_{p,s}^\dagger - V_{pi,s}(t)c_{p,s}] \gamma_i, \quad (3.9)$$

where $i, s = L, R$, and $V_{pi,s}(t)$ is the tunneling strength. Note that the Majorana operator becomes $\gamma_i \sim c_i + c_i^\dagger$, therefore the tunneling term does not have electron conservation and contains pairing $c_{p,s}^\dagger c_i^\dagger$ which leads to the current asymmetry discussed in Sec. 3.3.2. The Hamiltonian for the experimental setup of Fig. 3.1 can be described by $H = H_L + H_{TL} + H_{\text{mf}} + H_{TR} + H_R$.

3.3 NEGF method for the Majorana current

The Keldysh nonequilibrium Green function technique is used very widely to describe transport phenomena in mesoscopic systems. In the tunneling problem formulated in Sec. 3.2, we have considered the time-dependent bias voltages and tunneling strengths. This is essentially a nonequilibrium problem and can be treated by the Keldysh formalism [71]. In this formalism, the leads and the wire are decoupled and each part is in thermal equilibrium characterized by their respective chemical potentials at $t = -\infty$. We first adiabatically evolve the system by the total Hamiltonian H from $t = -\infty$ to $t = +\infty$, then evolve the system back in time from $t = +\infty$ to $t = -\infty$, and calculate the physical quantity during this evolution. Finally the system is back in the initial state at $t = -\infty$. This procedure eliminates the uncertain state at the asymptotically large time in the nonequilibrium theory [101]. The time loop, which contains two pieces: the outgoing branch from $t = -\infty$ to $t = +\infty$ and the ingoing branch from $t = +\infty$ to $t = -\infty$, is called Keldysh contour. Below we will use the Keldysh NEGF method to study the Majorana current in the tunneling transport. For more details of the Keldysh Green function, please refer to Appendix B.

3.3.1 general formula

We study the Majorana current from the left/right lead to the wire. The current is given by the changing rate of charge in the lead, $I_s = -e\langle\dot{N}_s\rangle$, where $s = L, R$, N_s is the number operator in the lead, $N_s = \sum_p c_{p,s}^\dagger c_{p,s}$. The bracket $\langle\rangle$ denotes the ensemble average with respect to the total Hamiltonian H . The commutation relations of electrons and MFs are $\{c_{p,s}, c_{p',s'}^\dagger\} = \delta_{p,p'}\delta_{s,s'}$ and $\{\gamma_i, \gamma_j\} = 2\delta_{i,j}$, and zero otherwise. Using the Heisenberg equation, the current from the lead to the wire is

$$\begin{aligned}
I_s(t) &= -e\langle\dot{N}_s\rangle = -ie\langle[H, N_s]\rangle = -ie\langle[H_{T,s}, N_s]\rangle, \\
&= ie \sum_{pi} \langle V_{pi,s}^*(t) c_{p,s}^\dagger \gamma_i - V_{pi,s}(t) \gamma_i c_{p,s} \rangle, \\
&= 2e \sum_{pi} \text{Re}\{V_{pi,s}^*(t) \langle i c_{p,s}^\dagger \gamma_i \rangle\}, \\
&= 2e \sum_{pi} \text{Re}\{V_{pi,s}^*(t) G_{ip,s}^<(t, t)\},
\end{aligned} \tag{3.10}$$

where $G_{ip,s}^<(t, t') = i\langle c_{p,s}^\dagger(t')\gamma_i(t) \rangle$ is the lesser component of the Keldysh Green function

$$G_{ip,s}(t, t') = -i\langle T_K \gamma_i(t) c_{p,s}^\dagger(t') \rangle. \quad (3.11)$$

Here operator T_K orders the times along the Keldysh contour with earlier times occurring first.

To proceed, we express the coupling Green function G_{ip} as a product of Green functions for the lead G_p and the wire G_{ij} . Via the equation of motion (EOM) method (see Ref. [101] and Appendix C for details), we have

$$G_{ip,s}(t, t') = \sum_j \int_K dt'' G_{ij}(t, t'') V_{pj,s}(t'') G_{p,s}^0(t'', t'), \quad (3.12)$$

where

$$\begin{aligned} G_{ij}(t, t') &= -i\langle T_K \gamma_i(t) \gamma_j(t') \rangle, \\ G_{p,s}^0(t, t') &= -i\langle T_K c_{p,s}(t) c_{p,s}^\dagger(t') \rangle_0 \end{aligned} \quad (3.13)$$

are the Green function of the wire and the free Green function of the lead respectively. Here $\langle \rangle_0$ is the ensemble average with respect to the Hamiltonian of lead H_s . The integration is taken on the Keldysh contour. Therefore, via the Keldysh Green function method [101], we can get the lesser component of the coupling Green function Eq. (3.12) by analytic continuation (see Appendix B for details),

$$G_{ip,s}^<(t, t') = \sum_j \int_{-\infty}^{\infty} dt'' V_{pj,s}(t'') [G_{ij}^R(t, t'') G_{p,s}^{0<}(t'', t') + G_{ij}^<(t, t'') G_{p,s}^{0A}(t'', t')], \quad (3.14)$$

where G^R and G^A are the retarded and advanced Green functions. The explicit expressions for the free Green functions G^0 can be found in Appendix D. Substituting this lesser Green function into the current formula Eq. (3.10) and using the expressions for the free Green functions, we arrive at

$$I_s(t) = -2e\text{Im} \left\{ \sum_{ij} \int_{-\infty}^t dt_1 \int_{-\infty}^{\infty} \frac{d\varepsilon}{2\pi} e^{i\varepsilon(t-t_1)} [\Gamma_s(\varepsilon, t_1, t)]_{ji} [G_{ij}^R(t, t_1) f_s(\varepsilon) + G_{ij}^<(t, t_1)] \right\}, \quad (3.15)$$

where $f_s(\varepsilon)$ is the Fermi function. The time-dependent level broadening matrix is given

by

$$[\Gamma_s(\varepsilon, t_1, t)]_{ji} = 2\pi\rho_s(\varepsilon)V_{i,s}^*(\varepsilon, t)V_{j,s}(\varepsilon, t_1)e^{-ie\int_{t_1}^t dt_2 U_s(t_2)}, \quad (3.16)$$

where the density operator is $\rho(\varepsilon) = \sum_p \delta(\varepsilon - \varepsilon_{p,s})$. Here we have explicitly indicated the energy dependence of the tunneling strength $V_{pi,s}(t)$. It is easy to check that the broadening matrix is Hermitian, $\mathbf{\Gamma}_s^\dagger(\varepsilon, t_1, t) = \mathbf{\Gamma}_s(\varepsilon, t, t_1)$.

Since transport is often dominated by the states close to the Fermi level and the broadening function is slowly varying function of energy, we apply the wide-band approximation [71] to the tunneling strength. The momentum and time dependence can thus be factorized, $V_{pi,s}(t) = V_{i,s}(\varepsilon_{p,s}, t) = u_s(t)V_{i,s}(\varepsilon_{p,s})$. Thus we find that $[\Gamma_s(t)]_{ji} \equiv [\Gamma_s(\varepsilon, t, t)]_{ji} = [\Gamma_s(\varepsilon)]_{ji}|u_s(t)|^2$, where the level broadening matrix is

$$[\Gamma_s(\varepsilon)]_{ji} = 2\pi\rho_s(\varepsilon)V_{i,s}^*(\varepsilon)V_{j,s}(\varepsilon). \quad (3.17)$$

Below we assume that the tunneling strength is time-independent and set $u_s(t) = 1$. In the mesoscopic transport, the physical property is generally dominated by states near the Fermi level. Since the broadening matrix is usually slowly varying function of energy close to the Fermi level, we can assume that it is energy-independent, $\mathbf{\Gamma}_s(\varepsilon) = \mathbf{\Gamma}_s$. This wide-band approximation captures the main physics of the tunneling problem and can be used to simplify the current expression Eq. (3.15).

Therefore, the current can be further reduced to $I_s(t) = I_s^{\text{out}}(t) + I_s^{\text{in}}(t)$, where

$$\begin{aligned} I_s^{\text{out}}(t) &= -e\text{ImTr}[\mathbf{\Gamma}_s \mathbf{G}^<(t, t)], \\ I_s^{\text{in}}(t) &= -e\text{ImTr}\left\{ \int_{-\infty}^{\infty} \frac{d\varepsilon}{\pi} f_s(\varepsilon) \int_{-\infty}^t dt_1 e^{-ie\varepsilon(t_1-t)} \mathbf{\Gamma}_s(t_1, t) \mathbf{G}^R(t, t_1) \right\}. \end{aligned} \quad (3.18)$$

Here $\mathbf{\Gamma}_s(t_1, t) \equiv \mathbf{\Gamma}_s(\varepsilon, t_1, t) = \mathbf{\Gamma}_s e^{-ie\int_{t_1}^t dt_2 U_s(t_2)}$ and $\mathbf{G}^{<,R}$ are the Green functions of the wire. The current has been separated in two parts: the outflow, $I_s^{\text{out}}(t)$, which is easy to be identified since $\mathbf{\Gamma}_s$ represents the rate at which an electron placed initially in the energy level of the wire will escape into the lead and $N(t) = \text{ImTr}[\mathbf{G}^<(t, t)]$ is the number of particles in the wire; the inflow, $I_s^{\text{in}}(t)$, which is proportional to the occupation $f_s(\varepsilon)$ in the lead and to the density of states $\rho(\varepsilon) = \text{ImTr}[\mathbf{G}^R(\varepsilon)]$ in the wire. For the outflow, the lesser Green function can be calculated by the relation [30]

$$\mathbf{G}^<(t, t) = \int dt_1 dt_2 \mathbf{G}^R(t, t_1) \mathbf{\Sigma}^<(t_1, t_2) \mathbf{G}^A(t_2, t), \quad (3.19)$$

where the explicit expression for the lesser self-energy $\Sigma^<(t_1, t_2)$ is given in Appendix C. Substituting $\Sigma^<$ into the lesser Green function, we have

$$\mathbf{G}^<(t, t) = \sum_{s=L,R} \int \frac{d\varepsilon}{2\pi} [if_s(\varepsilon)] [\mathbf{A}_s(\varepsilon, t) \mathbf{\Gamma}_s \mathbf{A}_s^\dagger(\varepsilon, t) + \mathbf{B}_s(\varepsilon, t) \mathbf{\Gamma}_s^* \mathbf{B}_s^\dagger(\varepsilon, t)], \quad (3.20)$$

where

$$\begin{aligned} \mathbf{A}_s(\varepsilon, t) &= \int dt_1 e^{-i\varepsilon(t_1-t)} e^{ie \int_t^{t_1} dt' U_s(t')} \mathbf{G}^R(t, t_1), \\ \mathbf{B}_s(\varepsilon, t) &= \int dt_1 e^{-i\varepsilon(t_1-t)} e^{-ie \int_t^{t_1} dt' U_s(t')} \mathbf{G}^R(t, t_1). \end{aligned} \quad (3.21)$$

Since $\text{Tr}[\mathbf{\Gamma}_s \mathbf{A} \mathbf{\Gamma}_{s'} \mathbf{A}^\dagger]$ is real, the outflow can be finally written as

$$I_s^{\text{out}}(t) = -e \sum_{s'=L,R} \int \frac{d\varepsilon}{2\pi} f_{s'}(\varepsilon) \text{Tr} \{ \mathbf{\Gamma}_s \mathbf{A}_{s'}(\varepsilon, t) \mathbf{\Gamma}_{s'} \mathbf{A}_{s'}^\dagger(\varepsilon, t) + \mathbf{\Gamma}_s \mathbf{B}_{s'}(\varepsilon, t) \mathbf{\Gamma}_{s'}^* \mathbf{B}_{s'}^\dagger(\varepsilon, t) \}. \quad (3.22)$$

For the inflow, substituting Eq. (3.21) into Eq. (3.18), we obtain

$$I_s^{\text{in}}(t) = -e \int \frac{d\varepsilon}{\pi} f_s(\varepsilon) \text{Im} \text{Tr} \{ \mathbf{\Gamma}_s \mathbf{A}_s(\varepsilon, t) \}. \quad (3.23)$$

The retarded Green function of the wire is deduced in Appendix C. Here we only show the result,

$$\mathbf{G}^R(t, t_1) = -2i\theta(t - t_1) e^{(2\mathbf{t} - \mathbf{\Gamma})(t - t_1)}, \quad (3.24)$$

where $\theta(t)$ is the Heaviside step function. The level broadening matrix is $\mathbf{\Gamma} = 2(\mathbf{\Gamma}_L + \mathbf{\Gamma}_R)$, where

$$\mathbf{\Gamma}_L = \begin{bmatrix} \Gamma_L & 0 \\ 0 & 0 \end{bmatrix}, \mathbf{\Gamma}_R = \begin{bmatrix} 0 & 0 \\ 0 & \Gamma_R \end{bmatrix}, \quad (3.25)$$

and Γ_L and Γ_R are positive. The hopping matrix are

$$\mathbf{t} = \begin{bmatrix} 0 & t \\ -t & 0 \end{bmatrix}. \quad (3.26)$$

3.3.2 *dc* current response

We first discuss the current response to the *dc* voltages at the two ends, $U_L(t) = U_L$ and $U_R(t) = U_R$. For the homogeneous system, $\mathbf{A}_s(\varepsilon, t)$ and $\mathbf{B}_s(\varepsilon, t)$ in Eq. (3.21) are time-independent and just the Fourier transform of the retarded Green function, $\mathbf{A}_s(\varepsilon, t) = \mathbf{G}^R(\varepsilon - eU_s)$ and $\mathbf{B}_s(\varepsilon, t) = \mathbf{G}^R(\varepsilon + eU_s)$. Substituting this relation into the outflow Eq. (3.22), we immediately have

$$I_s^{\text{out}} = -e \sum_{s'} \int \frac{d\varepsilon}{2\pi} [T_{ss'}^e(\varepsilon) f_{s'}(\varepsilon + eU_{s'}) + T_{ss'}^h(\varepsilon) f_{s'}(\varepsilon - eU_{s'})], \quad (3.27)$$

where the particle and hole transmission functions are

$$\begin{aligned} T_{ss'}^e(\varepsilon) &= \text{Tr}[\mathbf{\Gamma}_s \mathbf{G}^R(\varepsilon) \mathbf{\Gamma}_{s'} \mathbf{G}^A(\varepsilon)], \\ T_{ss'}^h(\varepsilon) &= \text{Tr}[\mathbf{\Gamma}_s \mathbf{G}^R(\varepsilon) \mathbf{\Gamma}_{s'}^* \mathbf{G}^A(\varepsilon)]. \end{aligned} \quad (3.28)$$

Here the retarded Green function $\mathbf{G}^R(\varepsilon)$ is the Fourier transform of Eq. (3.24) and can be explicitly written as

$$\mathbf{G}^R(\varepsilon) = \frac{2}{\begin{bmatrix} \varepsilon + 2i\Gamma_L & -2it \\ 2it & \varepsilon + 2i\Gamma_R \end{bmatrix}}, \quad (3.29)$$

and the advanced Green function is the Hermitian conjugation of the retarded one,

$$\mathbf{G}^A(\varepsilon) = \frac{2}{\begin{bmatrix} \varepsilon - 2i\Gamma_L & -2it \\ 2it & \varepsilon - 2i\Gamma_R \end{bmatrix}}. \quad (3.30)$$

Similarly, the inflow can be written as

$$\begin{aligned} I_s^{\text{in}} &= -e \int \frac{d\varepsilon}{\pi} f_s(\varepsilon + eU_s) \text{Im Tr}\{\mathbf{\Gamma}_s \mathbf{G}^R(\varepsilon)\}, \\ &= -e \int \frac{d\varepsilon}{2\pi i} f_s(\varepsilon + eU_s) \text{Tr}\{\mathbf{\Gamma}_s [\mathbf{G}^R(\varepsilon) - \mathbf{G}^A(\varepsilon)]\}. \end{aligned} \quad (3.31)$$

Here we have used the fact that the retarded and advanced Green functions are conjugated. By the definitions of the retarded and advanced Green functions, we have $\mathbf{G}^R(\varepsilon) - \mathbf{G}^A(\varepsilon) = -i \sum_{s'} \mathbf{G}^R(\varepsilon) (\mathbf{\Gamma}_{s'} + \mathbf{\Gamma}_{s'}^*) \mathbf{G}^A(\varepsilon)$ [101]. Substituting this relation into the

inflow Eq. (3.31), we have

$$I_s^{\text{in}} = e \sum_{s'} \int \frac{d\varepsilon}{2\pi} [T_{ss'}^e(\varepsilon) f_s(\varepsilon + eU_s) + T_{ss'}^h(\varepsilon) f_s(\varepsilon + eU_s)]. \quad (3.32)$$

Therefore, for the *dc* case, the current is reduced to the Landauer-Büttiker formula [30; 106],

$$I_s = e \sum_{s'} \int \frac{d\varepsilon}{2\pi} \{ T_{ss'}^e(\varepsilon) [f_s(\varepsilon + eU_s) - f_{s'}(\varepsilon + eU_{s'})] \\ + T_{ss'}^h(\varepsilon) [f_s(\varepsilon + eU_s) - f_{s'}(\varepsilon - eU_{s'})] \}. \quad (3.33)$$

Here we encounter four transmission functions, T_{LL}^e , T_{LR}^e , T_{LL}^h and T_{LR}^h . The first one injects an electron from the left lead and reflects an electron back to the left lead; this process does not have contribution to the transport. The second one injects an electron from the left lead and detects an electron at the right lead; this is the usual contribution to the transport. The third one injects an electron from the left lead and reflects a hole back to the left lead; this is the Andreev reflection of a superconductor. The fourth one injects an electron from the left lead and detects a hole at the right lead; this is the crossed Andreev reflection [63]. It is worth noting that due to the emergence of MFs ($\gamma = c + c^\dagger$), there exists a hole transmission channel $T_{ss'}^h(\varepsilon)$ in Eq. (3.28) in Majorana transport. This leads to the deviation from ordinary tunneling transport in the normal nanowire [17; 106] and renders the left and right currents asymmetric, $I_L \neq -I_R$. For example, when $\Gamma_L = \Gamma_R = \Gamma$, the quantity $J = I_L + I_R$ is shown in Fig. 3.2. We observe that only when $U_L = -U_R$ ($V = -2U_L$, where $V = U_R - U_L$), J is zero; otherwise, $J \neq 0$ in the $\Gamma \sim V$ plane. It is easy to check that when the hole transmission function $T_{ss'}^h$ vanishes, the current symmetry is recovered, $I_L = -I_R$. This scenario happens in the normal semiconducting nanowire [17; 106], the Anderson model [13; 143] and the quantum dot systems [54; 154]. Therefore, the current asymmetry is a unique feature of the Majorana transport in our two-lead setup and may be served as an indicator of the emergence of the Majorana fermion.

We now investigate differential conductance of the Majorana nanowire at zero temperature ($\beta_{L/R} = \infty$). In the Majorana transport, we should define the current going through the wire as $I = \frac{1}{2}(I_L - I_R)$. When the hole transmission function $T_{ss'}^h = 0$, the definition reduces to the usual one. Without loss of generality, U_L is fixed and we calculate the conductance $dI/dV \sim V$, where $V = U_R - U_L$. After some straightforward

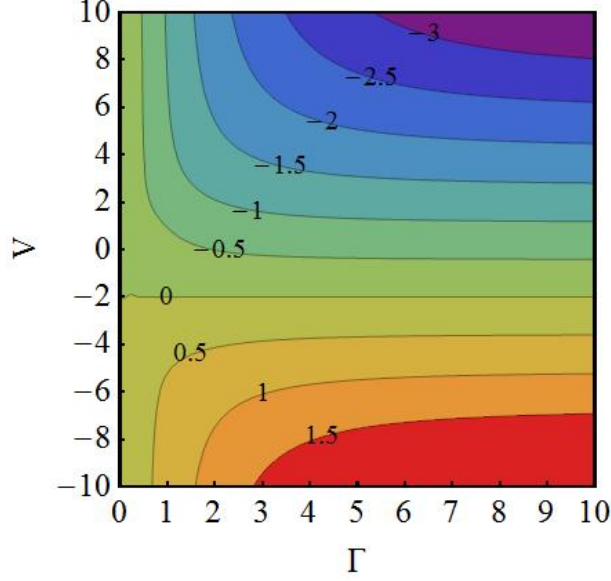


Figure 3.2: Current asymmetry $J = I_L + I_R$ in the $\Gamma \sim V$ plane ranging from -3 to $+1.5$. We set $U_L = 1$ and $\Gamma_L = \Gamma_R = \Gamma$ in this diagram.

calculations, we obtain that

$$\frac{dI}{dV} = \frac{4e^2}{h} \frac{\Gamma_L \Gamma_R (4t^2 + 4\Gamma_L \Gamma_R) + e^2 (V + U_L)^2 \Gamma_R^2}{[4t^2 - e^2 (V + U_L)^2]^2 + (4t^2 + 4\Gamma_L \Gamma_R)^2 - (4t^2)^2 + 4e^2 (V + U_L)^2 (\Gamma_L^2 + \Gamma_R^2)}. \quad (3.34)$$

Notice that when lead L decouples to the Majorana nanowire ($\Gamma_L = U_L = 0$), the conductance reduces to the one in Ref. [42]. Interestingly, we observe that a critical line $\Gamma_R = \Gamma_L^3/t^2 - 2\Gamma_L$ separates the zero-bias conductance peak from zero-bias conductance dip in the $\Gamma_R \sim \Gamma_L$ plane as shown in Fig. 3.3(a). For Γ_L , there exists a critical value $\Gamma_{Lc} = \sqrt{2}t$, below which the zero-bias conductance always exhibits a dip as shown in Fig. 3.3(b). Above this threshold, the zero-bias conductance undergoes a transition from dip to peak as shown in Fig. 3.3(c). We also find that the ZBP becomes larger as the level broadening is increased. The U_L dependence of conductance is also shown in Fig. 3.3(d). It is easy to see that only when $U_L = 0$, the peak is zero-bias, otherwise there is a shift in the V direction. We also study the finite temperature effects as depicted in Fig. 3.3(e) and 3.3(f). As the temperature is increased, the scattering process occurs more frequently, thereby leading to a reduction of the conductance. The competing effect of voltage and temperature can be seen from the intersection of the conductance profiles

as well. Notice that even in the dip region of Fig. 3.3(a), the dip can become a peak at zero-bias voltage as the temperature is increased as shown in Fig. 3.3(e). Although the ZBP above is consistent with the Majorana interpretation, other mechanisms such as impurity, disorder, [26; 126; 150] or zero-bias anomaly of Kondo physics [13; 54; 143; 154] cannot be completely ruled out. In these cases, the currents at the left and right leads remain symmetric, while in the two-lead tunneling transport involving Majorana fermion, the currents are asymmetric. Therefore, the current asymmetry J can be served as an auxiliary criterion for confirming the existence of Majorana fermion in the tunneling experiment as depicted in Fig. 3.1.

3.3.3 *ac* current response

We turn to consider the current response to the *ac* voltages. The harmonic voltages at the two ends of the nanowire are $U_L(t) = U_L \cos \omega_L t$ and $U_R(t) = U_R \cos(\omega_R t + \phi)$ respectively. When the voltage U_R is enhanced, the current becomes less harmonic and finally saturates at high voltage as shown in Fig. 3.4(a). The larger the level broadening Γ_R is, the stronger the coupling between lead and nanowire is. This leads to a higher current response as shown in Fig. 3.4(b). In Fig. 3.4(c), we study the influence of frequency difference of input signals at the left and right lead and find that a more complicated periodic pattern appears. The effect of phase difference is given in Fig. 3.4(d). It is shown that the current response hits the peak when the two voltage signals are out-of-phase. We also study the temperature effect in Fig. 3.4(e) and get similar results as the *dc* case. The response to rectangular *ac* voltages are depicted in Fig. 3.4(f). The upper plane is the voltage signals and the lower plane is the current response. It can be expected that in each plateau, the current response is the same as the *dc* case.

3.4 Interaction and disorder effects on the Majorana transport

The interaction and disorder effects on the topological property of the wire are significant. The disorder will destroy the translational symmetry of the wire. We need to

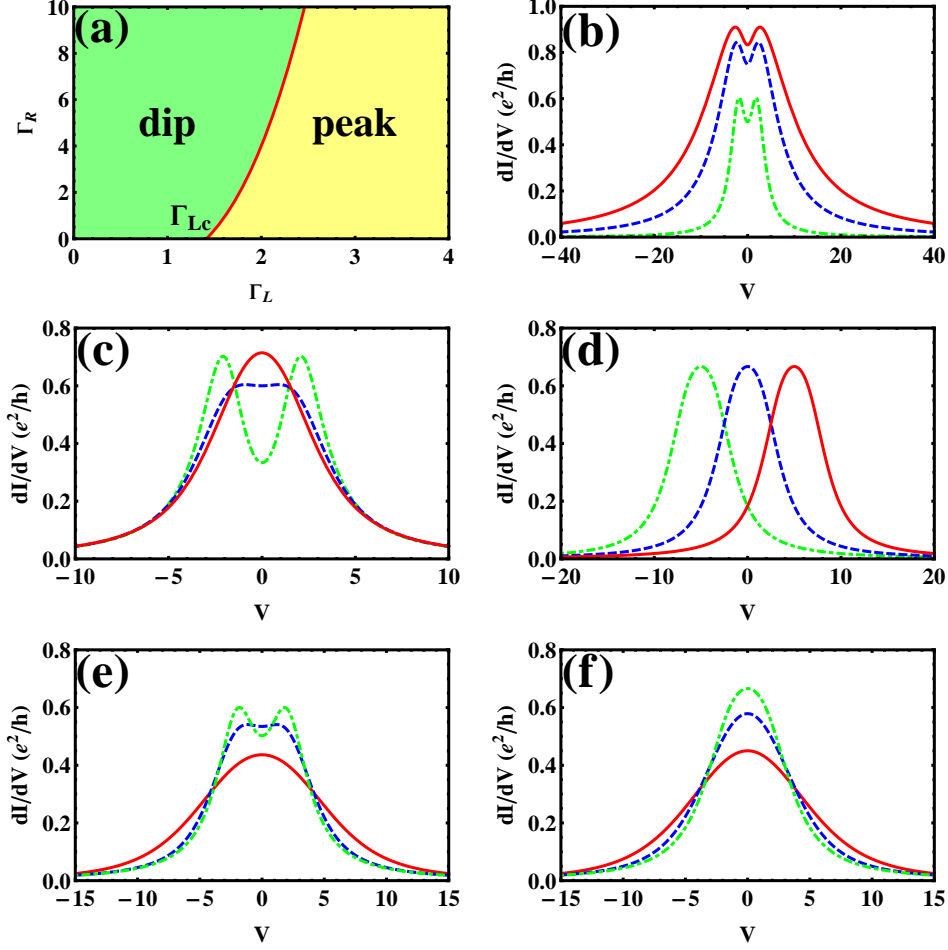


Figure 3.3: Conductance for the dc voltage. We set $t = 1$ in all figures. (a) shows the critical line for the dip-peak transition in the $\Gamma_R \sim \Gamma_L$ plane. The parameters in (b) are $U_L = 0$, $\Gamma_L = 1$ and $\Gamma_R = 1$ (green dot-dashed), 3 (blue dashed), 5 (red solid); in (c) are $U_L = 0$, $\Gamma_R = 1$ and $\Gamma_L = 0.5$ (green dot-dashed), 1.5 (blue dashed), 2.5 (red solid); in (d) are $\Gamma_L = 2$, $\Gamma_R = 1$ and $U_L = 5$ (green dot-dashed), 0 (blue dashed), -5 (red solid); in (e) are $U_L = 0$, $\Gamma_L = \Gamma_R = 1$ and $\beta_L = \beta_R = 10$ (green dot-dashed), 1.5 (blue dashed), 0.5 (red solid); in (f) are $U_L = 0$, $\Gamma_L = 2$, $\Gamma_R = 1$ and $\beta_L = \beta_R = 10$ (green dot-dashed), 1 (blue dashed), 0.5 (red solid).

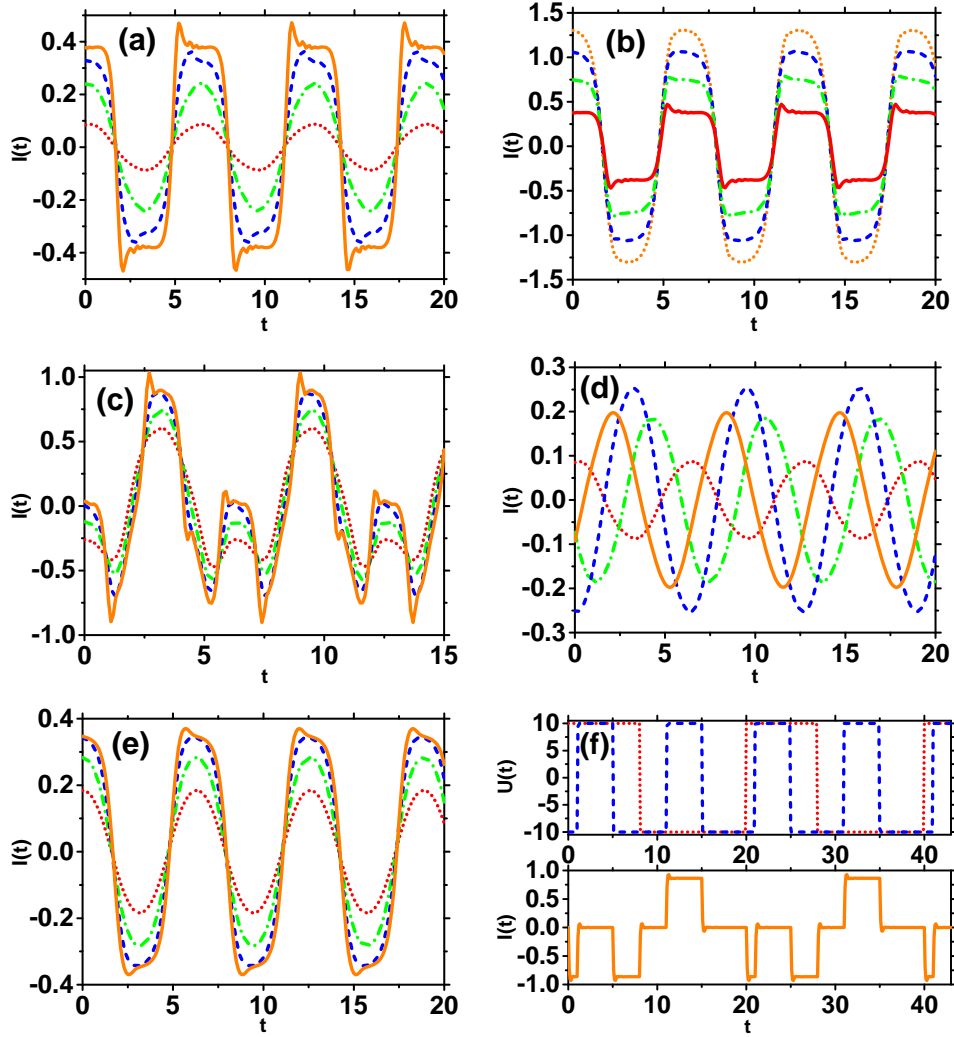


Figure 3.4: Current response to the *ac* voltage. (a) response to the change of U_R with $\omega_L = \omega_R = 1$ and $U_R = 2$ (dot), 4 (dash-dot), 8 (dash), 20 (solid); (b) response to the change of Γ_R with $\Gamma_R = 4$ (dot), 3 (dash), 2 (dash-dot), 1 (solid); (c) response to the change of U_R with $\omega_L = \omega_R/2 = 1$ and $U_R = 2$ (dot), 4 (dash-dot), 8 (dash), 20 (solid); (d) response to the change of ϕ with $\phi = 0$ (dot), $\pi/2$ (dash-dot), π (dash), $3\pi/2$ (solid); (e) response to the change of temperature with $\beta_L = \beta_R = 0.1$ (dot), 0.2 (dash-dot), 0.4 (dash), 1 (solid); (f) response to rectangular signals. The dotted line and dashed line in the upper plane are the voltage signals $U_L(t)$ and $U_R(t)$ respectively. The lower plane is the current response.

consider the Hamiltonian of the wire Eq. (3.1) in the real space,

$$\begin{aligned} H_0 &= \int dx \phi^\dagger \left[-\frac{\partial_x^2}{2m} - \mu - i(\alpha\tau_y + \beta\tau_x)\partial_x + V_z\tau_z \right] \phi, \\ H_\Delta &= \Delta \int dx (\psi_\uparrow\psi_\downarrow + \text{H.c.}), \end{aligned} \tag{3.35}$$

where $\phi = (\psi_\uparrow, \psi_\downarrow)^\text{T}$. We will use the bosonization method [20; 39; 52; 53; 96; 133] to discuss the interaction and disorder effects in the wire. Generally, in one dimension, the localization length due to the disorder is of the order of the mean free path. It means that after bumping a couple of times on the impurities the electrons are localized [52] and the wire becomes insulator. However, when the superconducting pairing satisfies the condition Eq. (3.3), the wire is in the topological superconducting phase. This competing mechanism can be quantitatively studied by the renormalization analysis of the density-density correlation function of the wire.

3.4.1 brief introduction of bosonization

3.4.1.1 left and right movers representation

To obtain the low-energy properties of the wire, we can deal with excitations close to the Fermi surface. Since the chemical potential μ lies within the gap, only the lower band in Eq. (3.4) is activated, and for one dimension, there are only two Fermi points $\pm k_F$ in the energy spectrum. We can linearize the dispersion relation near each Fermi points. In one dimension, because the low-energy particle-hole excitations have both well-defined momentum and energy, this will lead to two species of fermions: left and right moving fermions. We then replace the original model by the one where the energy spectrum is purely linear. This is nothing but assuming that the density of states is constant [52].

To begin with, we write the field operator of the Hamiltonian in the left and right movers representation. By the unitary transform $a_{ks} = \sum_\nu \langle s | \chi_\nu(k) \rangle a_{k\nu}$ where $s = \uparrow, \downarrow$ and $\nu = \pm$, we can transform the field operator $\psi_s(x)$ from the spin basis to the band basis,

$$\psi_s(x) = \frac{1}{\sqrt{2\pi}} \int dk e^{ikx} a_{ks} = \sum_\nu \frac{1}{\sqrt{2\pi}} \int dk e^{ikx} \langle s | \chi_\nu(k) \rangle a_{k\nu}. \tag{3.36}$$

Because only the electrons with momentum k near two Fermi points $\pm k_F$ of the lower

band in Eq. (3.4) are activated, we approximate the field operator as

$$\begin{aligned}
\psi_s(x) &\approx \frac{1}{\sqrt{2\pi}} \int_{-k_F-\Lambda}^{-k_F+\Lambda} dk e^{ikx} \langle s | \chi_-(k) \rangle a_{k,-} + \frac{1}{\sqrt{2\pi}} \int_{k_F-\Lambda}^{k_F+\Lambda} dk e^{ikx} \langle s | \chi_-(k) \rangle a_{k,-}, \\
&\approx e^{-ik_F x} \langle s | \chi_-(-k_F) \rangle \frac{1}{\sqrt{2\pi}} \int_{-k_F-\Lambda}^{-k_F+\Lambda} dk e^{i(k+k_F)x} a_{k,-} \\
&\quad + e^{ik_F x} \langle s | \chi_-(k_F) \rangle \frac{1}{\sqrt{2\pi}} \int_{k_F-\Lambda}^{k_F+\Lambda} dk e^{i(k-k_F)x} a_{k,-},
\end{aligned} \tag{3.37}$$

where $\Lambda \rightarrow 0$. Then we can express the field operator in terms of the left and right movers as

$$\psi_s(x) = e^{-ik_F x} \langle s | \chi_-(-k_F) \rangle \psi_L(x) + e^{ik_F x} \langle s | \chi_-(k_F) \rangle \psi_R(x), \tag{3.38}$$

where the left and right movers are

$$\begin{aligned}
\psi_L(x) &= \frac{1}{\sqrt{2\pi}} \int_{-\infty}^{\infty} dk e^{i(k+k_F)x} d_{k,L}, \\
\psi_R(x) &= \frac{1}{\sqrt{2\pi}} \int_{-\infty}^{\infty} dk e^{i(k-k_F)x} d_{k,R}.
\end{aligned} \tag{3.39}$$

Here $d_{k,L}$ and $d_{k,R}$ are the annihilation operators in the left and right branches of the lower band and we have extended the linear dispersion relation to the whole Brillouin zone by changing the range of integral for the left and right movers to $(-\infty, \infty)$.

We now turn to study the kinetic term H_0 in Eq. (3.5). By linearizing the energy spectrum $\varepsilon_-(k)$ near the two Fermi point $\pm k_F$, the low energy kinetic term becomes

$$\begin{aligned}
H_0 &\approx \int_{-\infty}^{\infty} dk [\varepsilon_F - \nu_F(k + k_F)] d_{k,L}^\dagger d_{k,L} + \int_{-\infty}^{\infty} dk [\varepsilon_F + \nu_F(k - k_F)] d_{k,R}^\dagger d_{k,R}, \\
&= \int_{-\infty}^{\infty} dk \nu_F(-k - k_F) d_{k,L}^\dagger d_{k,L} + \int_{-\infty}^{\infty} dk \nu_F(k - k_F) d_{k,R}^\dagger d_{k,R} + \text{constant},
\end{aligned} \tag{3.40}$$

where $\varepsilon_F = \frac{k_F^2}{2m} - \mu - \sqrt{(\alpha^2 + \beta^2)k_F^2 + V_z^2}$ and $\nu_F = \frac{k_F}{m} - \frac{(\alpha^2 + \beta^2)k_F}{\sqrt{(\alpha^2 + \beta^2)k_F^2 + V_z^2}}$. On the other

hand, by the definition of $\psi_R(x)$, we find that

$$\begin{aligned}
& \int dx \psi_R^\dagger(x) (-i\nu_F \partial_x) \psi_R(x) \\
&= \int dk dk' \left[\frac{1}{2\pi} \int dx e^{i(k'-k)x} \right] \nu_F (k' - k_F) d_{k,R}^\dagger d_{k',R}, \\
&= \int dk \nu_F (k - k_F) d_{k,R}^\dagger d_{k,R}.
\end{aligned} \tag{3.41}$$

Therefore, the low energy kinetic term is

$$H_0 = i\nu_F \int dx [\psi_L^\dagger(x) \partial_x \psi_L(x) - \psi_R^\dagger(x) \partial_x \psi_R(x)]. \tag{3.42}$$

Next we consider the s -wave superconducting term in Eq. (3.35). From Eq. (3.38), we have

$$\begin{aligned}
& \psi_\uparrow(x) \psi_\downarrow(x) \\
&= \left[e^{-ik_F x} (-e^{-i\theta/2} \sin \frac{\gamma_{-k_F}}{2}) \psi_L(x) + e^{ik_F x} (-e^{-i\theta/2} \sin \frac{\gamma_{k_F}}{2}) \psi_R(x) \right] \\
&\cdot \left[e^{-ik_F x} e^{i\theta/2} \cos \frac{\gamma_{-k_F}}{2} \psi_L(x) + e^{ik_F x} e^{i\theta/2} \cos \frac{\gamma_{k_F}}{2} \psi_R(x) \right], \\
&= -\sin \frac{\gamma_{-k_F}}{2} \cos \frac{\gamma_{k_F}}{2} \psi_L(x) \psi_R(x) - \sin \frac{\gamma_{k_F}}{2} \cos \frac{\gamma_{-k_F}}{2} \psi_R(x) \psi_L(x) \\
&- e^{-i2k_F x} \sin \frac{\gamma_{-k_F}}{2} \cos \frac{\gamma_{-k_F}}{2} \psi_L(x) \psi_L(x) - e^{i2k_F x} \sin \frac{\gamma_{k_F}}{2} \cos \frac{\gamma_{k_F}}{2} \psi_R(x) \psi_R(x).
\end{aligned} \tag{3.43}$$

Neglecting the oscillating terms and taking into account that $\gamma_{-k} = \arctan \frac{-\sqrt{\alpha^2 + \beta^2} k}{V_z} = -\gamma_k$, we find that

$$\psi_\uparrow(x) \psi_\downarrow(x) = \sin \gamma_{k_F} \psi_L(x) \psi_R(x). \tag{3.44}$$

Therefore, the s -wave superconducting term is

$$H_\Delta = \Delta \sin \gamma_{k_F} \int dx [\psi_L(x) \psi_R(x) + \psi_R^\dagger(x) \psi_L^\dagger(x)]. \tag{3.45}$$

We next consider the Coulomb interaction which can be formulated as

$$H_{\text{int}} = \int dx dx' V(x - x') \rho(x) \rho(x'), \tag{3.46}$$

where the electron density operator is $\rho(x) = \sum_{s=\uparrow,\downarrow} \psi_s^\dagger(x) \psi_s(x)$. In the momentum

space, the interaction can be recast into

$$H_{\text{int}} = \frac{1}{2\Omega} \sum_{k,s,k',s',q} \tilde{V}(q) a_{k+q,s}^\dagger a_{k'-q,s'}^\dagger a_{k',s'} a_{k,s}. \quad (3.47)$$

Similarly, we transform the Hamiltonian to the band basis (a_{k+}, a_{k-}) and neglect the upper-band operators, then the interaction term becomes

$$H_{\text{int}} = \frac{1}{2\Omega} \sum_{k,k',q} \tilde{V}(q) \cos \frac{\gamma_{k+q} - \gamma_k}{2} \cos \frac{\gamma_{k'-q} - \gamma_{k'}}{2} d_{k+q}^\dagger d_{k'-q}^\dagger d_{k'} d_k. \quad (3.48)$$

One should be reminded that the most efficient processes in the interaction are the ones that can act close to the Fermi surface. Particularly in one dimension, it is worth noting that the Fermi surface is reduced to two points $\pm k_F$ that allow us to decompose the interaction into three scattering processes. The first one is exchange scattering, where two electrons moving in the same direction collide and exchange their velocities; the second one is forward scattering, where two electrons moving in the opposite directions collide and keep moving in their original directions; the third one is the backward scattering, where two electrons moving in the opposite directions collide and move backward. Notice that the wave vector q for the forward and exchange processes is ~ 0 , and $\sim \pm 2k_F$ for the backward scattering. It is easy to see that the forward and backward scattering processes are identical for the spinless fermion as the particles are indiscernible. Therefore, the interaction Hamiltonian can be expressed as the sum of the above scattering processes:

$$H_{\text{int}} = \frac{\tilde{V}(0)}{2\Omega} \sum_{k \in R, k' \in R, q \sim 0} d_{k+q}^\dagger d_{k'-q}^\dagger d_{k'} d_k + \frac{\tilde{V}(0)}{\Omega} \sum_{k \in R, k' \in L, q \sim 0} d_{k+q}^\dagger d_{k'-q}^\dagger d_{k'} d_k + (R \leftrightarrow L). \quad (3.49)$$

Using the definitions of the left and right movers Eq. (3.39), the interaction can be written as

$$\begin{aligned} H_{\text{int}} &= g_2 \int dx \psi_R^\dagger(x) \psi_R(x) \psi_L^\dagger(x) \psi_L(x) \\ &+ \frac{g_4}{2} \int dx \psi_R^\dagger(x) \psi_R(x) \psi_R^\dagger(x) \psi_R(x) \\ &+ \frac{g_4}{2} \int dx \psi_L^\dagger(x) \psi_L(x) \psi_L^\dagger(x) \psi_L(x), \end{aligned} \quad (3.50)$$

where $g_2/2 = g_4 = \tilde{V}(0)$. Now we turn to study the disorder term. When the impurities

are weak and dense enough so that the effect of each impurity is negligible, they can only act collectively. In this case, there are many impurities in a volume small compared to the scale of variation of the physical quantities but large compared to the distance between impurities. Physically it means that one can replace the original disorder by a coarse grained version. This coarse grained disorder is equivalent to a Gaussian disorder [52] due to the central limit theorem. The disorder potential $U(x)$ can be treated as a random chemical potential on the impurity sites. Thus the disorder term can be formulated as

$$H_{\text{dis}} = \int dx U(x) \rho(x), \quad (3.51)$$

where the disorder potential satisfies Gaussian distribution

$$p(U) = \exp \left[-\frac{1}{2D} \int dx U^2(x) \right]. \quad (3.52)$$

Here we assume that the impurity potential is short-range so that $\langle U(x)U(x') \rangle = D\delta(x-x')$. Fourier transforming the Hamiltonian and projecting it onto the lower band, we have

$$H_{\text{dis}} = \frac{1}{\Omega} \sum_{k,q} \tilde{U}(q) \cos \frac{\gamma_{k+q} - \gamma_k}{2} d_{k+q}^\dagger d_k. \quad (3.53)$$

Again, the most important processes are the ones close to the Fermi surface. In one dimension, the disorder term can be thus approximated as

$$\begin{aligned} H_{\text{dis}} &= \frac{1}{\Omega} \sum_{q \sim 0} \tilde{U}(q) \sum_{k \sim \pm k_F} d_{k+q}^\dagger d_k \\ &+ \frac{\cos \gamma_{k_F}}{\Omega} \sum_{q \sim 2k_F} \tilde{U}(q) \sum_{k \sim -k_F} d_{k+q}^\dagger d_k \\ &+ \frac{\cos \gamma_{k_F}}{\Omega} \sum_{q \sim -2k_F} \tilde{U}(q) \sum_{k \sim k_F} d_{k+q}^\dagger d_k. \end{aligned} \quad (3.54)$$

In the left and right movers representation, we have

$$\begin{aligned} H_{\text{dis}} &= \int dx \eta(x) [\psi_R^\dagger(x) \psi_R(x) + \psi_L^\dagger(x) \psi_L(x)] \\ &+ \cos \gamma_{k_F} \int dx [\xi(x) \psi_L^\dagger(x) \psi_R(x) + \xi^*(x) \psi_R^\dagger(x) \psi_L(x)], \end{aligned} \quad (3.55)$$

where $\eta(x) = \frac{1}{\Omega} \sum_{q \sim 0} \tilde{U}(q) e^{iqx}$ and $\xi(x) = \frac{1}{\Omega} \sum_{q \sim 0} \tilde{U}(q - 2k_F) e^{iqx}$ are two independent

Gaussian random variables. Note that $\eta(x)$ is real and $\xi(x)$ is complex. The correlation relations are $\langle \eta(x)\eta(x') \rangle = \langle \xi(x)\xi^*(x') \rangle = D\delta(x-x')$, and zero otherwise.

3.4.1.2 bosonization of the Majorana nanowire

The Abelian bosonization formula [48; 52; 96; 97] is given by

$$\begin{aligned}\psi_L(x) &= \frac{1}{\sqrt{2\pi\alpha}} e^{-i\sqrt{4\pi}\phi_L(x)}, \\ \psi_R(x) &= \frac{1}{\sqrt{2\pi\alpha}} e^{i\sqrt{4\pi}\phi_R(x)},\end{aligned}\tag{3.56}$$

where $\psi_{L/R}(x)$ is the massless Dirac field (fermionic) as shown in Eq. (3.39), and $\phi_{L/R}(x)$ is massless Klein-Gordon field (bosonic). α is the short-range cutoff for the convergence of the continuum theory. Please see Appendix E for details.

Using the formula Eq. (3.56), the kinetic energy Eq. (3.42) can be bosonized as

$$H_0 = \pi\nu_F \int dx [\rho_L^2(x) + \rho_R^2(x)],\tag{3.57}$$

where $\rho_{L/R}(x) = \frac{1}{\sqrt{\pi}}\partial_x\phi_{L/R}(x)$ is the normal-ordered density operator for left/right mover. Please see Appendix F for the bosonization of the kinetic energy Eq. (3.57). We define two new variables, $\phi_L = \frac{-1}{\sqrt{4\pi}}(\theta + \varphi)$ and $\phi_R = \frac{1}{\sqrt{4\pi}}(\theta - \varphi)$, where the commutation relation is $[\theta(x), \varphi(y)] = i\pi\text{sgn}(y-x)/2$. The Hamiltonian H_0 then becomes

$$H_0 = \frac{\nu_F}{2\pi} \int dx [(\partial_x\theta)^2 + (\partial_x\varphi)^2].\tag{3.58}$$

For the s -wave superconducting term, substituting Eq. (3.56) into Eq. (3.45), after bosonization it can be written as

$$H_\Delta = \frac{\Delta \sin \gamma_{k_F}}{\pi\alpha} \int dx \cos 2\theta.\tag{3.59}$$

Similarly, the Coulomb interaction Eq. (3.50) in terms of the field θ and φ is

$$H_{\text{int}} = \frac{g_2}{4\pi^2} \int dx [(\partial_x\varphi)^2 - (\partial_x\theta)^2] + \frac{g_4}{4\pi^2} \int dx [(\partial_x\varphi)^2 + (\partial_x\theta)^2].\tag{3.60}$$

The bosonic form of the disorder term Eq. (3.55) is given by

$$H_{\text{dis}} = -\frac{1}{\pi} \int dx [\eta(x)\partial_x\varphi] + \frac{\cos \gamma_{k_F}}{2\pi\alpha} \int dx [\xi(x)e^{-i2\varphi} + \xi^*(x)e^{i2\varphi}].\tag{3.61}$$

Notice that in one dimension, the effect of Coulomb interaction just leads to the reparameterization of the kinetic energy H_0 . The interaction can be absorbed into the kinetic energy, then we arrive at the following Hamiltonian for the Luttinger liquid,

$$H_{\text{Lutt}} = H_0 + H_{\text{int}} = \frac{1}{2\pi} \int dx \left[uK(\partial_x\theta)^2 + \frac{u}{K}(\partial_x\varphi)^2 \right], \quad (3.62)$$

where the Luttinger parameters are

$$\begin{aligned} u &= \nu_F \left[(1 + y_4)^2 - y_2^2 \right]^{1/2}, \\ K &= \left(\frac{1 + y_4 - y_2}{1 + y_4 + y_2} \right)^{1/2}. \end{aligned} \quad (3.63)$$

Here $y_2 = \frac{g_2}{2\pi\nu_F}$ and $y_4 = \frac{g_4}{2\pi\nu_F}$. Furthermore, we observe that the first term in Eq. (3.61) is equivalent to a random gauge potential which can also be absorbed into the Hamiltonian of Luttinger liquid Eq. (3.62) via replacing $\varphi(x)$ by $\varphi(x) - \frac{K}{u} \int^x dy \eta(y)$. Finally, we achieve the bosonic Hamiltonian of the interacting wire with Gaussian disorder $H_{\text{dw}} = H_{\text{sG}} + H_{\text{bws}}$, where

$$\begin{aligned} H_{\text{sG}} &= \frac{1}{2\pi} \int dx \left[uK(\partial_x\theta)^2 + \frac{u}{K}(\partial_x\varphi)^2 \right] + \frac{\Delta \sin \gamma_{k_F}}{\pi\alpha} \int dx \cos 2\theta, \\ H_{\text{bws}} &= \frac{\cos \gamma_{k_F}}{2\pi\alpha} \int dx [\xi(x)e^{-i2\varphi} + \xi^*(x)e^{i2\varphi}]. \end{aligned} \quad (3.64)$$

The Hamiltonian H_{sG} is the well-known sine-Gordon Hamiltonian which has Kosterlitz-Thouless phase transition [84]. The superconducting term favors a superconducting ground state, however, the disorder term tends to pin the charge density to the disorder potential and favors an insulator phase [97]. Therefore, we can expect the disorder system undergoes a topological phase transition as the interplay of superconductivity and disorder.

3.4.2 influence on the Majorana transport

In general, we can use the perturbation theory to calculate the correlation function, for instance,

$$R(r_1 - r_2) = \langle e^{ia\sqrt{2}\varphi(r_1)} e^{-ia\sqrt{2}\varphi(r_2)} \rangle_{H_{\text{dw}}}, \quad (3.65)$$

to study the physical property of the interacting disorder wire [52]. The average for a system with a disorder potential U can be treated by the replica method as follows,

$$\langle O(\varphi) \rangle_{H_{\text{dw}}} = \lim_{n \rightarrow 0} \frac{\int \mathcal{D}[\xi, \xi^*] p(\xi, \xi^*) \int \prod_{i=1}^n \mathcal{D}\varphi_i O(\varphi_1) e^{-\sum_{a=1}^n S_U(\theta_a, \varphi_a)}}{\int \mathcal{D}[\xi, \xi^*] p(\xi, \xi^*)}, \quad (3.66)$$

where $O(\varphi)$ is some observable of φ . Please see Appendix G for details. Basically, we need to perform the functional integral over the n -copies of replicas φ_i and the Gaussian distributed random variables ξ and ξ^* . The Gaussian distributed disorder potential is $p(\xi, \xi^*) = e^{-\frac{1}{D} \int dx \xi(x) \xi^*(x)}$ and the action of the disorder system can be achieved by the Legendre transformation of the Hamiltonian H_{dw} ,

$$S_U(\theta_a, \varphi_a) = - \int_0^\beta d\tau \int dx \frac{i}{\pi} \partial_x \theta \partial_\tau \varphi + \int_0^\beta d\tau H_{\text{dw}}. \quad (3.67)$$

By integrating out the Gaussian random variables ξ and ξ^* , we arrive at

$$\langle O(\varphi) \rangle_{H_{\text{dw}}} = \lim_{n \rightarrow 0} \int \prod_{i=1}^n \mathcal{D}\varphi_i O(\varphi_1) e^{-S_{\text{eff}}}, \quad (3.68)$$

where

$$S_{\text{eff}} = \sum_{a=1}^n [S_0(\varphi_a) + S_\Delta(\varphi_a)] - \frac{D \cos^2 \gamma_{k_F}}{(2\pi\alpha)^2} \sum_{a,b=1}^n \int dx d\tau d\tau' \cos[2\varphi_a(x, \tau) - 2\varphi_b(x, \tau')]. \quad (3.69)$$

Here $S_0 = - \int_0^\beta d\tau \int dx \frac{i}{\pi} \partial_x \theta \partial_\tau \varphi + \int_0^\beta d\tau H_{\text{Lutt}}$ and $S_\Delta = \int_0^\beta d\tau H_\Delta$. The details of calculation of correlation function Eq. (3.65) by the replica method Eq. (3.68) is given in Appendix H. After some calculations, we find that the perturbation result is plagued by divergence which is notorious in one dimension. However, although the correlation is infinite, it should be independent of the change of short-range cutoff α because it characterizes the physical properties of the system. This peculiar property suggests the use of the renormalization group method [52; 97]. Particularly, by expanding the superconducting and disorder actions to the first leading order, changing the short-range cutoff $\alpha \rightarrow \alpha e^l$ and keeping the correlation function unchanged (see Appendix H for details),

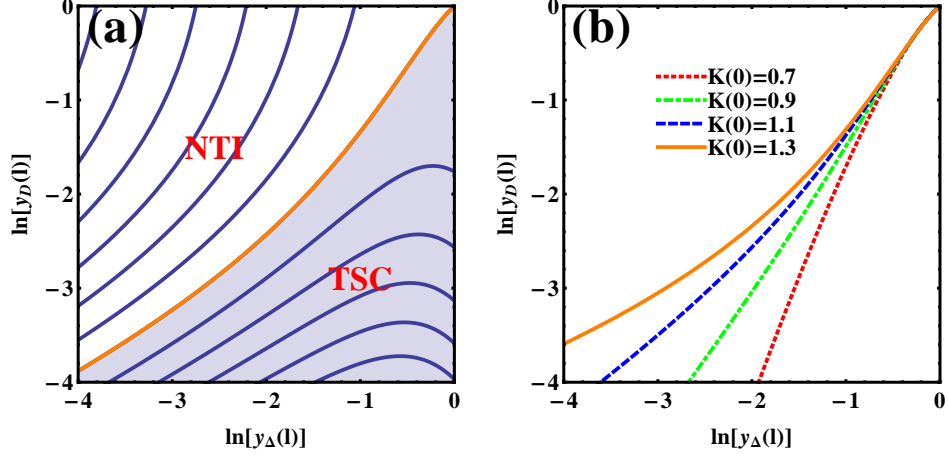


Figure 3.5: (a) RG flows of $y_D(l)$ and $y_\Delta(l)$, where $K(0) = 1.2$. NTI and TSC are short for non-topological insulator and topological superconductor. The orange line is the phase boundary. (b) phase boundaries with different $K(0)$ s.

we obtain the RG flows as follows,

$$\begin{aligned}
dK/dl &= y_\Delta^2 - y_D K^2, \\
dy_\Delta/dl &= (2 - K^{-1})y_\Delta, \\
dy_D/dl &= 2K y_D^2 - (2K - 3 + 2K^{-1}y_\Delta^2)y_D, \\
du/dl &= -y_D K u,
\end{aligned} \tag{3.70}$$

where $y_\Delta = \alpha\Delta \sin \gamma_{k_F}/u$ and $y_D = \alpha D \cos^2 \gamma_{k_F}/\pi u^2$. From the flows of $y_\Delta(l)$ and $y_D(l)$, we can see that when $K(l) < 1/2$, $y_D(l)$ is relevant, the system is in the random-pinned change density wave phase; when $K(l) > 3/2$, $y_\Delta(l)$ is relevant, the system is in the superconducting phase. When $1/2 < K(l) < 3/2$, both $y_D(l)$ and $y_\Delta(l)$ are relevant. In order to be consistent with the perturbation condition, the flows can be chosen to stop at l^* when $\max[y_D(l^*), y_\Delta(l^*)] = 1$. Using this criterion, the phase diagram in this $K(l)$ interval is obtained as shown in Fig. 3.5(a). Only when the parameters are in the shadow region, the Majorana fermions remain. In Fig. 3.5(b), we plot the phase boundaries with respect to different initial $K(0)$ and find that the topological superconducting phase becomes larger as $K(0)$ increases. Therefore, when $K(l) < 1/2$ or when $1/2 < K(l) < 3/2$ as well as the parameters are in the shadow region of Fig. 3.5(a), y_Δ is relevant and the Majorana transport is preserved, otherwise the disorder strength D will destroy the transport.

Part II

Mott-superfluid transition in hybrid circuit-QED system

Chapter 4

Phase transition of light in circuit-QED lattices coupled to nitrogen-vacancy centers in diamond

4.1 Introduction

The microscopic properties of strongly correlated many-particle systems emerging in solid-state physics are in general very hard to access experimentally [56; 60; 61]. So a method to simulate the properties of condensed-matter models using non-traditional controllable systems is highly desirable. Recently, the investigation of quantum simulation in photon-based many-body physics has received much attention in different systems [41; 56; 60; 61; 82; 136; 137]. Especially, there has been great interest in mimicking the quantum phase transition (QPT) of light by a scalable coupled resonator array in the context of cavity/circuit quantum electrodynamics (QED) [22; 50; 65; 73; 93; 124; 160; 167], which provides a convenient controllable platform for studying the strongly correlated states of light via photonic processes. On the other hand, artificially engineered hybrid devices can permit measurement access with good experimental control [38; 94]; and it is intriguing to employ a highly controllable quantum system with a tunable Hamiltonian to simulate the physics of another system of interest. This paradigm has promoted many experimental/theoretical proposals on probing the light phase and opened various possibilities for the simulation of many-body physics.

In this chapter, we elaborate an optical system for engineering the strongly correlated effects of light in a hybrid solid-state system. We consider a two-dimensional (2D) square

lattice of coupled transmission line resonators (TLRs) [10; 25; 140], where each TLR is coupled to a single nitrogen vacancy (NV) [21; 35; 47; 68; 174] encircled by a persistent current qubit (PCQ). We show that the competition between the on-site TLR-PCQ interaction and the nonlocal hopping induces the photonic localization-delocalization transition. Subsequently the Mott insulator (MI) phase and the superfluid (SF) phase can appear in a controllable way. The phase boundary in the case of photon hopping with real/complex-valued amplitudes can be obtained using the mean-field approach. Also, the quantum jump technique is employed to describe the phase diagram when the dissipation is considered. Finally, the possibility of observation of the QPT is discussed.

In our architecture, one can tune independently the on-site TLR-PCQ interaction and the nonlocal photonic hopping between adjacent TLRs. This permits us to systematically study the localization-delocalization transition of light in a complete parameter space. The main motivation for building such a hybrid system is to combine several advantages: *in situ* tunability of circuit elements [15; 112; 168], transmission measurement for state readout [10], peculiar characteristics of NVs (e.g., individual addressing [15; 87] and long coherence time at room-temperature [2; 72; 115]), and scalability of TLR arrays [34; 55; 65; 81; 103; 114; 118]. Due to the easy readout of the states of NV by laser or microwave, it is possible to indirectly probe the quantum many body states of our hybrid system by NV center. Recently, Underwood *et al* experimentally fabricated 25 arrays of TLRs and demonstrated the feasibility of quantum simulation in a circuit-QED system [153]. Lucero *et al* experimentally fabricated a complex circuit composed of four phase qubits and five TLRs to realize intricate quantum algorithms [98]. The progress renders the TLR lattice as a good platform for studying condensed-matter physics with photons and makes our scheme more practical.

The main results of this chapter were published in the following paper:

- Jia-Bin You, W. L. Yang, Zhen-Yu Xu, A. H. Chan, and C. H. Oh, *Phase transition of light in circuit-QED lattices coupled to nitrogen-vacancy centers in diamond*. Physical Review B **90**, 195112 (2014).

4.2 Model

As illustrated in Fig. 4.1, we consider a 2D lattice of coupled TLRs, where the basic unit consists of a TLR coupled to a single NV encircled by a PCQ, which acts as an interconnect to greatly magnify the NV-TLR coupling by several orders of magnitude,

compared with the direct NV-TLR coupling (far below the linewidth of TLR by dozens of KHz) resulting from the vacuum fluctuations of the photons [1; 152].

The TLR is made of a superconductor line interrupted by two capacitors at its ends. In the microwave domain, it can be treated as a quantum LC harmonic oscillator,

$$H^{\text{TLR}} = \omega_r(a^\dagger a + 1/2), \quad (4.1)$$

where a (a^\dagger) is the annihilation (creation) operator of the photonic mode in the TLR, and $\omega_r = \sqrt{1/L_r C_r}$ is the corresponding eigenfrequency with inductance L_r and capacitance C_r . Here we set $\hbar = 1$. The PCQ located at an antinode of the TLR's magnetic field is formed by a superconducting loop interrupted by three Josephson junctions, where all the junctions are identical except that one is smaller than the other two as shown in Fig. 4.1 [120; 152]. When the loop is biased by half a magnetic flux quantum, the device is an effective two-level qubit made up of two countercirculating persistent currents. This effective two-level system is described by the Hamiltonian $H^{\text{PCQ}} = \frac{1}{2}(\varepsilon\sigma_z + \Delta_0\sigma_x)$, where σ_x and σ_z are the Pauli matrices. Here $\varepsilon = 2I_p(\Phi - \Phi_0/2)$, where I_p is the persistent circulating current of the PCQ loop, Φ is the external magnetic flux through the loop induced by the current in the central conductor of the TLR and Φ_0 is the flux quantum; Δ_0 is the coupling between the two states of the two-level PCQ system [152]. Going to the eigenbasis we can write this two-level system as

$$H^{\text{PCQ}} = \frac{\omega_0}{2}\sigma_z, \quad (4.2)$$

where $\omega_0 = \sqrt{\varepsilon^2 + \Delta_0^2}$. The NV can be modeled as a three-level system in the triplet ground-state subspace consisting of $|^3A, m_s = 0\rangle$ and $|^3A, m_s = \pm 1\rangle$. The Hamiltonian is

$$H^{\text{NV}} = \gamma_e B_z S_z + D(S_z^2 - 2/3), \quad (4.3)$$

where γ_e is the electronic gyromagnetic ratio, $D/2\pi \sim 2.87$ GHz is the zero-field splitting which is predominantly due to dipolar spin-spin coupling between the two unpaired electrons forming the NV center, B_z is a perpendicular magnetic field at the NV center induced by the persistent circulating current and $S_z = \text{diag}\{1, 0, -1\}$ is the spin-1- z operator.

The PCQ magnetically couples to the TLR via mutual inductance, $H^{\text{T-P}} = -\mu \cdot B$, where μ is the magnetic dipole of PCQ induced by the persistent circulating currents and

B is the magnetic field at the PCQ induced by the current in the central conductor of the TLR. To quantize the Hamiltonian, the magnetic field is taken to consist of a single bosonic mode with the field operator $B \sim a^\dagger + a$ and the PCQ is coupled to the field through its magnetic dipole $\mu \sim \sigma^+ + \sigma^-$, where $\sigma^\pm = \frac{1}{2}(\sigma_x \pm i\sigma_y)$. Moving the TLR-PCQ coupling to interaction picture, we have $H^{\text{T-P}} \sim e^{i(\omega_r + \omega_0)t} a^\dagger \sigma^+ + e^{-i(\omega_r + \omega_0)t} a \sigma^- + e^{i(\omega_r - \omega_0)t} a^\dagger \sigma^- + e^{-i(\omega_r - \omega_0)t} a \sigma^+$. When $\omega_r \sim \omega_0$, the counter-rotating terms $a^\dagger \sigma^+$ and $a \sigma^-$ can be safely ignored by means of the rotating wave approximation. Therefore, we arrive at the famous Jaynes-Cummings (JC) type interaction

$$H^{\text{T-P}} = g(a^\dagger \sigma^- + a \sigma^+), \quad (4.4)$$

where $g = (I_p \mu_0 r^2 / d) \sqrt{\omega_r / 2L_r}$. Here r is the radius of the PCQ loop, d is the distance between the PCQ and central conductor of the TLR, and μ_0 is Bohr magneton. The changes of magnetic flux within the loop induced by I_p presented in the PCQ lead to small shifts in the transition frequencies ($m_s \rightarrow \pm 1$) of the NV [120; 152]. Through this small change in magnetic field the PCQ can couple to the NV via the Zeeman term,

$$H^{\text{N-P}} = \frac{1}{2} \eta \sigma_z S_z, \quad (4.5)$$

where the coupling is $\eta = I_p \mu_0 \gamma_e / r$.

Therefore, the basic unit of our system at site p is thus governed by the Hamiltonian $H_p^0 = H^{\text{TLR}} + H^{\text{PCQ}} + H^{\text{NV}} + H^{\text{T-P}} + H^{\text{N-P}}$. To get the eigenstates of the Hamiltonian H_p^0 , we note that $[H_p^0, S_z] = 0$, thus S_z can be replaced by its eigenvalue m_s . We then consider a sector of the Hamiltonian labeling by m_s ,

$$H_p^0(m_s) = \omega_r(a^\dagger a + 1/2) + (\omega_0 + \eta m_s) \sigma_z / 2 + g(a^\dagger \sigma^- + a \sigma^+) + \chi(m_s), \quad (4.6)$$

where $S_z |m_s\rangle = m_s |m_s\rangle$ and $\chi(m_s) = \gamma_e B_z m_s + D(m_s^2 - 2/3)$ is the eigenenergy of H^{NV} . Furthermore, the Hamiltonian can be written as a sum of two commuting parts, $H_p^0(m_s) - \chi(m_s) = H_I + H_{II}$, where

$$\begin{aligned} H_I &= \omega_r(a^\dagger a + 1/2 + \sigma_z/2), \\ H_{II} &= (-\Delta + \eta m_s) \sigma_z / 2 + g(a^\dagger \sigma^- + a \sigma^+). \end{aligned} \quad (4.7)$$

Here the detuning between the TLR and the PCQ is $\Delta = \omega_r - \omega_0$. The eigenstates of

H_I , being of tensor product form, can be easily solved and denoted by

$$\begin{aligned} |n, g\rangle &= \frac{(a^\dagger)^n}{\sqrt{n!}}|0\rangle \otimes \begin{bmatrix} 0 \\ 1 \end{bmatrix}, \\ |n, e\rangle &= \frac{(a^\dagger)^n}{\sqrt{n!}}|0\rangle \otimes \begin{bmatrix} 1 \\ 0 \end{bmatrix}, \end{aligned} \quad (4.8)$$

where n is the number of microwave photons in a single TLR, $|g\rangle$ and $|e\rangle$ are the ground and excited states of the two-level PCQ system. Via this observation and taking H_{II} into account, it is enough to diagonalize the Hamiltonian $H_p^0(m_s)$ in the subspaces spanned by $\{|n, e\rangle, |n+1, g\rangle\}$. The Hamiltonian projected into this subspaces is

$$h_p^0(m_s) = \begin{bmatrix} \langle n, e | H_p^0(m_s) | n, e \rangle & \langle n, e | H_p^0(m_s) | n+1, g \rangle \\ \langle n+1, g | H_p^0(m_s) | n, e \rangle & \langle n+1, g | H_p^0(m_s) | n+1, g \rangle \end{bmatrix}. \quad (4.9)$$

Since

$$\begin{aligned} H_p^0(m_s)|n, e\rangle &= [(n+1/2)\omega_r + (\omega_0 + \eta m_s)/2 + \chi(m_s)]|n, e\rangle + g\sqrt{n+1}|n+1, g\rangle, \\ H_p^0(m_s)|n+1, g\rangle &= [(n+3/2)\omega_r - (\omega_0 + \eta m_s)/2 + \chi(m_s)]|n+1, g\rangle + g\sqrt{n+1}|n, e\rangle, \end{aligned} \quad (4.10)$$

the Hamiltonian $h_p^0(m_s)$ can be explicitly written as

$$\begin{bmatrix} (n+1/2)\omega_r + (\omega_0 + \eta m_s)/2 + \chi(m_s) & g\sqrt{n+1} \\ g\sqrt{n+1} & (n+3/2)\omega_r - (\omega_0 + \eta m_s)/2 + \chi(m_s) \end{bmatrix}. \quad (4.11)$$

Therefore, diagonalizing the Hamiltonian Eq. (4.11) via the eigenequation $|E\mathbf{I} - h_p^0(m_s)| = 0$, where E is the eigenenergy and \mathbf{I} is the identical matrix, the photon-dependent eigenenergies can be obtained,

$$E_{\pm}(n) = (n+1)\omega_r \pm \Omega_n(\Delta)/2 + \chi(m_s), \quad (4.12)$$

where the Rabi frequency is $\Omega_n(\Delta) = \sqrt{4g^2(n+1) + (\Delta - \eta m_s)^2}$. The corresponding

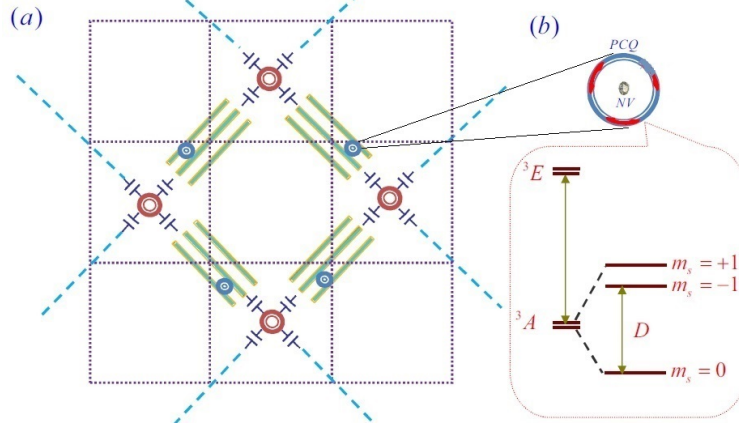


Figure 4.1: (a) Schematic circuit for the resonator lattice, where each TLR is coupled to a single NV center encircled by a PCQ, and the red circles denote the central coupler. (b) The subsystem consisting of NV and PCQ, where NV is at the center of the loop. The PCQ is made up of three Josephson junctions, and it couples to the NV via the magnetic field at the center of the loop generated by the persistent currents in the loop. The energy levels of NV are shown in the red box.

eigenstates are

$$\begin{aligned}
 |n, +\rangle &= \sin \frac{\beta_n}{2} |n, e\rangle + \cos \frac{\beta_n}{2} |n+1, g\rangle, \\
 |n, -\rangle &= -\cos \frac{\beta_n}{2} |n, e\rangle + \sin \frac{\beta_n}{2} |n+1, g\rangle,
 \end{aligned} \tag{4.13}$$

where $\tan \beta_n = \frac{2g\sqrt{n+1}}{\Delta - \eta m_s}$. Therefore, the eigenstates of the whole Hamiltonian H_p^0 , $|m_s, n, \pm\rangle = |m_s\rangle \otimes |n, \pm\rangle$, which consist of a microwave photon at TLR, an excitation mode from PCQ and an excitation mode from NV are called dressed states (polariton). The unperturbed TLR eigenstates $|n\rangle$ are modified (dressed) by the interaction with the PCQ and the NV, and their eigenfrequencies are shifted by the Rabi frequency.

We present a paradigm for a 2D TLR lattice coupled to the solid-state spins of the NV centers. We have shown that a specially engineered resonator lattice provides a practical platform to couple both individual spin and superconducting qubit, and engineer their interactions in a controllable way.

4.3 Mott-superfluid transition

We study the full Hamiltonian of the 2D square lattice by adding the on-site chemical potential and the nonlocal microwave photonic tunneling between adjacent sites. Here the photonic tunneling in our model can be realized by a central coupler which serves as an individual tunable quantum transducer to transfer photonic states between adjacent TLRs. Here, the central coupler may be conceived as a Josephson ring circuit [55; 81; 118], or a current-biased Josephson junction phase qubit [11; 105; 171; 172], or a capacitive coupling element [67], or an active nonreciprocal device as proposed in Ref. [75]. The Hamiltonian is given by

$$H = \sum_p H_p^0 + \sum_{\langle p,q \rangle} k_{\langle p,q \rangle} a_p^\dagger a_q - \sum_p \mu_p N_p, \quad (4.14)$$

where μ_p is the chemical potential at site p , a_p (a_p^\dagger) is the annihilation (creation) operator of the photonic mode in the TLR at site p , and $k_{\langle p,q \rangle} = 2Z_0 C_{\langle p,q \rangle} (\omega_r + \delta_p)(\omega_r + \delta_q)$ are photonic tunneling rates between two adjacent resonators p and q denoted by $\langle p, q \rangle$, which are set by the tunable mutual capacitance $C_{\langle p,q \rangle}$ between resonator ends with characteristic impedance Z_0 and frequency shift δ_p due to random disorder [153]. Since $\omega_r \gg \delta_p$, one can assume that $k_{\langle p,q \rangle} = k = 2Z_0 C \omega_r^2$ without disorder for nearest-neighbor resonators, and $k_{\langle p,q \rangle} = 0$ for other resonator pairs. Here we have tuned the mutual capacitance $C_{\langle p,q \rangle} = C$ for all the photonic tunneling between two adjacent TLRs. The conserved quantity in our system is the total number of polaritons $N = \sum_p (a_p^\dagger a_p + \sigma_p^+ \sigma_p^- + \frac{1}{2} S_p^+ S_p^-)$ with S^i (σ^i) the spin-1 (-1/2) operators ($i = \pm$). Thus we can define the chemical potential μ_p for polaritons at site p .

The photon-dependent eigenstates of the Hamiltonian H_p^0 are dressed states $|m_s, \pm, n\rangle$ with the eigenenergies Eq. (4.12). The interaction of this hybrid system H_p^0 is governed by the JC-type of coupling Eq. (4.4), which enables the interconversion of qubit excitations and photons, and provides the effective on-site repulsion. This effective on-site repulsion can be defined as the energy cost of adding an additional polariton into a lattice site [56]. Here we study the zero-temperature property of the Hamiltonian, thus only the lower energy band of Eq. (4.12) is considered. Therefore, the on-site repulsion is given by $U(n) = |E_{|m_s, -, n+1\rangle} - E_{|m_s, -, n\rangle} - \omega_r|$. Meanwhile, the microwave photon in the TLR can tunnel from one TLR to its neighboring TLRs. This competition between the effective on-site repulsion and the nearest neighbor photon hopping will lead to the Mott-superfluid transition. The difference between the Bose-Hubbard model [85] and our model is that

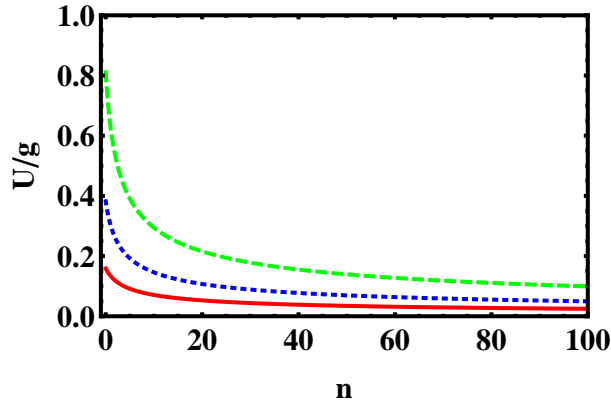


Figure 4.2: The dependence of effective on-site repulsion U on the photon number n . The parameters are $\Delta = 1$, $m_s = 0$, and $g = 0.5$ (red solid), 1 (blue dotted), 2 (green dashed).

the conserved particles in our model are the polaritons rather than the pure bosons in the Bose-Hubbard model, and the effective on-site repulsion decreases with the growth of photon number [56] and goes to zero in the limit of large n as shown in Fig. 4.2, while it is a constant in the Bose-Hubbard model.

The phase can be distinguished using the corresponding order parameters. Here we choose the SF order parameter $\psi = \langle a_p \rangle$ (set to be real) to differentiate the Mott-insulator state from the SF state. Using the mean-field theory [155; 156], we decouple the hopping term as $a_p^\dagger a_q = \langle a_p^\dagger \rangle a_q + a_p^\dagger \langle a_q \rangle - \langle a_p^\dagger \rangle \langle a_q \rangle$; the resulting mean-field Hamiltonian can then be written as a sum over single sites,

$$H^{\text{MF}} = \sum_p [H_p^0 - zk\psi(a_p^\dagger + a_p) + zk\psi^2 - \mu N_p], \quad (4.15)$$

where $z = 4$ is the number of nearest neighbors. Here we have assumed that the chemical potentials at all sites are equal, $\mu_p = \mu$. Similarly, $[H^{\text{MF}}, S_z] = 0$, therefore, S_z can be treated as a c -number in the mean-field Hamiltonian and has three eigenvalues $m_s = \pm 1, 0$. We then replace the operator S_z by its eigenvalue m_s and consider a sector of the mean-field Hamiltonian $H^{\text{MF}}(m_s)$. To fix the order parameter ψ in the mean-field Hamiltonian, the variational method is employed [56]. We study the zero-temperature phase diagram of the Hamiltonian $H^{\text{MF}}(m_s)$, thus only the ground state is necessary to be taken into account. First, we write the mean-field Hamiltonian in the polariton basis,

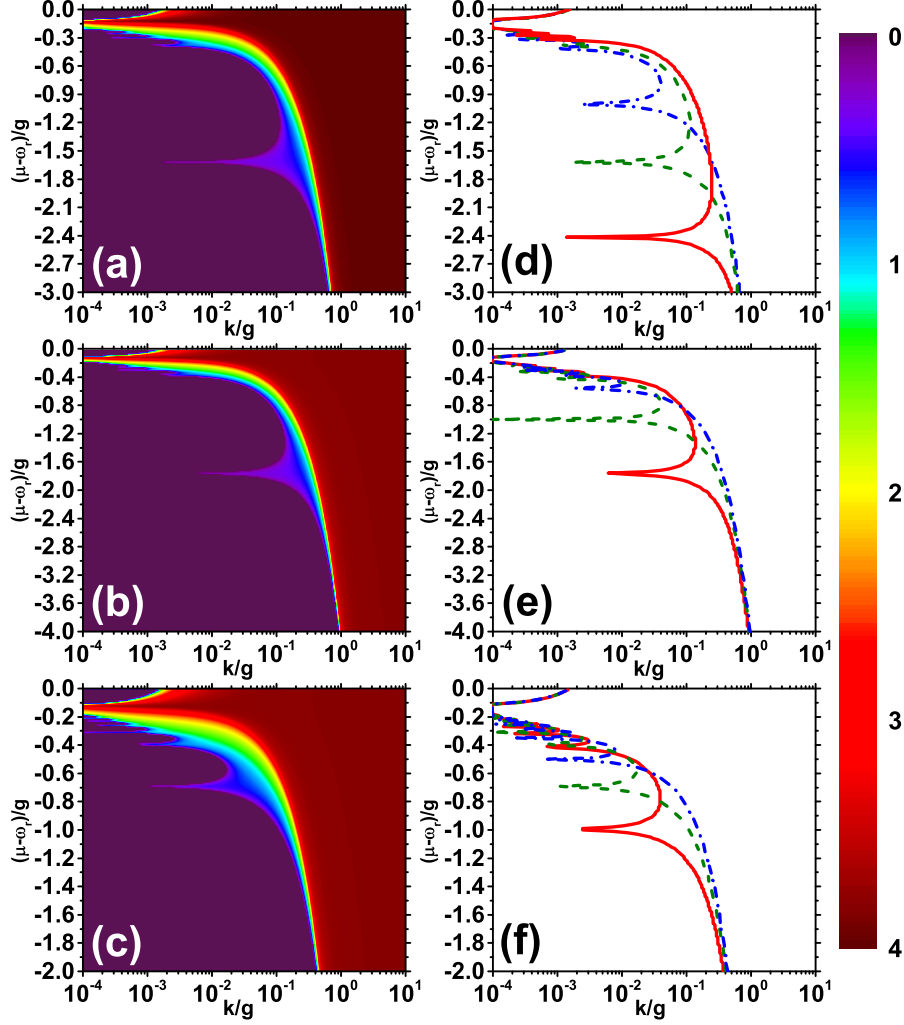


Figure 4.3: The phase diagrams in the $\mu \sim k$ plane for different sets of NV-PCQ coupling η and tunable magnetic fields B_z applied on a NV, where μ and k are the chemical potential and the photon hopping rate. The common parameters are $g = 1$, $\omega_r = 200$, $D = 100$, and $\gamma_e = -10^3$. The other parameters are set as follows: (a) $\eta = 0.01$, $B_z = 0.0005\text{T}$, and $\Delta = g$; the phase boundaries are plotted in (d), where $\Delta = 2g$ (solid), g (dashed), and 0 (dot-dashed). (b) $\eta = 1.2$, $B_z = -0.3\text{T}$, and $\Delta = 0$; the phase boundaries are plotted in (e), where $B_z = -0.3\text{T}$ (solid), 0.0005T (dashed), and 0.3T (dot-dashed). (c) $\eta = 0.75$, $B_z = 0.3\text{T}$, and $\Delta = 0$; the phase boundaries are plotted in (f), where $\eta = 0.01$ (solid), $\eta = 0.75$ (dashed), and $\eta = 1.5$ (dot-dashed).

$\{|g, 0\rangle, |e, 0\rangle, |g, 1\rangle, |e, 1\rangle, |g, 2\rangle, |e, 2\rangle, \dots\}$. In this basis, $H^{MF}(m_s)$ reads

$$\begin{aligned}
& \begin{bmatrix}
-\frac{\omega_0}{2} - \frac{\eta m_s}{2} & 0 & -zk\psi & 0 & 0 & 0 \\
0 & \frac{\omega_0}{2} + \frac{\eta m_s}{2} - \mu & g & -zk\psi & 0 & 0 \\
-zk\psi & g & \omega_r - \frac{\omega_0}{2} - \frac{\eta m_s}{2} - \mu & 0 & -\sqrt{2}zk\psi & 0 \\
0 & -zk\psi & 0 & \omega_r + \frac{\omega_0}{2} + \frac{\eta m_s}{2} - 2\mu & \sqrt{2}g & -\sqrt{2}zk\psi \\
0 & 0 & -\sqrt{2}zk\psi & \sqrt{2}g & 2\omega_r - \frac{\omega_0}{2} - \frac{\eta m_s}{2} - 2\mu & 0 & \dots \\
0 & 0 & 0 & -\sqrt{2}zk\psi & 0 & 2\omega_r + \frac{\omega_0}{2} + \frac{\eta m_s}{2} - 3\mu & \dots \\
& & & & \dots & \dots & \dots
\end{bmatrix} \\
& + \left[\frac{\omega_r}{2} + \gamma_e B_z m_s + D(m_s^2 - \frac{2}{3}) + zk\psi^2 - \mu(1 + \frac{m_s}{2} - \frac{m_s^2}{2}) \right] \mathbf{I}.
\end{aligned} \tag{4.16}$$

We then truncate $H^{MF}(m_s)$ at a finite value of n photon states, n_{\max} . Second, numerically diagonalize this Hamiltonian in the truncated basis and identify the ground state energy, E_g . Third, increase n_{\max} until E_g converges to its value at $n_{\max} = \infty$. Finally, minimize E_g with respect to ψ for different values of μ and k . The order parameter can then be fixed by $\{\psi(\mu, k) : \partial E_g(\mu, k)/\partial \psi = 0\}$. We plot ψ in the (μ, k) plane to obtain the mean-field phase diagram/boundary when η varies from the weak coupling regime ($\eta \ll g$) to the strong coupling regime ($\eta > g$) under the resonant/detuning case. The features of Fig. 4.3 are rich. The regime where $\psi = 0$ corresponds to the stable and incompressible MI lobes characterized by a fixed number of excitations per site with no variance. In each MI lobe, due to the nonlinearity and anharmonicity in the spectrum originating from the photon blockade effect [9; 64; 89], the strong TLR-PCQ interaction leads to an effective large polariton-polariton repulsion which freezes out hopping and localizes polaritons at individual lattice sites. By contrast, strong hopping favors delocalization and leads to a condensation of the particles into the zero-momentum state; namely, $\psi \neq 0$ indicates a SF compressible phase with the stable ground state at each site corresponding to a coherent state of excitations. The compressibility is defined as the changeability of the average number of polaritons per site in the grand canonical ensemble, $\rho = -\partial E_g(\psi = \psi_{\min})/\partial \mu$. When $\partial \rho/\partial \mu = 0$, the system has constant density and is incompressible; otherwise the system is compressible [56].

Analogous to the Bose-Hubbard model, the underlying physical picture is that the MI-SF phase transition results from the interplay between polariton delocalization and on-site repulsive interaction. Therefore, the phase boundary primarily depends on the ratio of the photon-hopping k to the on-site repulsion. When the on-site repulsion dominates over hopping, the system is in the MI phase, otherwise the system is in the SF phase. From the expressions of the parameter η and g , we can find that reduction of the size of the PCQ loop will increase η but decrease g , and the adjustment of the distance d

only affects the TLR-PCQ interaction. Furthermore, the detuning Δ is also tunable by varying the magnetic field applied on the NV. In Fig. 4.3, one can find that the size of the MI lobes varies with Δ .

Further insight into the transition can be gained when the photonic hopping with complex-valued amplitude exists in Eq. (4.14), where the hopping process becomes $-\sum_{\langle p,q \rangle} k_{\langle p,q \rangle} e^{i\phi_{\langle p,q \rangle}} a_p^\dagger a_q$ with tunneling phase $\phi_{\langle p,q \rangle} = -\phi_{\langle q,p \rangle}$ and we set $k_{\langle p,q \rangle} = k$. We emphasize that this process is possible if the intermediate coupling elements break time-reversal symmetry [55; 65; 81; 118; 121]. It can be realized by the passive coupling elements. By the meaning of passive, the coupler only transfers photons via intermediate virtual excitations and otherwise remains in its ground state at all times. Consequently, the coupler degrees of freedom can be integrated out so that the effective hopping for the passive coupling elements becomes complex. The complex tunneling amplitude $k_{\langle p,q \rangle} e^{i\phi_{\langle p,q \rangle}}$ provides a new perspective in the dynamical evolution of the system. Consider the case where the tunneling phases inside each row/column of the TLR lattice in Fig. 4.1 are equal, and the phases in all the rows/columns are in an alternate pattern of $\{2\pi\alpha, -2\pi\alpha, 2\pi\alpha, -2\pi\alpha, \dots\}$, then in the mean-field approximation, the hopping term becomes

$$\begin{aligned} -\sum_{\langle p,q \rangle} k_{\langle p,q \rangle} e^{i\phi_{\langle p,q \rangle}} a_p^\dagger a_q &= -\sum_{\langle p,q \rangle} k e^{i\phi_{\langle p,q \rangle}} a_p^\dagger a_q, \\ &= -k \sum_p (e^{i2\pi\alpha} a_{p+\hat{x}}^\dagger a_p + e^{i2\pi\alpha} a_{p+\hat{y}}^\dagger a_p + \text{H.c.}), \\ &= \sum_p [-zk\psi \cos(2\pi\alpha)(a_p^\dagger + a_p) + zk\psi^2 \cos(2\pi\alpha)], \end{aligned} \quad (4.17)$$

where \hat{x} (\hat{y}) is the unit vector in the x (y) direction. Here we have applied the mean-field approximation in the third line of Eq. (4.17). Therefore, the total Hamiltonian under the mean-field approximation reads

$$H_\alpha^{\text{MF}} = \sum_p [H_p^0 - zk\psi \cos(2\pi\alpha)(a_p^\dagger + a_p) + zk\psi^2 \cos(2\pi\alpha) - \mu N_p]. \quad (4.18)$$

The phase diagram is exhibited in Fig. 4.4; we find that the boundary line gradually shifts to the right as α increases in the interval $[0, 1/4]$. Because of the spatial variation of the tunneling phase, the wave function of a polariton from one lattice site to another acquires a nontrivial phase, which actually reduces the effective hopping rates from k to $k \cos(2\pi\alpha)$.

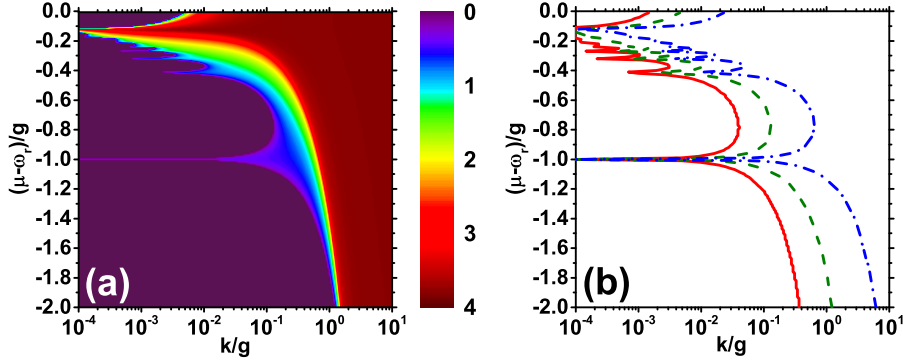


Figure 4.4: (a) The order parameter ψ in the $\mu \sim k$ plane. The parameters are $g = 1$, $\omega_r = 200$, $D = 100$, $\gamma_e = -10^3$, $\eta = 0.01$, $B_z = 0.0005\text{T}$, $\alpha = 0.2$, and $\Delta = 0$. The corresponding phase boundaries are plotted in (b), where the solid, dashed, and dot-dashed line denote $\alpha = 0, 0.2$, and 0.24 , respectively.

4.4 Dissipative effects

Generally, nonequilibrium processes such as the dissipative effect, are crucial in solid-state devices. We show that the signature of the Mott-superfluid transition remains even in the presence of the engineered dissipation by the quantum trajectory method [16; 123] (see Appendix I for details). By this approach, the non-Hermitian Hamiltonian is formulated as

$$H_{\text{diss}} = H^{\text{MF}} - \frac{i\Gamma}{2} \sum_p \sigma_p^+ \sigma_p^- - \frac{i\kappa}{2} \sum_p a_p^\dagger a_p, \quad (4.19)$$

where κ is the decay rate of the TLR, and Γ is the decay rate from the effective excited state $|e\rangle$ to the ground state $|g\rangle$ of the PCQ. In our case, the dissipative effects result from the unavoidable interaction between the PCQ/TLR and the corresponding Markovian environment; for example, the interaction between the output of the TLR and the corresponding vacuum field will result in photon escape into the environment. Here the dissipative effects of the NV are negligible, compared with κ and Γ . The phase diagrams under dissipative effects are displayed in Fig. 4.5. Once the hopping rate is increased beyond a critical value, the system is expected to undergo a nonequilibrium QPT from a MI phase, where the initial photon population imbalance between two resonators is self-trapped, to a SF phase where it coherently oscillates between the two TLRs [65]. Furthermore, another obvious feature is that the size of the MI phase becomes larger with the growth of dissipative rates. Note that the effective on-site repulsion becomes

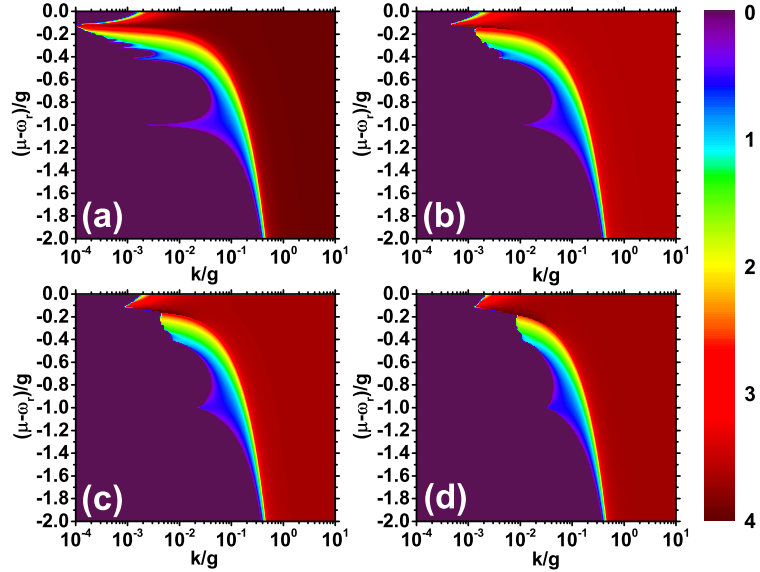


Figure 4.5: The order parameter ψ in the $\mu \sim k$ plane under different dissipative rates: (a) $\Gamma = \kappa = 0.01$, (b) $\Gamma = \kappa = 0.05$, (c) $\Gamma = \kappa = 0.1$, and (d) $\Gamma = \kappa = 0.15$. The other parameters are $g = 1$, $\omega_r = 200$, $D = 100$, $\gamma_e = -10^3$, $\eta = 0.01$, $B_z = 0.0005\text{T}$, and $\Delta = 0$.

stronger at lower excitation number as depicted in Fig. 4.2, which implies that the dissipative effect (inducing the decrease of the excitation number) favors the MI phase. As a result, the dissipation results in the dynamical switching from SF phase to MI phase and causes the enlargement of the size of MI phase.

4.5 Experimental feasibility

We briefly stress the relevant experimental progress. On one hand, it is possible to fabricate large arrays to observe many-body physics of interacting polaritons since resonators and qubits can be made lithographically [151]. Actually, it is indeed feasible to couple over 200 TLRs with negligible disorders (on the order of a few parts in 10^4) in a 2D lattice using a $32\text{mm} \times 32\text{mm}$ sample. This number can easily be extended to more than 1000 TLRs on a full two-inch wafer [65]. On the other hand, how to probe quantum many-body states of polaritons is still an open question in photonic quantum simulation [102]. The previous works suggested measuring the individual TLR through mapping the excitations into the qubit followed by obtaining the state-selective resonance fluorescence spectrum [5; 60; 61], but a remaining technical challenge is the realization

of high-efficiency photon detectors. Alternatively, the local statistical property of the TLR can be analyzed readily using combined techniques of photon-number-dependent qubit transition [74; 141] and fast readout of the qubit state through a separate low- Q resonator mode [92], for which the high-efficiency photon detectors are not required. Experimentally, transmission and reflection measurements for circuit-QED arrays have been implemented successfully in small systems with one or two resonators [22; 74; 160]. In order to distinguish between different phases of the system, one can also experimentally probe beyond transmission, such as by two-tone spectroscopy and a second-order coherence function (photon statistics) to reveal additional information [43; 144; 149]. For instance, by driving a TLR with a microwave source and detecting the output field of the other TLR, we could probe the properties of the system by independently detecting the correlation between two remote sites. The tunability of coupling strengths in our system enables one to measure these quantities relative straightforwardly.

Finally, we survey the relevant experimental parameters. Given the flexibility of circuit-QED, we can access a wide range of tunable experimental parameters for TLR-PCQ coupling strength g and hopping rate $k_{\langle p,q \rangle}$. Taking $L_r = 2\text{nH}$, $\omega_r/2\pi = 6\text{ GHz}$, $I_p = 600\text{nA}$, and $r = 0.2\mu\text{m}$, we get $\eta/2\pi \approx 140\text{KHz}$ and $g/2\pi \approx [1.8, 180]\text{MHz}$ when the distance d varies from $5\mu\text{m}$ to 50nm . In Ref. [153], the authors measured devices with photon hopping rates $k/2\pi$ from 0.8 to 31 MHz in resonator lattices. The electron-spin relaxation time T_1 of the NV ranges from 6 ms at room temperature [116] to $28\text{-}265\text{ s}$ at low temperature [59]. In addition, later experimental progress [6] with isotopically pure diamond has demonstrated a longer dephasing time to be $T_2 = 1.8\text{ms}$. Therefore, the dissipation and decoherence of the NV are negligible.

Chapter 5

Summary and outlook

In Chapter 2, we investigate the topological phase and the Majorana bound state in the spin-singlet superconductor with Rashba and Dresselhaus (110) spin-orbit couplings. In Sec. 2.4, we find that there exist flat Andreev bound states which host Majorana fermions in the s -wave Dresselhaus (110) superconductor. In Sec. 2.5, we study the topological properties of the spin-orbit coupled spin-singlet superconductor. Due to the particle-hole symmetry of the BdG Hamiltonian, we can use the Pfaffian invariant \mathcal{P} to demonstrate all the possible phase diagrams of the spin-singlet superconductor with Rashba and Dresselhaus (110) spin-orbit couplings. We find that only when the Hamiltonian has partial particle-hole symmetry or chiral symmetry, the edge spectrum is Majorana flat band protected by the edge index, namely, one dimensional Pfaffian invariant $\mathcal{P}(k_y)$ or the winding number $\mathcal{W}(k_y)$; otherwise the edge spectrum is Dirac cone. These edge indices can be used in determining the location of the zero-energy Majorana flat bands. The Majorana flat band implies a peak in the density of states which is clearly visible and can be detected in the transport measurements [7; 28; 109; 127; 164].

In Chapter 3, we use the Keldysh formalism to comprehensively study the two-lead tunneling in Majorana nanowire with and without short-range Coulomb interaction and disorder. A zero-bias dc conductance peak appears in our layout which implies the existence of Majorana fermion and is consistent with previous experiments on InSb nanowire [23; 27; 31; 40; 91; 109]. We find that since the Majorana fermion is a fermion that is its own antiparticle, there exists a hole transmission channel which makes the currents asymmetric at the left and right leads. This current asymmetry may be used as a criterion for detecting the Majorana fermion in our two-lead setup as depicted in Fig. 3.1. For the ac voltage, we find that the current response is enhanced in step with the increase of level broadening and the decrease of temperature, and finally saturates at high voltage.

The effects of short-range Coulomb interaction and disorder to the Majorana transport have been considered via bosonization method and renormalization group analysis. We find that there is a topological phase transition in the interplay of superconductivity and disorder. In the topological superconducting phase, the Majorana transport remains, otherwise the transport will destroy in the non-topological insulator phase.

In Chapter 4, we devise a concrete hybrid system to engineer a photonic Mott-superfluid phase transition in a 2D square lattice of TLRs coupled to a single NV encircled by a PCQ. We find that the interplay between the on-site repulsion and the photon tunneling leads to the photonic localization-delocalization transition (MI-SF transition). In the presence of dissipation, the phase diagram can be obtained by the mean-field approach and the quantum trajectory method. Facilitated by the good connectivity in circuit-QED, experiments combining both scalability and long coherence times are expected in the coming few years; at that stage the investigation of photonic quantum phase transition using TLR lattice systems can be realized.

We now discuss possible future research directions. For Part I, it is interesting to apply the recursive Green function method to explore the transport property of different kinds of junctions involving topological insulator, topological superconductor, ferromagnet, quantum dot and so on [18; 49; 78; 95; 157; 162]. We would like to study the influence of these junctions on the zero-bias conductance peak which is a signal of Majorana fermion. Meanwhile, we can also study the effects of magnetic field, interaction, Kondo impurity, disorder and geometry of device on the transport. For Part II, it is interesting to study simulations of many body physics by the cavity-QED and circuit-QED systems [22; 50; 65; 73; 93; 111; 117; 124; 160; 167]. For example, we would like to study simulation of the fractional quantum Hall effect by the cavity or circuit QED system [62].

Appendix A

Edge spectra of topological superconductor with mixed spin-singlet pairings

The superconductors with mixed s -wave and d -wave pairing symmetries are of the case (a), (f) and (g) in Tab. 2.1. For each case, there are three different kinds of phase diagrams depending on the hopping amplitude t as demonstrated in Fig. 2.5(b)-2.5(d). Although the edge spectrum becomes more complicated, there are no qualitative differences in the edge spectrum between the $d + s$ -wave superconductor and the pure d -wave or s -wave superconductor. The edge spectra for the $d_{x^2-y^2} + s$ -wave superconductor with Dresselhaus (110) spin-orbit coupling are shown in Fig. A.1. Due to the partial particle-hole symmetry and the chiral symmetry, the edge spectra of this kind of superconductor are Majorana flat bands protected by the Pfaffian invariant $\mathcal{P}(k_y)$ and the winding number $\mathcal{W}(k_y)$. Notice that in Fig. A.1(f) and Fig. A.1(t), the winding number $\mathcal{W}(k_y)$ in some range of k_y is 2, however, its parity namely the Pfaffian invariant $\mathcal{P}(k_y)$ is 1. Therefore, the phase is trivial in this range of k_y . The edge spectra for the $d_{x^2-y^2} + id_{xy} + s$ -wave superconductor with Rashba/Dresselhaus (110) spin-orbit coupling are shown in Fig. A.2 and Fig. A.3 respectively. Without protection of the partial particle-hole symmetry or the chiral symmetry, the Majorana flat bands disappear and become Dirac cones. In the nontrivial topological phase, we find that the edge spectra have an odd number of Dirac cones.

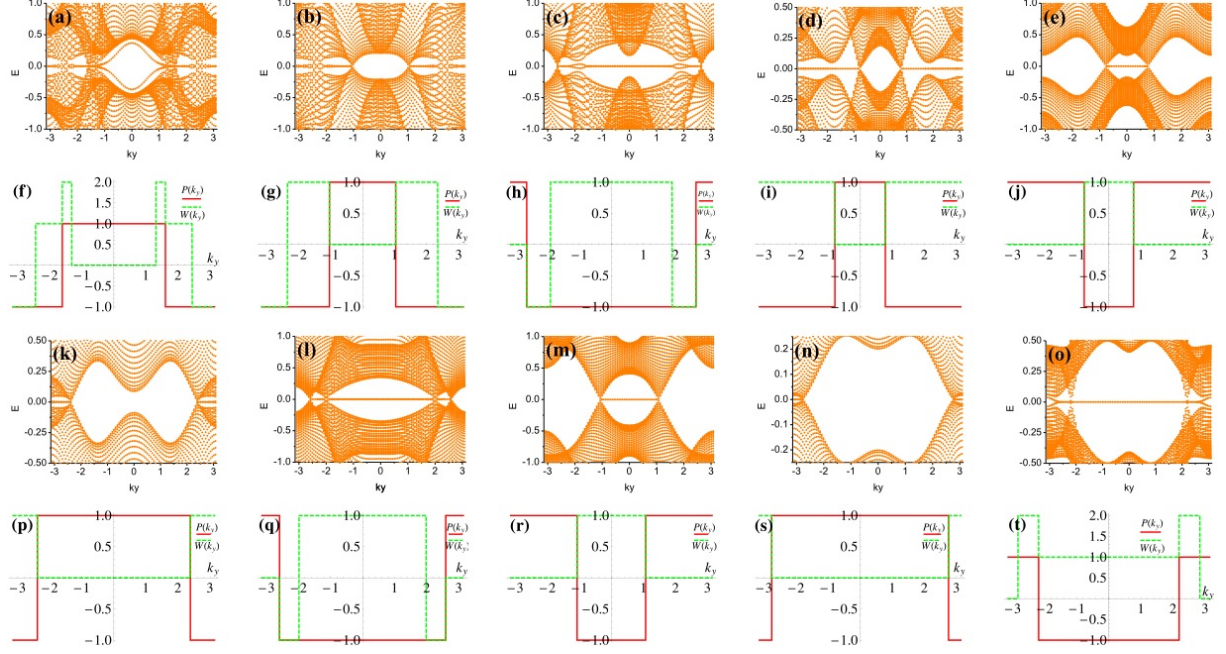


Figure A.1: (a)-(e) and (k)-(o) are the edge spectra of the $d_{x^2-y^2} + s$ -wave superconductor with Dresselhaus (110) spin-orbit coupling in case (f) of Tab. 2.1. There are three different kinds of phase diagrams depending on the hopping amplitude t as shown in Fig. 2.5(b)-2.5(d). For the phase diagram of Fig. 2.5(b), the edge spectra are demonstrated in (a), (b) and (c). The parameters are $t = 2$, $\beta = 1$, $\Delta_{s_1} = 1$, $\Delta_{d_1} = 2$ and (a) $\mu = 0, V^2 = 16$, (b) $\mu = -2.5, V^2 = 36$, (c) $\mu = -4, V^2 = 20$, which correspond to regions I, II and III in Fig. 2.5(b) respectively. (f), (g) and (h) are the Pfaffian invariant and winding number for (a), (b) and (c). For the phase diagram of Fig. 2.5(c), the edge spectra are demonstrated in (d), (e), (k) and (l). The parameters are $t = 1$, $\beta = 1$, $\Delta_{s_1} = 1$, $\Delta_{d_1} = 2$ and (d) $\mu = 0, V^2 = 12$, (e) $\mu = 0, V^2 = 20$, (k) $\mu = -1.8, V^2 = 30$, (l) $\mu = -4.5, V^2 = 25$, which correspond to regions I, II, III and IV in Fig. 2.5(c) respectively. (i), (j), (p) and (q) are the Pfaffian invariant and winding number for (d), (e), (k) and (l). For the phase diagram of Fig. 2.5(d), the edge spectra are demonstrated in (m), (n) and (o). The parameters are $t = 0.5$, $\beta = 1$, $\Delta_{s_1} = 1$, $\Delta_{d_1} = 2$ and (m) $\mu = 0, V^2 = 16$, (n) $\mu = -7, V^2 = 81$, (o) $\mu = -1, V^2 = 5$, which correspond to regions I, II and III in Fig. 2.5(d) respectively. (r), (s) and (t) are the Pfaffian invariant and winding number for (m), (n) and (o).

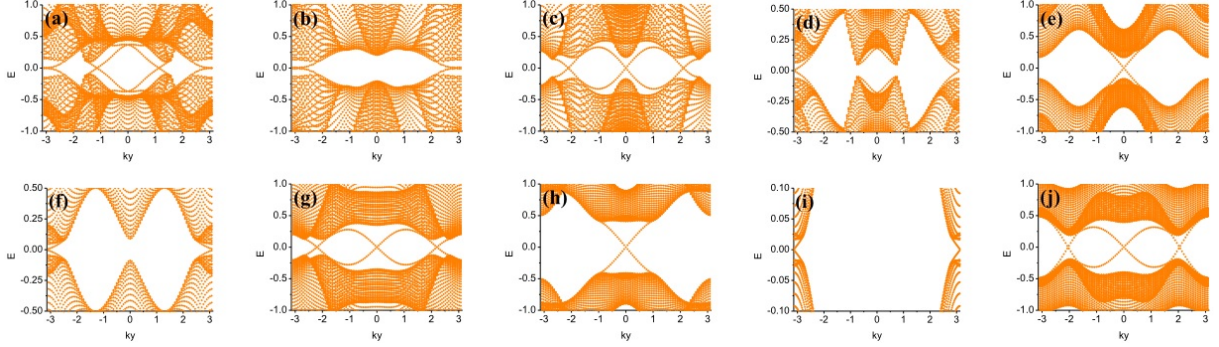


Figure A.2: (a)-(j) are the edge spectra of the $d_{x^2-y^2} + id_{xy} + s$ -wave superconductor with Rashba spin-orbit coupling in case (a) of Tab. 2.1. For the phase diagram of Fig. 2.5(b), the edge spectra are demonstrated in (a), (b) and (c). The parameters are $t = 2$, $\alpha = 1$, $\Delta_{s_1} = 1$, $\Delta_{s_2} = 0$, $\Delta_{d_1} = 2$, $\Delta_{d_2} = 1$ and (a) $\mu = 0, V_z = 4$, (b) $\mu = -2.5, V_z = 6$, (c) $\mu = -4, V_z = 2\sqrt{5}$, which correspond to regions I, II and III in Fig. 2.5(b) respectively. For the phase diagram of Fig. 2.5(c), the edge spectra are demonstrated in (d), (e), (f) and (g). The parameters are $t = 1$, $\alpha = 1$, $\Delta_{s_1} = 1$, $\Delta_{s_2} = 0$, $\Delta_{d_1} = 2$, $\Delta_{d_2} = 1$ and (d) $\mu = 0, V_z = 2\sqrt{3}$, (e) $\mu = 0, V_z = 2\sqrt{5}$, (f) $\mu = -1.8, V_z = \sqrt{30}$, (g) $\mu = -4.5, V_z = 5$, which correspond to regions I, II, III and IV in Fig. 2.5(c) respectively. For the phase diagram of Fig. 2.5(d), the edge spectra are demonstrated in (h), (i) and (j). The parameters are $t = 0.5$, $\alpha = 1$, $\Delta_{s_1} = 1$, $\Delta_{s_2} = 0$, $\Delta_{d_1} = 2$, $\Delta_{d_2} = 1$ and (h) $\mu = 0, V_z = 4$, (i) $\mu = -7, V_z = 9$, (j) $\mu = -3, V_z = 3$, which correspond to regions I, II and III in Fig. 2.5(d) respectively.

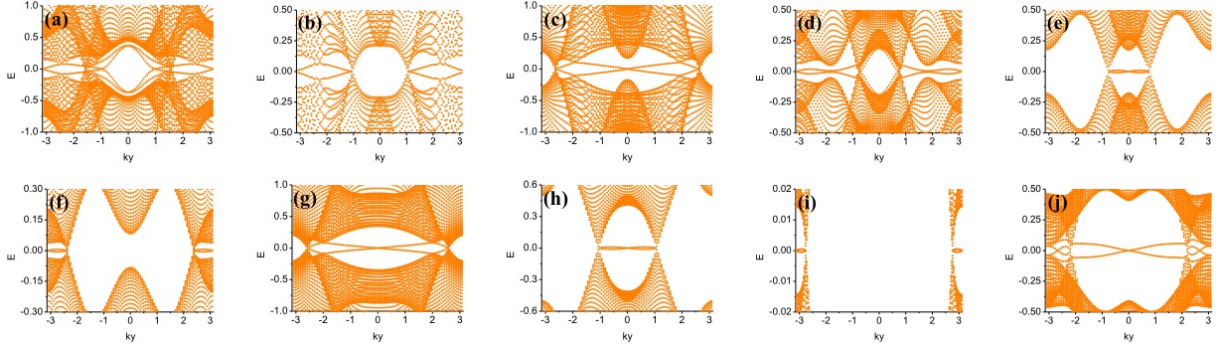


Figure A.3: (a)-(j) are the edge spectra of the $d_{x^2-y^2} + id_{xy} + s$ -wave superconductor with Dresselhaus (110) spin-orbit coupling in case (g) of Tab. 2.1. For the phase diagram of Fig. 2.5(b), the edge spectra are demonstrated in (a), (b) and (c). The parameters are $t = 2$, $\beta = 1$, $\Delta_{s_1} = 1$, $\Delta_{s_2} = 0$, $\Delta_{d_1} = 2$, $\Delta_{d_2} = 1$ and (a) $\mu = 0, V^2 = 16$, (b) $\mu = -2.5, V^2 = 36$, (c) $\mu = -4, V^2 = 20$, which correspond to regions I, II and III in Fig. 2.5(b) respectively. For the phase diagram of Fig. 2.5(c), the edge spectra are demonstrated in (d), (e), (f) and (g). The parameters are $t = 1$, $\beta = 1$, $\Delta_{s_1} = 1$, $\Delta_{s_2} = 0$, $\Delta_{d_1} = 2$, $\Delta_{d_2} = 1$ and (d) $\mu = 0, V^2 = 12$, (e) $\mu = 0, V^2 = 20$, (f) $\mu = -1.8, V^2 = 30$, (g) $\mu = -4.5, V^2 = 25$, which correspond to regions I, II, III and IV in Fig. 2.5(c) respectively. For the phase diagram of Fig. 2.5(d), the edge spectra are demonstrated in (h), (i) and (j). The parameters are $t = 0.5$, $\beta = 1$, $\Delta_{s_1} = 1$, $\Delta_{s_2} = 0$, $\Delta_{d_1} = 2$, $\Delta_{d_2} = 1$ and (h) $\mu = 0, V^2 = 16$, (i) $\mu = -7, V^2 = 81$, (j) $\mu = -1, V^2 = 5$, which correspond to regions I, II and III in Fig. 2.5(d) respectively.

Appendix B

Keldysh non-equilibrium Green function

The kernel of equilibrium many-body theory is the time-ordered Green function given by

$$G_c(t, t') = -i \frac{\langle \Psi_0 | T \{ \psi_H(t) \psi_H^\dagger(t') \} | \Psi_0 \rangle}{\langle \Psi_0 | \Psi_0 \rangle}, \quad (\text{B.1})$$

where T is the time-ordered operator, $\psi_H(t)$ is the field operator in the Heisenberg picture and Ψ_0 is the ground state of the full Hamiltonian. Here the full Hamiltonian can be divided into two parts, $H = H_0 + V$, where H_0 is the non-interacting part of the Hamiltonian in which the ground state Φ_0 can be easily obtained, and V is the interacting part of the Hamiltonian. However, the exact ground state Ψ_0 of the Hamiltonian H is generally hard to be acquired. To make any progress, we can express the exact ground state Ψ_0 in terms of quantities we know, for example the non-interacting ground state Φ_0 . These two states are related by the S -matrix as given in the Gell-Mann and Low theorem [101]:

$$|\Psi_0\rangle = S(0, -\infty)|\Phi_0\rangle. \quad (\text{B.2})$$

We have introduced the S -matrix which changes the wavefunction from $\psi(t')$ to $\psi(t)$: $\psi(t) = S(t, t')\psi(t')$. Therefore the traditional argument is that one starts in the remote past ($t = -\infty$) with the ground state $\psi(-\infty) = \Phi_0$ of the non-interacting Hamiltonian H_0 . The operator $S(0, -\infty)$ brings this wave function adiabatically up to the present $t = 0$. We now have the ground state $\psi(0) = \Psi_0$ which contains the effects of the

interaction V , so that it is an eigenstate of H . In equilibrium, one possible and reasonable assumption is that as $t \rightarrow +\infty$, $\psi(\infty) = S(\infty, 0)\Psi_0$ is equal to Φ_0 except for a phase factor. Therefore, the equilibrium time-ordered Green function can be rewritten as

$$G_c(t, t') = -i \frac{\langle \Phi_0 | T \{ S(\infty, -\infty) \psi_H(t) \psi_H^\dagger(t') \} | \Phi_0 \rangle}{\langle \Phi_0 | S(\infty, -\infty) | \Phi_0 \rangle}. \quad (\text{B.3})$$

Starting from this formula, the diagrammatic technique for calculating the equilibrium Green function perturbatively can be developed [101].

However, because in the non-equilibrium problem the irreversible effects break the symmetry between $t = -\infty$ and $t = +\infty$, the initial state at $t = -\infty$ is generally different from the final state at $t = +\infty$. This makes the assumption in equilibrium problem where the initial and final states are equal up to a phase factor invalid. Therefore, we cannot define the non-equilibrium Green function by virtue of Eq. (B.3).

For non-equilibrium problem, one can abandon this assumption by first evolving the Hamiltonian from $t = -\infty$ to the moment of interest τ , and then continuously evolving the Hamiltonian back in time from τ to $t = -\infty$. The advantage of this so-called Keldysh formalism is that one starts and ends with a known state $\psi(-\infty) = \Phi_0$ which is the eigenstate of H_0 and is usually the only state we know exactly. In this formalism one can define the Keldysh Green function as follows:

$$G(t, t') = -i \frac{\langle \Phi_0 | T_K \{ S(-\infty, -\infty) \psi_H(t) \psi_H^\dagger(t') \} | \Phi_0 \rangle}{\langle \Phi_0 | S(-\infty, -\infty) | \Phi_0 \rangle}, \quad (\text{B.4})$$

where T_K is the contour-ordered operator on the time loop as shown in Fig. B.1(a). This Keldysh contour contains two pieces: the outgoing branch L_1 from $t = -\infty$ to $t = +\infty$ and the ingoing branch L_2 from $t = +\infty$ to $t = -\infty$. The S -matrix, $S(-\infty, -\infty)$ should be interpreted in the contour-ordered sense [101]. With this definition Eq. (B.4), the contour-ordered Green function contains four different functions as shown in Fig. B.1(b)-(e),

$$G(t, t') = \begin{cases} G_c(t, t') & t, t' \in L_1 \\ G^>(t, t') & t \in L_2, t' \in L_1 \\ G^<(t, t') & t \in L_1, t' \in L_2 \\ G_{\bar{c}}(t, t') & t, t' \in L_2 \end{cases}, \quad (\text{B.5})$$

where $G_c(t, t')$ is the usual time-ordered Green function, $G_{\bar{c}}(t, t')$ is the anti-time-ordered

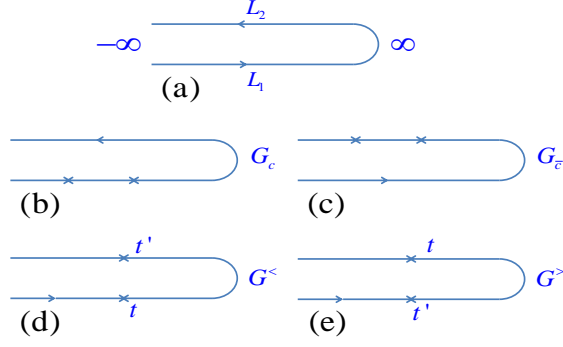


Figure B.1: the Keldysh contour (a) and the Keldysh Green function (b)-(e).

Green function, $G^>(t, t')$ is the greater Green function and $G^<(t, t')$ is the lesser Green function.

Next we study the analytic continuation of the Keldysh Green function. The main technical trick needed in the analytic continuation is Langreth Theorem. Considering the following product,

$$A(t, t') = \int_L d\tau B(t, \tau) C(\tau, t'), \quad (\text{B.6})$$

where L is the Keldysh contour. The lesser Green function is then given by

$$A^<(t, t') = \int_{L_1} d\tau B(t, \tau) C^<(\tau, t') + \int_{L_2} d\tau B^<(t, \tau) C(\tau, t'), \quad (\text{B.7})$$

where L_1 and L_2 are the outgoing and ingoing branches of the Keldysh contour L . Considering the first term and splitting the integral into two parts, we have

$$\begin{aligned} & \int_{L_1} d\tau B(t, \tau) C^<(\tau, t') \\ &= \int_{-\infty}^t dt_1 B^>(t, t_1) C^<(t_1, t') + \int_t^{-\infty} dt_1 B^<(t, t_1) C^<(t_1, t'), \\ &= \int_{-\infty}^{\infty} dt_1 \theta(t - t_1) (B^>(t, t_1) - B^<(t, t_1)) C^<(t_1, t'), \\ &= \int_{-\infty}^{\infty} dt_1 B^R(t, t_1) C^<(t_1, t'), \end{aligned} \quad (\text{B.8})$$

where $B^R(t, t_1)$ is the retarded Green function. Similarly, we have

$$\int_{L_2} d\tau B(t, \tau) C^<(\tau, t') = \int_{-\infty}^{\infty} dt_1 B^<(t, t_1) C^A(t_1, t'), \quad (\text{B.9})$$

where $C^A(t_1, t')$ is the advanced Green function. Finally, we arrive at

$$A^<(t, t') = \int_{-\infty}^{\infty} dt_1 [B^R(t, t_1) C^<(t_1, t') + B^<(t, t_1) C^A(t_1, t')]. \quad (\text{B.10})$$

Similarly, for the greater Green function, we have

$$A^>(t, t') = \int_{-\infty}^{\infty} dt_1 [B^R(t, t_1) C^>(t_1, t') + B^>(t, t_1) C^A(t_1, t')]. \quad (\text{B.11})$$

Usually, one also needs the retarded (or advanced) component of a product of Green functions defined on the Keldysh contour. We first express the retarded Green function in terms of the lesser and greater Green function [101],

$$A^R(t, t') = \theta(t - t') [A^>(t, t') - A^<(t, t')], \quad (\text{B.12})$$

then substituting the definitions of lesser and greater Green functions Eq. (B.10) and Eq. (B.11) into Eq. (B.12), we have

$$A^R(t, t') = \int_{t'}^t dt_1 B^R(t, t_1) C^R(t_1, t'). \quad (\text{B.13})$$

Similarly, the analytic continuation of the greater Green function is

$$A^A(t, t') = \int_t^{t'} dt_1 B^A(t, t_1) C^A(t_1, t'). \quad (\text{B.14})$$

Appendix C

Green function and self-energy for Majorana nanowire

Here we use the equation of motion method to study the Green function of the wire. The Keldysh Green function for the nanowire is defined as $G_{ij}(t, t') = -i\langle T_K \gamma_i(t) \gamma_j(t') \rangle$. We first consider the time evolution of this Green function. By definition

$$G_{ij}(t, t') = -i\theta(t - t')\langle \gamma_i(t) \gamma_j(t') \rangle + i\theta(t' - t)\langle \gamma_j(t') \gamma_i(t) \rangle, \quad (\text{C.1})$$

where $\theta(t - t')$ is defined on the Keldysh contour. Then we have

$$\partial_t G_{ij}(t, t') = -2i\delta(t - t')\delta_{i,j} - i\langle T_K \partial_t \gamma_i(t) \gamma_j(t') \rangle. \quad (\text{C.2})$$

Using the Heisenberg equation $i\partial_t \gamma_k(t) = [\gamma_k(t), H]$, where H is the Hamiltonian of the system, it is easy to check that the time evolution of Majorana operator is

$$i\partial_t \gamma_k(t) = -2i \sum_i t_{ik} \gamma_i(t) - \sum_{p,s=L,R} 2(V_{pk,s}^* c_{p,s}^\dagger(t) - V_{pk,s} c_{p,s}(t)). \quad (\text{C.3})$$

Substituting Eq. (C.3) into Eq. (C.2), after some calculations we have

$$\begin{aligned} i\partial_t G_{ij}(t, t') &= 2\delta(t - t')\delta_{i,j} + 2i \sum_k t_{ik} G_{kj}(t, t') \\ &\quad + 2 \sum_{p,s=L,R} (V_{pi,s} G_{pj,s}(t, t') - V_{pi,s}^* \bar{G}_{pj,s}(t, t')), \end{aligned} \quad (\text{C.4})$$

where the Green function for the tunnelings are given by

$$\begin{aligned} G_{pj,s}(t, t') &= -i\langle T_K c_{p,s}(t) \gamma_j(t') \rangle, \\ \bar{G}_{pj,s}(t, t') &= -i\langle T_K c_{p,s}^\dagger(t) \gamma_j(t') \rangle. \end{aligned} \quad (\text{C.5})$$

Similarly, we can use the equation of motion method [101] to express these two tunneling Green functions in terms of the wire Green function. for example, we have $(i\partial_t - \xi_{p,s})G_{pj,s}(t, t') = \sum_i V_{pi,s}^* G_{ij}(t, t')$ which leads to the following closed form for $G_{pj,s}(t, t')$,

$$G_{pj,s}(t, t') = \sum_i \int dt'' G_p^0(t, t'') V_{pi,s}^* G_{ij}(t'', t'), \quad (\text{C.6})$$

and similarly,

$$\bar{G}_{pj,s}(t, t') = - \sum_i \int dt'' \bar{G}_p^0(t, t'') V_{pi,s} G_{ij}(t'', t'), \quad (\text{C.7})$$

where the free lead Green function is defined as

$$\begin{aligned} G_p^0(t, t') &= -i\langle T_K c_p(t) c_p^\dagger(t') \rangle_0, \\ \bar{G}_p^0(t, t') &= -i\langle T_K c_p^\dagger(t) c_p(t') \rangle_0. \end{aligned} \quad (\text{C.8})$$

It is easy to check that the free lead Green functions satisfy the point charge source equation,

$$\begin{aligned} (i\partial_t - \xi_{p,L})G_p^0(t, t') &= \delta(t - t'), \\ (i\partial_t + \xi_{p,L})\bar{G}_p^0(t, t') &= \delta(t - t'), \end{aligned} \quad (\text{C.9})$$

which lead to the closed forms for $G_{pj,s}(t, t')$ and $\bar{G}_{pj,s}(t, t')$ respectively.

Therefore, substituting Eq. (C.6) and Eq. (C.7) into Eq. (C.4), we have

$$\begin{aligned} i\partial_t G_{ij}(t, t') &= 2\delta(t - t')\delta_{i,j} + 2i \sum_k t_{ik} G_{kj}(t, t') \\ &+ 2 \sum_{k,s=L,R} \int dt'' \Sigma_{ik,s}(t, t'') G_{kj}(t'', t'), \end{aligned} \quad (\text{C.10})$$

where the self-energy is $\Sigma_s = \Sigma_s^e + \Sigma_s^h$. The electron and hole self-energies are given by

$$\begin{aligned}\Sigma_{ik,s}^e(t, t'') &= \sum_p V_{pi,s}(t) G_{p,s}^0(t, t'') V_{pk,s}^*(t''), \\ \Sigma_{ik,s}^h(t, t'') &= \sum_p V_{pk,s}(t) \bar{G}_{p,s}^0(t, t'') V_{pi,s}^*(t'').\end{aligned}\tag{C.11}$$

We now study the retarded component of the self-energy $\Sigma_{ik}^R = \Sigma_{ik,L}^{eR} + \Sigma_{ik,R}^{eR} + \Sigma_{ik,L}^{hR} + \Sigma_{ik,R}^{hR}$, where

$$\begin{aligned}\Sigma_{ik,s}^{eR}(t, t'') &= \sum_p V_{pi,s}(t) G_{p,s}^{0R}(t, t'') V_{pk,s}^*(t''), \\ \Sigma_{ik,s}^{hR}(t, t'') &= \sum_p V_{pi,s}^*(t) \bar{G}_{p,s}^{0R}(t, t'') V_{pk,s}(t'').\end{aligned}\tag{C.12}$$

By the wide-band approximation, the retarded self-energy is

$$\Sigma_{ik,s}^{eR}(t, t'') = \int \frac{d\varepsilon}{2\pi} [\Gamma_s]_{ik} G_{p,s}^{0R}(t, t'').\tag{C.13}$$

Substituting the free retarded Green function in Appendix D into Eq. (C.13), the retarded self-energy for electron becomes

$$\Sigma_s^{eR}(t, t'') = -\frac{i}{2} \mathbf{\Gamma}_s(t) \delta(t - t'').\tag{C.14}$$

Similarly, the retarded self-energy for hole is

$$\Sigma_s^{hR}(t, t'') = -\frac{i}{2} \mathbf{\Gamma}_s^*(t) \delta(t - t'').\tag{C.15}$$

Therefore, the retarded self-energy for the Majorana nanowire is

$$\Sigma^R(t, t'') = -\frac{i}{2} \mathbf{\Gamma}(t) \delta(t - t''),\tag{C.16}$$

where $\mathbf{\Gamma}(t) = \mathbf{\Gamma}_L(t) + \mathbf{\Gamma}_R(t) + \mathbf{\Gamma}_L^*(t) + \mathbf{\Gamma}_R^*(t)$. Finally, by the analytic continuation [101] of Eq. (C.10), we have

$$i\partial_t G_{ij}^R(t, t') = 2\delta(t - t')\delta_{ij} + 2i \sum_k t_{ik} G_{kj}^R(t, t') + 2 \sum_k \int dt'' \Sigma_{ik}^R(t, t'') G_{kj}^R(t'', t').\tag{C.17}$$

Substituting Eq. (C.16) into it, we arrive at $[i\partial_t - 2i\mathbf{t} + i\mathbf{\Gamma}(t)]\mathbf{G}^R(t, t') = 2\delta(t - t')$, which

leads to the solution to the retarded Green function

$$\mathbf{G}^R(t, t') = -2i\theta(t - t')e^{\int_{t'}^t [2\mathbf{t} - \mathbf{\Gamma}(t'')]dt''}. \quad (\text{C.18})$$

Next we study the lesser self-energy of Majorana nanowire, $\Sigma_{ik}^<(t, t'') = \sum_{s=L,R} [\Sigma_{ik,s}^{e<}(t, t'') + \Sigma_{ik,s}^{h<}(t, t'')]$. By Eq. (C.11) and making use of the explicit expressions for the free Green functions in Appendix D and the level broadening matrix, we obtain

$$\Sigma_{ik}^<(t, t'') = i \sum_{s=L,R} \int \frac{d\varepsilon}{2\pi} e^{-i\varepsilon(t-t'')} f_s(\varepsilon) \{ [\Gamma_s(\varepsilon, t, t'')]_{ik} + [\Gamma_s^*(-\varepsilon, t, t'')]_{ik} \}. \quad (\text{C.19})$$

With the wide-band approximation, the lesser self-energy for the wire can be further reduced to

$$\Sigma^<(t, t'') = \sum_{s=L,R} \int \frac{d\varepsilon}{2\pi} e^{-i\varepsilon(t-t'')} [i f_s(\varepsilon)] [\mathbf{\Gamma}_s e^{ie \int_{t'}^t U_s(t')dt'} + \mathbf{\Gamma}_s^* e^{-ie \int_{t'}^t U_s(t')dt'}]. \quad (\text{C.20})$$

Appendix D

Useful expressions for the free Green functions

We first study the free lesser Green function $G_{p,s}^{0<}(t, t') = i\langle c_{p,s}^\dagger(t')c_{p,s}(t) \rangle_0$. By the equation of motion method, we find that this Green function satisfies the differential equation, $\partial_t G_{p,s}^{0<}(t, t') = -i\xi_{p,s}(t)G_{p,s}^{0<}(t, t')$, which has the solution $G_{p,s}^{0<}(t, t') = G_{p,s}^{0<}(t', t')e^{-i\int_{t'}^t \xi_{p,s}(t'')dt''}$. The coefficient $G_{p,s}^{0<}(t', t')$ is just the equilibrium Fermi function for the free electron with energy $\varepsilon_{p,s}$: $G_{p,s}^{0<}(t', t') = if_s(\varepsilon_{p,s}) = i/(e^{\beta\varepsilon_{p,s}} + 1)$. Therefore, we get

$$G_{p,s}^{0<}(t, t') = if_s(\varepsilon_{p,s})e^{-i\int_{t'}^t \xi_{p,s}(t'')dt''}, \quad (\text{D.1})$$

Similarly, it is easy to check that

$$\begin{aligned} G_{p,s}^{0>}(t, t') &= -i(1 - f_s(\varepsilon_{p,s}))e^{-i\int_{t'}^t \xi_{p,s}(t'')dt''}, \\ \overline{G}_{p,s}^{0<}(t, t') &= i(1 - f_s(\varepsilon_{p,s}))e^{i\int_{t'}^t \xi_{p,s}(t'')dt''}, \\ \overline{G}_{p,s}^{0>}(t, t') &= -if_s(\varepsilon_{p,s})e^{i\int_{t'}^t \xi_{p,s}(t'')dt''}. \end{aligned} \quad (\text{D.2})$$

We now calculate the retarded and advanced Green functions for the free electron [101]. By the relations, $G^R(t, t') = \theta(t - t')G^>(t, t') + \theta(t' - t)G^<(t, t') - G^<(t, t')$ and $G^A(t, t') = \theta(t - t')G^>(t, t') + \theta(t' - t)G^<(t, t') - G^>(t, t')$, and substituting the free lesser

and greater Green functions into these relations, we finally arrive at

$$\begin{aligned}
G_{p,s}^{0R}(t, t') &= -i\theta(t - t')e^{-i \int_{t'}^t \xi_{p,s}(t'')dt''}, \\
G_{p,s}^{0A}(t, t') &= i\theta(t' - t)e^{-i \int_{t'}^t \xi_{p,s}(t'')dt''}, \\
\overline{G}_{p,s}^{0R}(t, t') &= -i\theta(t - t')e^{i \int_{t'}^t \xi_{p,s}(t'')dt''}, \\
\overline{G}_{p,s}^{0A}(t, t') &= i\theta(t' - t)e^{i \int_{t'}^t \xi_{p,s}(t'')dt''}.
\end{aligned} \tag{D.3}$$

Appendix E

Fermion-boson correspondence in one dimension

In this appendix, we shall discuss the feasibility of standard Abelian bosonization formula as follows:

$$\begin{aligned}\psi_L(x) &= \frac{1}{\sqrt{2\pi\alpha}} e^{-i\sqrt{4\pi}\phi_L(x)}, \\ \psi_R(x) &= \frac{1}{\sqrt{2\pi\alpha}} e^{i\sqrt{4\pi}\phi_R(x)},\end{aligned}\tag{E.1}$$

where $\psi_{L/R}(x)$ and $\phi_{L/R}(x)$ are the massless Dirac field (fermionic) and massless Klein-Gordon field (bosonic) for the left/right mover respectively. α is the short-range cutoff for the convergence of the continuum theory. To demonstrate the relation of these two kinds of massless fields Eq. (E.1), we calculate the equal time correlation function in the ground state and check that if the results are identical in these two field theories.

Firstly, the Hamiltonian of a massless Dirac field can be formulated as

$$H_F = i\nu_F \int dx \left[\psi_L^\dagger(x) \partial_x \psi_L(x) - \psi_R^\dagger(x) \partial_x \psi_R(x) \right],\tag{E.2}$$

where ν_F is the Fermi velocity. The field operators are defined as follows ($\alpha \rightarrow 0$):

$$\begin{aligned}\psi_L(x) &= \frac{1}{\sqrt{2\pi}} \int_{-\infty}^{\infty} dk e^{ikx} a_{k,L} e^{-\alpha k/2}, \\ \psi_R(x) &= \frac{1}{\sqrt{2\pi}} \int_{-\infty}^{\infty} dk e^{ikx} a_{k,R} e^{-\alpha k/2},\end{aligned}\tag{E.3}$$

where $a_{k,L/R}$ is the annihilation operator for the left or right mover and satisfies the

fermionic commutation relation $\{a_{p,L/R}, a_{q,L/R}^\dagger\} = 2\pi\delta(p - q)$. Consider the equal time correlation function in the Fermi vacuum, for example,

$$\begin{aligned}
\langle \psi_R(x)\psi_R^\dagger(0) \rangle_0 &= \frac{1}{2\pi} \int_{-\infty}^{\infty} dk_1 dk_2 e^{ik_1 x} \langle a_{k_1,R} a_{k_2,R}^\dagger \rangle_0 e^{-\alpha(k_1+k_2)/2}, \\
&= \frac{1}{2\pi} \int_{-\infty}^{\infty} dk_1 dk_2 e^{ik_1 x} \delta_{k_1,k_2} \Theta(k_2) e^{-\alpha(k_1+k_2)/2}, \\
&= \frac{1}{2\pi} \int_0^{\infty} dk e^{ikx} e^{-\alpha k}, \\
&= \frac{1}{2\pi} \frac{1}{\alpha - ix}.
\end{aligned} \tag{E.4}$$

Here $\Theta(k)$ is the Heaviside step function.

Next we study the massless Klein-Gordon field, which is given by

$$H_B = \frac{\nu_F}{2} \int dx [\Pi^2 + (\partial_x \Phi)^2]. \tag{E.5}$$

Here the commutation relation is $[\Phi(x), \Pi(y)] = i\delta(x - y)$. In the particle interpretation, the canonical coordinate and momentum are $(\alpha \rightarrow 0)$

$$\begin{aligned}
\Phi(x) &= \int \frac{dk}{2\pi} \sqrt{\frac{\nu_F}{2\omega_k}} [b_k e^{ikx} + b_k^\dagger e^{-ikx}] e^{-\alpha|k|/2}, \\
\Pi(x) &= \int \frac{dk}{2\pi} \sqrt{\frac{\omega_k}{2\nu_F}} [-ib_k e^{ikx} + ib_k^\dagger e^{-ikx}] e^{-\alpha|k|/2},
\end{aligned} \tag{E.6}$$

where the dispersion is $\omega_k = \nu_F|k|$ and the bosonic commutation relation is $[b_k, b_{k'}^\dagger] = 2\pi\delta(k - k')$. Here we define two new fields $\phi_L(x)$ and $\phi_R(x)$, which are the superposition of the fields $\Phi(x)$ and $\Pi(x)$, and can be expressed as

$$\begin{aligned}
\phi_L(x) &= \frac{1}{2} \left[\Phi(x) + \int_{-\infty}^x \Pi(x') dx' \right], \\
\phi_R(x) &= \frac{1}{2} \left[\Phi(x) - \int_{-\infty}^x \Pi(x') dx' \right].
\end{aligned} \tag{E.7}$$

Substituting Eq. (E.6) into Eq. (E.7), we have

$$\begin{aligned}
\phi_L(x) &= \int_{-\infty}^0 \frac{dk}{2\pi\sqrt{2|k|}} [b_k e^{ikx} + b_k^\dagger e^{-ikx}] e^{-\alpha|k|/2}, \\
\phi_R(x) &= \int_0^{\infty} \frac{dk}{2\pi\sqrt{2|k|}} [b_k e^{ikx} + b_k^\dagger e^{-ikx}] e^{-\alpha|k|/2}.
\end{aligned} \tag{E.8}$$

The fields $\phi_L(x)$ and $\phi_R(x)$ satisfy simple commutation rules. By means of the commutation relation for boson, one can easily obtain

$$\begin{aligned}
[\phi_R(x), \phi_R(y)] &= \lim_{\mu \rightarrow 0} \int_{\mu}^{\infty} \frac{dk}{4\pi k} e^{-\alpha k} (e^{ik(x-y)} - e^{-ik(x-y)}), \\
&= \lim_{\mu \rightarrow 0} \int_{\mu}^{\infty} \frac{dk}{4\pi k} (e^{(-\alpha+i(x-y))k} - e^{(-\alpha-i(x-y))k}), \\
&= \frac{1}{4\pi} \lim_{\alpha \rightarrow 0} \ln \frac{-\alpha - i(x-y)}{-\alpha + i(x-y)}, \\
&= \frac{i}{4} \text{sign}(x-y).
\end{aligned} \tag{E.9}$$

Similarly, we have $[\phi_L(x), \phi_L(y)] = -\frac{i}{4} \text{sign}(x-y)$ and $[\phi_L(x), \phi_R(y)] = 0$.

Before proceed to the next calculation, we first give an operator identity as follows:

$$e^A e^B =: e^{A+B} : \exp \left[\left\langle AB + \frac{A^2 + B^2}{2} \right\rangle_0 \right], \tag{E.10}$$

where $::$ is the normal ordered operator which puts all creation operators to the left of all annihilation operators in a product, A and B are the linear superposition of creation and annihilation operators, and the average $\langle \rangle_0$ is with respect to the ground state. To show this identity, we first decompose the operators into two parts: $c = c^+ + c^-$, where c^+ and c^- are the creation and annihilation parts of the operator c and satisfy the commutation relation $[c^+, c^-] = \text{const.}$. Then using the Baker-Campbell-Hausdorff formula, $e^A = e^{A^+ + A^-} = e^{A^+} e^{A^-} e^{-\frac{1}{2}[A^+, A^-]}$, we have

$$\begin{aligned}
e^A e^B &= e^{A^+} e^{A^-} e^{-\frac{1}{2}[A^+, A^-]} e^{B^+} e^{B^-} e^{-\frac{1}{2}[B^+, B^-]}, \\
&= e^{A^+} e^{A^-} e^{B^+} e^{B^-} e^{-\frac{1}{2}[A^+, A^-]} e^{-\frac{1}{2}[B^+, B^-]}, \\
&= e^{A^+} e^{B^+} e^{A^-} e^{B^-} e^{[A^-, B^+]} e^{-\frac{1}{2}[A^+, A^-]} e^{-\frac{1}{2}[B^+, B^-]}, \\
&=: e^{A+B} : e^{[A^-, B^+]} e^{-\frac{1}{2}[A^+, A^-]} e^{-\frac{1}{2}[B^+, B^-]}.
\end{aligned} \tag{E.11}$$

For the average with respect to the ground state manifold, we have

$$\langle AB \rangle_0 = \langle (A^+ + A^-)(B^+ + B^-) \rangle_0 = \langle A^- B^+ \rangle_0 = [A^-, B^+]. \tag{E.12}$$

Substituting Eq. (E.12) into Eq. (E.11), finally we arrive at Eq. (E.10).

Now we calculate the equal time correlation function Eq. (E.4) by means of the

bosonization formula Eq. (E.1),

$$\begin{aligned}
\langle \psi_R(x) \psi_R^\dagger(0) \rangle_0 &= \frac{1}{2\pi\alpha} \langle e^{i\sqrt{4\pi}\phi_R(x)} e^{-i\sqrt{4\pi}\phi_R(0)} \rangle_0, \\
&= \frac{1}{2\pi\alpha} \langle : e^{i\sqrt{4\pi}[\phi_R(x)-\phi_R(0)]} : \rangle_0 \exp \left[4\pi \left\langle \phi_R(x)\phi_R(0) - \frac{\phi_R^2(x) + \phi_R^2(0)}{2} \right\rangle_0 \right], \\
&= \frac{1}{2\pi\alpha} \exp \left[4\pi \lim_{\mu \rightarrow 0} \int_{\mu}^{\infty} \frac{dk}{4\pi k} [e^{(ix-\alpha)k} - e^{-\alpha k}] \right], \\
&= \frac{1}{2\pi\alpha} \exp \left[\ln \frac{\alpha}{\alpha - ix} \right], \\
&= \frac{1}{2\pi} \frac{1}{\alpha - ix}.
\end{aligned} \tag{E.13}$$

It is found that the result is the same as direct calculation by the fermionic field as shown in Eq. (E.4). Therefore, we have established the fermion-boson correspondence Eq. (E.1) in one dimension.

Appendix F

Normal-ordered density operator

When we use the bosonization method to study the many-body physics in one dimension, after linearizing the energy spectrum in the whole Brillouin zone and considering the low-energy effective theory, we encounter the infinite density problem in one dimension because we have introduced an infinite number of occupied states [52]. One needs to define the density operator carefully to avoid this infinity. Here all the infinities are handled by normal ordering. This procedure can equivalently be done by subtracting ground state expectation value after point-splitting. As an example, the normal-ordered density operator can be defined as

$$\rho_R(x) =: \psi_R^\dagger(x)\psi_R(x) := \lim_{\delta \rightarrow 0} \left(\psi_R^\dagger(x + \delta)\psi_R(x) - \langle \psi_R^\dagger(x + \delta)\psi_R(x) \rangle_0 \right). \quad (\text{F.1})$$

Using the bosonization formula Eq. (E.1) and the operator identity Eq. (E.10), the first term can be calculated as

$$\begin{aligned} \lim_{\delta \rightarrow 0} \psi_R^\dagger(x + \delta)\psi_R(x) &= \frac{1}{2\pi\alpha} \lim_{\delta \rightarrow 0} e^{-i\sqrt{4\pi}\phi_R(x+\delta)} e^{i\sqrt{4\pi}\phi_R(x)}, \\ &= \frac{1}{2\pi\alpha} \lim_{\delta \rightarrow 0} : e^{-i\sqrt{4\pi}\delta\partial_x\phi_R(x)} : \frac{\alpha}{\alpha - i\delta}, \\ &\approx \lim_{\alpha \rightarrow 0} \frac{1}{2\pi\alpha} [1 - i\sqrt{4\pi}\delta\partial_x\phi_R(x)] \frac{\alpha}{\alpha - i\delta}, \\ &= \frac{i}{2\pi\delta} + \frac{1}{\sqrt{\pi}} \partial_x\phi_R(x). \end{aligned} \quad (\text{F.2})$$

Also by means of Eq. (E.10), the ground state expectation is infinite as expected and given by

$$\langle \psi_R^\dagger(x + \delta) \psi_R(x) \rangle_0 = \frac{1}{2\pi\alpha} \langle e^{-i\sqrt{4\pi}\phi_R(x+\delta)} e^{i\sqrt{4\pi}\phi_R(x)} \rangle_0 = \frac{i}{2\pi\delta}. \quad (\text{F.3})$$

Therefore, we obtain the normal-ordered density operator as

$$\rho_R(x) =: \psi_R^\dagger(x) \psi_R(x) := \frac{1}{\sqrt{\pi}} \partial_x \phi_R(x). \quad (\text{F.4})$$

We next study the normal-ordered kinetic energy as shown in Eq. (3.42). By expanding $: \psi_R^\dagger(x) \psi_R(x + \delta) :$ to the second order, we have

$$\begin{aligned} : \psi_R^\dagger(x) \psi_R(x + \delta) : &:= \frac{1}{\sqrt{\pi}} \partial_x \phi_R(x) + i\delta : (\partial_x \phi_R(x))^2 :, \\ : \psi_R^\dagger(x) \psi_R(x - \delta) : &:= \frac{1}{\sqrt{\pi}} \partial_x \phi_R(x) - i\delta : (\partial_x \phi_R(x))^2 :. \end{aligned} \quad (\text{F.5})$$

Then the kinetic energy for the right mover is given by

$$: \psi_R^\dagger(x) \frac{d}{dx} \psi_R(x) : =: \psi_R^\dagger(x) \frac{\psi_R(x + \delta) - \psi_R(x - \delta)}{2\delta} := i : [\partial_x \phi_R(x)]^2 :. \quad (\text{F.6})$$

Similarly, we have $: \psi_L^\dagger(x) \frac{d}{dx} \psi_L(x) := -i : [\partial_x \phi_L(x)]^2 :$. Substituting the normal-ordered kinetic energies of the left and right movers into Eq. (3.42), we bosonize the kinetic energy as shown in Eq. (3.57).

Appendix G

Replica method

To study the average value of an observable O in a disordered system, we first calculate the expectation value of the observable O in a specific configuration of a Gaussian disorder potential U , then average this expectation value $\langle O \rangle_U$ over all possible configurations of the disorder potential. By the path integral method, the expectation value for the potential U can be written as

$$\langle O \rangle_U = \frac{\int \mathcal{D}\varphi O(\varphi) e^{-S_U(\varphi)}}{\int \mathcal{D}\varphi e^{-S_U(\varphi)}}. \quad (\text{G.1})$$

Here $S_U(\varphi)$ is the action of the system for a given configuration of the disorder potential U ,

$$S_U(\varphi) = S_0(\varphi) + \int dx d\tau U(x) F(\varphi(x, \tau)), \quad (\text{G.2})$$

where $\tau = it$ is the imaginary time. We have to average over all the possible configurations of U to get the average value of the observables O in the disordered system. This can be accomplished by the following functional integral:

$$\langle O \rangle = \frac{\int \mathcal{D}U p(U) \langle O \rangle_U}{\int \mathcal{D}U p(U)}, \quad (\text{G.3})$$

where $p(U)$ is the Gaussian distribution of the random potential $p(U) = \exp[-\frac{1}{2D} \int dx U^2]$ and $\langle U(x)U(x') \rangle = D\delta(x - x')$.

The denominator in $\langle O \rangle_U$ is an obstacle for calculation. We omit it first, then the

expectation value of O is

$$\begin{aligned}\langle O \rangle &= \frac{\int \mathcal{D}U p(U) \int \mathcal{D}\varphi O(\varphi) e^{-S_U(\varphi)}}{\int \mathcal{D}U p(U)}, \\ &= \int \mathcal{D}\varphi O(\varphi) \exp[-S_{\text{eff}}(\varphi)],\end{aligned}\tag{G.4}$$

where the effective action is

$$S_{\text{eff}}(\varphi) = S_0(\varphi) - \frac{D}{2} \int dx d\tau d\tau' F(\varphi(x, \tau)) F(\varphi(x, \tau')).\tag{G.5}$$

The presence of the denominator in $\langle O \rangle_U$ prevents us from doing the average as above. However, we can use the replica method to transform the denominator into numerator by the following trick:

$$\frac{1}{\int \mathcal{D}\varphi e^{-S_U(\varphi)}} = \lim_{m \rightarrow 0} \left[\int \mathcal{D}\varphi e^{-S_U(\varphi)} \right]^{m-1}.\tag{G.6}$$

The tradeoff is that we introduce another $m - 1$ copies of φ fields and need to do a m -dimensional Gaussian functional integral. The average is now given by

$$\langle O \rangle = \frac{\int \mathcal{D}U p(U) \int \prod_{i=1}^m \mathcal{D}\varphi_i O(\varphi_1) e^{-\sum_{a=1}^m S_U(\varphi_a)}}{\int \mathcal{D}U p(U)}.\tag{G.7}$$

After integrating the m -dimensional Gaussian functional integral, we finally achieve

$$\langle O \rangle = \int \prod_{i=1}^m \mathcal{D}\varphi_i O(\varphi_1) e^{-S_{\text{eff}}},\tag{G.8}$$

where

$$S_{\text{eff}} = \sum_{a=1}^m S_0(\varphi_a) - \frac{D}{2} \sum_{a,b=1}^m \int dx d\tau d\tau' F(\varphi_a(x, \tau)) F(\varphi_b(x, \tau')).\tag{G.9}$$

At the end of the integration, we take m to 0 to get the expectation value of the observable O in the disordered system. Therefore, we can evaluate any observable in the disordered system by Eq. (G.8).

Appendix H

Renormalization analysis of correlation function

Here we first give some details of the calculation of correlation $R(r_1 - r_2) = \langle e^{ia\sqrt{2}\varphi(r_1)} e^{-ia\sqrt{2}\varphi(r_2)} \rangle_{H_{\text{dw}}}$, and then do a RG analysis for this correlation function. Substituting this correlation into the replica method Eq. (3.68), and expanding D to the first order and Δ to the second order, up to the first leading terms in D and Δ , we have $R(r_1 - r_2) = R_0 + R_\Delta + R_D$, where

$$\begin{aligned}
 R_0 &= \langle e^{ia\sqrt{2}\varphi(r_1)} e^{-ia\sqrt{2}\varphi(r_2)} \rangle_0, \\
 R_\Delta &= \frac{\Delta^2 \sin^2 \gamma_{k_F}}{8(\pi\alpha u)^2} \sum_{\epsilon=\pm 1} \int d^2 r' d^2 r'' [\langle e^{ia\sqrt{2}\varphi(r_1)} e^{-ia\sqrt{2}\varphi(r_2)} e^{i2\epsilon\theta(r')} e^{-i2\epsilon\theta(r'')} \rangle_0 \\
 &\quad - \langle e^{ia\sqrt{2}\varphi(r_1)} e^{-ia\sqrt{2}\varphi(r_2)} \rangle_0 \langle e^{i2\epsilon\theta(r')} e^{-i2\epsilon\theta(r'')} \rangle_0], \\
 R_D &= \frac{D \cos^2 \gamma_{k_F}}{8(\pi\alpha u)^2} \sum_{\epsilon=\pm 1} \int d^2 r' d^2 r'' \delta(x' - x'') [\langle e^{ia\sqrt{2}\varphi(r_1)} e^{-ia\sqrt{2}\varphi(r_2)} e^{i2\epsilon\varphi(r')} e^{-i2\epsilon\varphi(r'')} \rangle_0 \\
 &\quad - \langle e^{ia\sqrt{2}\varphi(r_1)} e^{-ia\sqrt{2}\varphi(r_2)} \rangle_0 \langle e^{i2\epsilon\varphi(r')} e^{-i2\epsilon\varphi(r'')} \rangle_0].
 \end{aligned} \tag{H.1}$$

The average $\langle \rangle_0$ is performed for the Luttinger Hamiltonian H_{Lutt} in Eq. (3.62). These correlation functions can be calculated by the following formula [52]:

$$\langle \prod_j e^{iA_j \phi(r_j)} \prod_j e^{iB_j \theta(s_j)} \rangle_0 = e^{\frac{1}{2} \sum_{i<j} A_i A_j K F_1(r_i - r_j)} e^{\frac{1}{2} \sum_{i<j} B_i B_j K^{-1} F_1(s_i - s_j)} e^{-\frac{1}{2} \sum_{i,j} A_i B_j F_2(r_i - s_j)}, \tag{H.2}$$

where $r = (x, u\tau)$ and $s = (x', u\tau')$. Notice that the correlations are nonzero only when the coefficients A_i and B_i satisfy the neutral conditions: $\sum_i A_i = 0$ and $\sum_i B_i = 0$,

otherwise the correlations are vanishing. The functions

$$\begin{aligned} F_1(r) &= \frac{1}{2} \ln \frac{x^2 + (u|\tau| + \alpha)^2}{\alpha^2}, \\ F_2(r) &= -i \text{Arg}(y_\alpha + ix), \end{aligned} \quad (\text{H.3})$$

are the real and imaginary parts of the analytic function $\ln(y_\alpha - ix)$, where $y_\alpha = u\tau + \alpha \text{sign}(\tau)$.

For the R_Δ term, Using Eq. (H.2), and replacing the integration variables by $r' = R + \frac{r}{2}$ and $r'' = R - \frac{r}{2}$, we have

$$R_\Delta = \frac{\Delta^2 \sin^2 \gamma_{k_F}}{4(\pi\alpha u)^2} \int d^2 R d^2 r e^{-a^2 K F_1(r_1 - r_2)} e^{-2K^{-1} F_1(r)} [a^2 (r \cdot \nabla_R [F_2(r_1 - R) - F_2(r_2 - R)])]^2. \quad (\text{H.4})$$

Since $F_1(r)$ and $F_2(r)$ are the real and imaginary parts of the analytic function $\ln(y_\alpha - ix)$, they obey the standard Cauchy relations: $\nabla_X F_1 = i \nabla_Y F_2$, $\nabla_Y F_1 = -i \nabla_X F_2$, where $R = (X, Y)$. Thus R_Δ can be further reduced to

$$\begin{aligned} R_\Delta &= \frac{\Delta^2 \sin^2 \gamma_{k_F}}{4(\pi\alpha u)^2} \int d^2 R d^2 r e^{-a^2 K F_1(r_1 - r_2)} e^{-2K^{-1} F_1(r)} \frac{a^2 r^2}{2} \\ &\quad \times [(F_1(r_1 - R) - F_1(r_2 - R))(\nabla_X^2 + \nabla_Y^2)(F_1(r_1 - R) - F_1(r_2 - R))]. \end{aligned} \quad (\text{H.5})$$

Note that $F_1(r)$ is essentially $\ln(r/\alpha)$ because the short-range cutoff $\alpha \ll r$. Therefore, one can apply the identity $(\nabla_X^2 + \nabla_Y^2) \log(R) = 2\pi\delta(R)$ to Eq. (H.5), and finally find that

$$R_\Delta = -\frac{\Delta^2 \alpha^2 a^2 \sin^2 \gamma_{k_F}}{u^2} e^{-a^2 K F_1(r_1 - r_2)} F_1(r_1 - r_2) \int_\alpha^\infty \frac{dr}{\alpha} \left(\frac{r}{\alpha}\right)^{3-2K^{-1}}. \quad (\text{H.6})$$

By the similar technique, we can obtain the R_D term as follows,

$$R_D = \frac{D a^2 K^2 \cos^2 \gamma_{k_F}}{4(\pi\alpha u)^2} e^{-a^2 K F_1(r_1 - r_2)} [J_+ I_+(r_1 - r_2) + J_- I_-(r_1 - r_2)], \quad (\text{H.7})$$

where

$$\begin{aligned} J_\pm &= \int d^2 r \delta(x) e^{-2K F_1(r)} (x^2 \pm y^2), \\ I_\pm(r_1 - r_2) &= \int d^2 R F_1(r_1 - R) (\nabla_X^2 \pm \nabla_Y^2) F_1(R - r_2). \end{aligned} \quad (\text{H.8})$$

Substituting $F_1(r) = \ln(r/\alpha)$ into Eq. (H.8), we have

$$\begin{aligned}
J_+ &= 2\alpha^3 \int \frac{dr}{\alpha} \left(\frac{r}{\alpha}\right)^{2-2K}, \\
J_- &= -2\alpha^3 \int \frac{dr}{\alpha} \left(\frac{r}{\alpha}\right)^{2-2K}, \\
I_+(r_1 - r_2) &= 2\pi F_1(r_1 - r_2), \\
I_-(r_1 - r_2) &= \pi \cos 2\theta_{r_1 - r_2}.
\end{aligned} \tag{H.9}$$

Finally, we obtain that the R_D term is

$$R_D = \frac{D\alpha a^2 K^2 \cos^2 \gamma_{k_F}}{2\pi u^2} e^{-a^2 K F_1(r_1 - r_2)} [2F_1(r_1 - r_2) - \cos 2\theta_{r_1 - r_2}] \int_{\alpha}^{\infty} \frac{dr}{\alpha} \left(\frac{r}{\alpha}\right)^{2-2K}, \tag{H.10}$$

where θ_r is the angle between the vector $r = (x, u\tau)$ and the x -axis. Notice that the $\delta(x)$ term in Eq. (H.8) makes x and $u\tau$ inequivalent in R_D term. Thus the space and time are asymmetric and have to be renormalized separately. We set

$$F_t(r_1 - r_2) = F_1(r_1 - r_2) + \frac{t}{K} \cos 2\theta_{r_1 - r_2}, \tag{H.11}$$

where t parameterizes the anisotropy between the space and time directions, and $t = 0$ in the original Hamiltonian but will be generalized during the renormalization due to the $\delta(x)$ term.

Therefore, keeping the zeroth order term of t during the renormalization, the correlation for the whole Hamiltonian should be

$$\begin{aligned}
R(r_1 - r_2) &= e^{-a^2 K F_t(r_1 - r_2)} \left\{ 1 - a^2 F_1(r_1 - r_2) \left[y_{\Delta}^2 \int \frac{dr}{\alpha} \left(\frac{r}{\alpha}\right)^{3-2K^{-1}} - y_D K^2 \int \frac{dr}{\alpha} \left(\frac{r}{\alpha}\right)^{2-2K} \right] \right. \\
&\quad \left. - a^2 \frac{y_D K^2}{2} \cos 2\theta_{r_1 - r_2} \int \frac{dr}{\alpha} \left(\frac{r}{\alpha}\right)^{2-2K} \right\},
\end{aligned} \tag{H.12}$$

where $y_{\Delta} = \frac{\alpha \Delta \sin \gamma_{k_F}}{u}$ and $y_D = \frac{\alpha D \cos^2 \gamma_{k_F}}{\pi u^2}$. It is worth noting that $R(r_1 - r_2)$ is structurally identical to the correlation function of Luttinger Hamiltonian Eq. (3.62), $R_0(r_1 - r_2) = e^{-a^2 K F_t(r_1 - r_2)}|_{t=0}$. Quantitatively, this structural similarity can be achieved by re-exponentiating Eq. (H.12), and comparing with $R_0(r_1 - r_2)$. We find that an effective Luttinger Hamiltonian with renormalized K_{eff} and t_{eff} shown below will gen-

erate the same correlation of the original Luttinger Hamiltonian (without disorder and superconductivity),

$$\begin{aligned} K_{\text{eff}} &= K + y_{\Delta}^2 \int_{\alpha}^{\infty} \frac{dr}{\alpha} \left(\frac{r}{\alpha}\right)^{3-2K^{-1}} - y_D K^2 \int_{\alpha}^{\infty} \frac{dr}{\alpha} \left(\frac{r}{\alpha}\right)^{2-2K}, \\ t_{\text{eff}} &= t + \frac{y_D K^2}{2} \int_{\alpha}^{\infty} \frac{dr}{\alpha} \left(\frac{r}{\alpha}\right)^{2-2K}. \end{aligned} \quad (\text{H.13})$$

Note that generally the Luttinger parameters K_{eff} and t_{eff} are divergent in one dimension. However, since the Luttinger parameters determine the correlations and thus physical properties of the system, they should be independent of the short-range cutoff α . It is necessary to keep the divergent Luttinger parameters as constants to preserve the physical properties of the system. Therefore, we can use the following renormalization procedure to extract useful information from these infinities. For K_{eff} , by writing the integral $\int_{\alpha}^{\infty} = \int_{\alpha}^{\alpha e^l} + \int_{\alpha e^l}^{\infty}$, integrating the first part, and rescaling the second part $\alpha e^l \rightarrow \alpha$, we observe that when

$$\begin{aligned} K(l) &= K(0) + y_{\Delta}^2(0) \frac{e^{[4-2K^{-1}(0)]l} - 1}{4 - 2K^{-1}(0)} - y_D(0) K^2(0) \frac{e^{[3-2K(0)]l} - 1}{3 - 2K(0)}, \\ y_{\Delta}^2(l) &= y_{\Delta}^2(0) e^{[4-2K^{-1}(0)]l}, \\ y_D(l) K^2(l) &= y_D(0) K^2(0) e^{[3-2K(0)]l}, \end{aligned} \quad (\text{H.14})$$

K_{eff} is unchanged. Sending l to zero, we have

$$\begin{aligned} \frac{dK}{dl} &= y_{\Delta}^2 - y_D K^2, \\ \frac{dy_{\Delta}}{dl} &= (2 - K^{-1}) y_{\Delta}, \\ \frac{dy_D}{dl} &= 2K y_D^2 - (2K - 3 + 2K^{-1} y_{\Delta}^2) y_D. \end{aligned} \quad (\text{H.15})$$

Similarly, for the t_{eff} , we have

$$\frac{dt}{dl} = \frac{y_D K^2}{2}. \quad (\text{H.16})$$

For the form of $F_t(r)$, a renormalization of t is equivalent to a renormalization of the velocity u by

$$-\frac{2}{K} \frac{dt}{dl} = \frac{1}{u} \frac{du}{dl}. \quad (\text{H.17})$$

Therefore, we have

$$\frac{du}{dl} = -y_D K u. \quad (\text{H.18})$$

Given a set of initial parameters, the Hamiltonian with parameters generated by the above renormalization flow equations is in the same phase. Thus we can use these renormalization flows to depict the phase diagram of the system.

Appendix I

Quantum trajectory method

We consider the Lindblad master equation of the mean field Hamiltonian Eq. (4.15) for studying the dissipative effects,

$$\frac{d\rho}{dt} = i[\rho, H^{MF}] + \mathcal{L}(\rho), \quad (\text{I.1})$$

where ρ is the density matrix of the hybrid circuit-QED system and the Lindblad term is

$$\mathcal{L}(\rho) = \frac{\Gamma}{2} \sum_i (2\sigma_i^- \rho \sigma_i^+ - \sigma_i^+ \sigma_i^- \rho - \rho \sigma_i^+ \sigma_i^-) + \frac{\kappa}{2} \sum_i (2a_i \rho a_i^\dagger - a_i^\dagger a_i \rho - \rho a_i^\dagger a_i). \quad (\text{I.2})$$

Here κ is the decay rate of the TLR, and Γ is the decay rate from the effective excited state $|e\rangle$ of the PCQ. The quantum trajectory method is essentially a Monte-Carlo simulation [107; 108]. Considering at time t the system is in a state with normalized wave function $|\phi(t)\rangle$, then at time $t + \delta t$, the wavefunction $|\phi(t + \delta t)\rangle$ is renewed by the following two steps:

1. a quantum jump to a new state $C_l|\phi(t)\rangle$ with probability $\delta p_l = \delta t \langle \phi(t) | C_l^\dagger C_l | \phi(t) \rangle$, where $C_l = \sqrt{\Gamma} \sigma_l^-$ or $\sqrt{\kappa} a_l$;
2. time-evolve the wavefunction $|\phi(t)\rangle$ as $e^{-iH_{\text{eff}}\delta t}|\phi(t)\rangle$ with probability $1 - \delta p$, where $\delta p = \sum_l \delta p_l$ and the effective non-Hermitian Hamiltonian is

$$H_{\text{eff}} = H^{\text{MF}} - \frac{i\Gamma}{2} \sum_i \sigma_i^+ \sigma_i^- - \frac{i\kappa}{2} \sum_i a_i^\dagger a_i. \quad (\text{I.3})$$

Note that the wave function at time $t + \delta t$ obtained by the step 1 and 2 should be normalized by $\sqrt{\delta p_l/\delta t}$ and $\sqrt{1 - \delta p}$ respectively. With this evolution, when the system is initially in the state $\rho(t) = |\phi(t)\rangle\langle\phi(t)|$, after one Monte-Carlo step, the density matrix becomes

$$\begin{aligned} \rho(t + \delta t) = & (1 - \delta p) \frac{e^{-iH_{\text{eff}}\delta t} |\phi(t)\rangle \langle\phi(t)| e^{iH_{\text{eff}}^\dagger \delta t}}{\sqrt{1 - \delta p} \sqrt{1 - \delta p}} \\ & + \sum_m \delta p_m \frac{\sqrt{\Gamma} \sigma_m^- |\phi(t)\rangle \langle\phi(t)| \sqrt{\Gamma} \sigma_m^+}{\sqrt{\delta p_m/\delta t} \sqrt{\delta p_m/\delta t}} + \sum_n \delta p_n \frac{\sqrt{\kappa} a_n |\phi(t)\rangle \langle\phi(t)| \sqrt{\kappa} a_n^\dagger}{\sqrt{\delta p_n/\delta t} \sqrt{\delta p_n/\delta t}}. \end{aligned} \quad (\text{I.4})$$

By Taylor expansion of the evolution operator $e^{-iH_{\text{eff}}\delta t} \approx 1 - iH_{\text{eff}}\delta t$ and keeping the δt terms in Eq. (I.4) to the first order, we have

$$\begin{aligned} \rho(t + \delta t) = & \rho(t) + i\delta t[\rho(t), H^{MF}] \\ & + \frac{\Gamma\delta t}{2} \sum_m (2\sigma_m^- \rho(t) \sigma_m^+ - \sigma_m^+ \sigma_m^- \rho(t) - \rho(t) \sigma_m^+ \sigma_m^-) \\ & + \frac{\kappa\delta t}{2} \sum_n (2a_n \rho(t) a_n^\dagger - a_n^\dagger a_n \rho(t) - \rho(t) a_n^\dagger a_n), \\ = & \rho(t) + i\delta t[\rho(t), H^{MF}] + \delta t\mathcal{L}(\rho(t)). \end{aligned} \quad (\text{I.5})$$

Putting δt to zero, the master equation (I.1) of the system is recovered. Therefore, we can use Monte-Carlo method described above to solve the master equation (I.1).

If the dissipations Γ and κ are small enough, which is the case we considered in the Mott-superfluid transition in Sec. 4.4, we can neglect the quantum jump step 1 and only study the system governed by the effective non-Hermitian Hamiltonian H_{eff} as shown in step 2. This is equivalent to replace $\omega_r \rightarrow \omega_r - i\kappa/2$ and $\omega_0 \rightarrow \omega_0 - i\Gamma/2$ in the mean-field Hamiltonian Eq. (4.15).

Bibliography

- [1] ABDUFARRUKH A. ABDUMALIKOV, OLEG ASTAFIEV, YASUNOBU NAKAMURA, YURI A. PASHKIN, AND JAWSHEN TSAI. Vacuum rabi splitting due to strong coupling of a flux qubit and a coplanar-waveguide resonator. *Phys. Rev. B*, **78**:180502, Nov 2008. [58](#)
- [2] I. AHARONOVICH, S. CASTELLETTO, D. A. SIMPSON, C.-H. SU, A. D. GREENTREE, AND S. PRAWER. Diamond-based single-photon emitters. *Rep.Prog.Phys*, **74**:076501, 2011. [57](#)
- [3] JASON ALICEA. Majorana fermions in a tunable semiconductor device. *Phys. Rev. B*, **81**:125318, Mar 2010. [1](#), [6](#), [31](#)
- [4] JASON ALICEA, YUVAL OREG, GIL REFAEL, FELIX VON OPPEN, AND MATTHEW P. A. FISHER. Non-abelian statistics and topological quantum information processing in 1d wire networks. *Nat. Phys.*, **7**:412, 2011. [1](#), [6](#), [31](#)
- [5] DIMITRIS G. ANGELAKIS, MARCELO FRANCA SANTOS, AND SOUGATO BOSE. Photon-blockade-induced mott transitions and xy spin models in coupled cavity arrays. *Phys. Rev. A*, **76**:031805, Sep 2007. [68](#)
- [6] G. BALASUBRAMANIAN, P. NEUMANN, D. TWITCHEN, M. MARKHAM, R. KOLESOV, N. MIZUOCHI, J. ISOYA, J. ACHARD, J. BECK, J. TISSLER, V. JACQUES, P. R. HEMMER, F. JELEZKO, AND J. WRACHTRUP. Ultralong spin coherence time in isotopically engineered diamond. *Nature Materials*, **8**:383, 2009. [69](#)
- [7] T. V. BAY, T. NAKA, Y. K. HUANG, H. LUIGJES, M. S. GOLDEN, AND A. DE VISSER. Superconductivity in the doped topological insulator $\text{Cu}_x\text{Bi}_2\text{Se}_3$ under high pressure. *Phys. Rev. Lett.*, **108**:057001, Jan 2012. [6](#), [70](#)

- [8] B. ANDREI BERNEVIG AND SHOU-CHENG ZHANG. Quantum spin hall effect. *Phys. Rev. Lett.*, **96**:106802, Mar 2006. [6](#)
- [9] K. M. BIRNBAUM, A. BOCA, R. MILLER, A. D. BOOZER, T. E. NORTHUP, AND H. J. KIMBLE. Photon blockade in an optical cavity with one trapped atom. *Nature*, **436**:87, 2005. [65](#)
- [10] ALEXANDRE BLAIS, REN-SHOU HUANG, ANDREAS WALLRAFF, S. M. GIRVIN, AND R. J. SCHOELKOPF. Cavity quantum electrodynamics for superconducting electrical circuits: An architecture for quantum computation. *Phys. Rev. A*, **69**:062320, Jun 2004. [57](#)
- [11] ALEXANDRE BLAIS, ALEXANDER MAASSEN VAN DEN BRINK, AND ALEXANDRE M. ZAGOSKIN. Tunable coupling of superconducting qubits. *Phys. Rev. Lett.*, **90**:127901, Mar 2003. [62](#)
- [12] C. J. BOLECH AND EUGENE DEMLER. Observing majorana bound states in p -wave superconductors using noise measurements in tunneling experiments. *Phys. Rev. Lett.*, **98**:237002, Jun 2007. [2](#), [32](#)
- [13] JANEZ BONCA AND SERGEI KRUCHININ. *Electron Transport in Nanosystems*. Springer, 2007. [41](#), [43](#)
- [14] P. M. R. BRYDON, ANDREAS P. SCHNYDER, AND CARSTEN TIMM. Topologically protected flat zero-energy surface bands in noncentrosymmetric superconductors. *Phys. Rev. B*, **84**:020501, Jul 2011. [1](#), [6](#), [7](#)
- [15] I. BULUTA AND F. NORI. Quantum simulators. *Science*, **326**:108, 2009. [57](#)
- [16] H. CARMICHAEL. *An Open Systems Approach to Quantum Optics*. Springer-Verlag Berlin, 1993. [3](#), [67](#)
- [17] C CAROLI, R COMBESCOT, NOZIERES P, AND SAINT-JAMES D. Direct calculation of the tunneling current. *J. Phys. C: Solid State Phys.*, **4**:916, 1971. [41](#)
- [18] JORGE CAYAO, ELSA PRADA, PABLO SAN-JOSE, AND RAMÓN AGUADO. Sns junctions in nanowires with spin-orbit coupling: Role of confinement and helicity on the subgap spectrum. *Phys. Rev. B*, **91**:024514, Jan 2015. [71](#)

- [19] W. CHANG, V. E. MANUCHARYAN, T. S. JESPERSEN, J. NYGÅRD, AND C. M. MARCUS. Tunneling spectroscopy of quasiparticle bound states in a spinful josephson junction. *Phys. Rev. Lett.*, **110**:217005, May 2013. [2](#)
- [20] MENG CHENG AND HONG-HAO TU. Majorana edge states in interacting two-chain ladders of fermions. *Phys. Rev. B*, **84**:094503, Sep 2011. [32](#), [46](#)
- [21] L. CHILDRESS, M. V. G. DUTT, J. M. TAYLOR, A. S. ZIBROV, F. JELEZKO, J. WRACHTRUP, P. R. HEMMER, AND M. D. LUKIN. Coherent dynamics of coupled electron and nuclear spin qubits in diamond. *Science*, **314**:281, 2006. [57](#)
- [22] I. CHIORESCU, P. BERTET, K. SEMBA, Y. NAKAMURA, C.J.P.M. HARMANS, AND J. E. MOOIJ. Coherent dynamics of a flux qubit coupled to a harmonic oscillator. *Nature*, **431**:159, 2004. [3](#), [56](#), [69](#), [71](#)
- [23] H. O. H. CHURCHILL, V. FATEMI, K. GROVE-RASMUSSEN, M. T. DENG, P. CAROFF, H. Q. XU, AND C. M. MARCUS. Superconductor-nanowire devices from tunneling to the multichannel regime: Zero-bias oscillations and magnetoconductance crossover. *Phys. Rev. B*, **87**:241401, Jun 2013. [2](#), [31](#), [70](#)
- [24] DAVID J. CLARKE, JAY D. SAU, AND SUMANTA TEWARI. Majorana fermion exchange in quasi-one-dimensional networks. *Phys. Rev. B*, **84**:035120, Jul 2011. [31](#)
- [25] JOHN CLARKE AND FRANK K. WILHELM. Superconducting quantum bits. *Nature*, **453**:1031, 2008. [57](#)
- [26] S. M. CRONENWETT, H. J. LYNCH, D. GOLDHABER-GORDON, L. P. KOUWENHOVEN, C. M. MARCUS, K. HIROSE, N. S. WINGREEN, AND V. UMANSKY. Low-temperature fate of the 0.7 structure in a point contact: A kondo-like correlated state in an open system. *Phys. Rev. Lett.*, **88**:226805, May 2002. [43](#)
- [27] ANINDYA DAS, YUVAL RONEN, YONATAN MOST, YUVAL OREG, MOTY HEIBLUM, AND HADAS SHTRIKMAN. Transport signatures of floquet majorana fermions in driven topological superconductors. *Nature Physics*, **8**:887, 2012. [2](#), [31](#), [70](#)
- [28] ANINDYA DAS, YUVAL RONEN, YONATAN MOST, YUVAL OREG, MOTY HEIBLUM, AND HADAS SHTRIKMAN. Zero-bias peaks and splitting in an al-inas

- nanowire topological superconductor as a signature of majorana fermions. *Nat. Phys.*, **8**:887, Nov 2012. [2](#), [6](#), [70](#)
- [29] SANKAR DAS SARMA, MICHAEL FREEDMAN, AND CHETAN NAYAK. Topologically protected qubits from a possible non-abelian fractional quantum hall state. *Phys. Rev. Lett.*, **94**:166802, Apr 2005. [1](#)
- [30] SUPRIYO DATTA. *Quantum Transport: Atom to Transistor*. Cambridge University Press, 2005. [2](#), [32](#), [38](#), [41](#)
- [31] M. T. DENG, C. L. YU, G. Y. HUANG, M. LARSSON, P. CAROFF, AND H. Q. XU. Anomalous zero-bias conductance peak in a nb-insb nanowire-nb hybrid device. *Nano Letters*, **12**[12]:6414–6419, 2012. [2](#), [31](#), [70](#)
- [32] M. T. DENG, C. L. YU, G. Y. HUANG, M. LARSSON, P. CAROFF, AND H. Q. XU. Parity independence of the zero-bias conductance peak in a nanowire based topological superconductor-quantum dot hybrid device. *Scientific Reports*, **4**:7261, 2014. [2](#), [32](#)
- [33] SHUSA DENG, GERARDO ORTIZ, AMRIT POUDEL, AND LORENZA VIOLA. Majorana flat bands in *s*-wave gapless topological superconductors. *Phys. Rev. B*, **89**:140507, Apr 2014. [1](#), [6](#)
- [34] L. DICARLO, M. D. REED, L. SUN, B. R. JOHNSON, J. M. CHOW, J. M. GAMBETTA, L. FRUNZIO, S. M. GIRVIN, M. H. DEVORET, AND R. J. SCHOELKOPF. Preparation and measurement of three-qubit entanglement in a superconducting circuit. *Nature*, **467**:574, 2010. [3](#), [57](#)
- [35] M. V. G. DUTT, , L. CHILDRESS, L. JIANG, E. TOGAN, J. MAZE, F. JELEZKO, A. S. ZIBROV, P. R. HEMMER, AND M. D. LUKIN. Quantum register based on individual electronic and nuclear spin qubits in diamond. *Science*, **316**:1312, 2007. [57](#)
- [36] DONG E. LIU, MENG CHENG, AND ROMAN M. LUTCHYN. Probing majorana physics in quantum dot shot noise experiments. *arXiv:1409.3860v2*. [2](#), [32](#)
- [37] ERIK ERIKSSON. Spin-orbit interactions in a helical luttinger liquid with a kondo impurity. *Phys. Rev. B*, **87**:235414, Jun 2013. [33](#)

- [38] ROSARIO FAZIO AND HERRE VAN DER ZANT. Quantum phase transitions and vortex dynamics in superconducting networks. *Physics Reports*, **355**[4]:235 – 334, 2001. [3](#), [56](#)
- [39] LUKASZ FIDKOWSKI, ROMAN M. LUTCHYN, CHETAN NAYAK, AND MATTHEW P. A. FISHER. Majorana zero modes in one-dimensional quantum wires without long-ranged superconducting order. *Phys. Rev. B*, **84**:195436, Nov 2011. [32](#), [46](#)
- [40] A. D. K. FINCK, D. J. VAN HARLINGEN, P. K. MOHSENI, K. JUNG, AND X. LI. Anomalous modulation of a zero-bias peak in a hybrid nanowire-superconductor device. *Phys. Rev. Lett.*, **110**:126406, Mar 2013. [1](#), [2](#), [31](#), [70](#)
- [41] MICHAEL FLEISCHHAUER, JOHANNES OTTERBACH, AND RAZMIK G. UNANYAN. Bose-einstein condensation of stationary-light polaritons. *Phys. Rev. Lett.*, **101**:163601, Oct 2008. [56](#)
- [42] KARSTEN FLENSBERG. Tunneling characteristics of a chain of majorana bound states. *Phys. Rev. B*, **82**:180516, Nov 2010. [2](#), [32](#), [42](#)
- [43] M. FRANÇA SANTOS, L. G. LUTTERBACH, S. M. DUTRA, N. ZAGURY, AND L. DAVIDOVICH. Reconstruction of the state of the radiation field in a cavity through measurements of the outgoing field. *Phys. Rev. A*, **63**:033813, Feb 2001. [4](#), [69](#)
- [44] PER FRÖJDH AND HENRIK JOHANNESSON. Magnetic impurity in a luttinger liquid: A conformal field theory approach. *Phys. Rev. B*, **53**:3211–3236, Feb 1996. [32](#)
- [45] LIANG FU AND C. L. KANE. Superconducting proximity effect and majorana fermions at the surface of a topological insulator. *Phys. Rev. Lett.*, **100**:096407, Mar 2008. [1](#), [6](#), [31](#), [33](#), [34](#)
- [46] LIANG FU, C. L. KANE, AND E. J. MELE. Topological insulators in three dimensions. *Phys. Rev. Lett.*, **98**:106803, Mar 2007. [6](#)
- [47] T. GAEBEL, M. DOMHAN, I. POPA, C. WITTMANN, P. NEUMANN, F. JELEZKO, J. R. RABEAU, N. STAVRIAS, A. D. GREENTREE, S. PRAWER, J. MEIJER, J. TWAMLEY, P. R. HEMMER, AND J. WRACHTRUP. Room-temperature coherent coupling of single spins in diamond. *Nature Physics*, **2**:408, 2006. [57](#)

- [48] SUHAS GANGADHARAIHAH, JIANMIN SUN, AND OLEG A. STARYKH. Spin-orbital effects in magnetized quantum wires and spin chains. *Phys. Rev. B*, **78**:054436, Aug 2008. [32](#), [51](#)
- [49] JOSE H. GARCÍA, LUCIAN COVACI, AND TATIANA G. RAPPOPORT. Real-space calculation of the conductivity tensor for disordered topological matter. *Phys. Rev. Lett.*, **114**:116602, Mar 2015. [71](#)
- [50] M. GEORGESCU, I. S. ASHHAB, AND FRANCO NORI. Quantum simulation. *Rev. Mod. Phys.*, **86**:153–185, Mar 2014. [3](#), [56](#), [71](#)
- [51] PARAG GHOSH, JAY D. SAU, SUMANTA TEWARI, AND S. DAS SARMA. Non-abelian topological order in noncentrosymmetric superconductors with broken time-reversal symmetry. *Phys. Rev. B*, **82**:184525, Nov 2010. [13](#), [20](#), [31](#)
- [52] T. GIAMARCHI. *Quantum Physics in One Dimension*. Clarendon Press, 2003. [32](#), [46](#), [50](#), [51](#), [53](#), [90](#), [94](#)
- [53] T. GIAMARCHI AND H. J. SCHULZ. Anderson localization and interactions in one-dimensional metals. *Phys. Rev. B*, **37**:325–340, Jan 1988. [32](#), [46](#)
- [54] D. GOLDHABER-GORDON, HADAS SHTRIKMAN, D. MAHALU, DAVID ABUSCHMAGDER, U. MEIRAV, AND M. A. KASTNER. Kondo effect in a single-electron transistor. *Nature*, **391**:156, 1998. [41](#), [43](#)
- [55] ANDREW D. GREENTREE AND ANDREW M. MARTIN. Breaking time reversal symmetry with light. *Physics*, **3**:85, Oct 2010. [3](#), [57](#), [62](#), [66](#)
- [56] ANDREW D. GREENTREE, CHARLES TAHAN, JARED H. COLE, AND LLOYD C. L. HOLLENBERG. Quantum phase transitions of light. *Nature Physics*, **2**:856, 2006. [56](#), [62](#), [63](#), [65](#)
- [57] MARKUS GREINER, OLAF MANDEL, TILMAN ESSLINGER, THEODOR W. HÄNSCH, AND IMMANUEL BLOCH. Quantum phase transition from a superfluid to a mott insulator in a gas of ultracold atoms. *Nature*, **415**:39, 2002. [3](#)
- [58] F. D. M. HALDANE. Model for a quantum hall effect without landau levels: Condensed-matter realization of the "parity anomaly". *Phys. Rev. Lett.*, **61**:2015–2018, Oct 1988. [6](#)

- [59] J. HARRISON, M.J. SELLARS, AND N.B. MANSON. Measurement of the optically induced spin polarisation of n-v centres in diamond. *Diamond and Related Materials*, **15**:586 – 588, 2006. [69](#)
- [60] MICHAEL J. HARTMANN, FERNANDO G. S. L. BRANDÃO, AND MARTIN B. PLENIO. Strongly interacting polaritons in coupled arrays of cavities. *Nature Physics*, **2**:849, 2006. [56](#), [68](#)
- [61] M.J. HARTMANN, F.G.S.L. BRANDÃO, AND M.B. PLENIO. Quantum many-body phenomena in coupled cavity arrays. *Laser and Photonics Reviews*, **2**[6]:527–556, 2008. [56](#), [68](#)
- [62] ANDREW L. C. HAYWARD, ANDREW M. MARTIN, AND ANDREW D. GREENTREE. Fractional quantum hall physics in jaynes-cummings-hubbard lattices. *Phys. Rev. Lett.*, **108**:223602, Jun 2012. [71](#)
- [63] JAMES J. HE, JIANGSHENG WU, TING-PONG CHOY, XIONG-JUN LIU, Y. TANAKA, AND K. T. LAW. Correlated spin currents generated by resonant-crossed andreev reflections in topological superconductors. *Nature Communications*, **5**:3232, 2014. [41](#)
- [64] A. J. HOFFMAN, S. J. SRINIVASAN, S. SCHMIDT, L. SPIETZ, J. AUMENTADO, H. E. TÜRECI, AND A. A. HOUCK. Dispersive photon blockade in a superconducting circuit. *Phys. Rev. Lett.*, **107**:053602, Jul 2011. [65](#)
- [65] ANDREW A. HOUCK, HAKAN E. TÜRECI, AND KOCH JENS. On-chip quantum simulation with superconducting circuits. *Nature Physics*, **8**:292, 2012. [3](#), [56](#), [57](#), [66](#), [67](#), [68](#), [71](#)
- [66] TIMOTHY H. HSIEH AND LIANG FU. Majorana fermions and exotic surface andreev bound states in topological superconductors: Application to $\text{Cu}_x\text{Bi}_2\text{Se}_3$. *Phys. Rev. Lett.*, **108**:107005, Mar 2012. [1](#), [6](#)
- [67] YONG HU AND LIN TIAN. Deterministic generation of entangled photons in superconducting resonator arrays. *Phys. Rev. Lett.*, **106**:257002, Jun 2011. [62](#)
- [68] THOMAS HÜMMER, GEORG M. REUTHER, PETER HÄNGGI, AND DAVID ZUECO. Nonequilibrium phases in hybrid arrays with flux qubits and nitrogen-vacancy centers. *Phys. Rev. A*, **85**:052320, May 2012. [57](#)

- [69] R. HÜTZEN, A. ZAZUNOV, B. BRAUNECKER, A. LEVY YEYATI, AND R. EGGER. Majorana single-charge transistor. *Phys. Rev. Lett.*, **109**:166403, Oct 2012. [32](#)
- [70] D. A. IVANOV. Non-abelian statistics of half-quantum vortices in p-wave superconductors. *Phys. Rev. Lett.*, **86**:268–271, Jan 2001. [31](#)
- [71] ANTTI-PEKKA JAUHO, NED S. WINGREEN, AND YIGAL MEIR. Time-dependent transport in interacting and noninteracting resonant-tunneling systems. *Phys. Rev. B*, **50**:5528–5544, Aug 1994. [2](#), [32](#), [35](#), [36](#), [38](#)
- [72] L. JIANG, J. S. HODGES, J. R. MAZE, P. MAURER, J. M. TAYLOR, D. G. CORY, P. R. HEMMER, R. L. WALSWORTH, A. YACOBY, A. S. ZIBROV, AND M. D. LUKIN. Repetitive readout of a single electronic spin via quantum logic with nuclear spin ancillae. *Science*, **326**:267, 2009. [57](#)
- [73] JIASEN JIN, DAVIDE ROSSINI, ROSARIO FAZIO, MARTIN LEIB, AND MICHAEL J. HARTMANN. Photon solid phases in driven arrays of nonlinearly coupled cavities. *Phys. Rev. Lett.*, **110**:163605, Apr 2013. [3](#), [56](#), [71](#)
- [74] B. R. JOHNSON, M. D. REED, A. A. HOUCK, D. I. SCHUSTER, LEV S. BISHOP, E. GINOSSAR, J. M. GAMBETTA, L. DICARLO, L. FRUNZIO, S. M. GIRVIN, AND R. J. SCHOELKOPF. Quantum non-demolition detection of single microwave photons in a circuit. *Nature Physics*, **6**:663, 2010. [4](#), [69](#)
- [75] A. KAMAL, J. CLARKE, AND M. H. DEVORET. Noiseless non-reciprocity in a parametric active device. *Nature Physics*, **7**:311, 2011. [62](#)
- [76] C. L. KANE AND E. J. MELE. Quantum spin hall effect in graphene. *Phys. Rev. Lett.*, **95**:226801, Nov 2005. [6](#)
- [77] C. L. KANE AND E. J. MELE. Z_2 topological order and the quantum spin hall effect. *Phys. Rev. Lett.*, **95**:146802, Sep 2005. [6](#)
- [78] OLEKSIY KASHUBA AND CARSTEN TIMM. Topological kondo effect in transport through a superconducting wire with multiple majorana end states. *Phys. Rev. Lett.*, **114**:116801, Mar 2015. [71](#)
- [79] A. KITAEV. Unpaired majorana fermions in quantum wires. *Phys. Usp.*, **44**:131, 2001. [1](#), [6](#), [7](#), [31](#), [34](#), [35](#)

- [80] A.YU. KITAEV. Fault-tolerant quantum computation by anyons. *Annals of Physics*, **303**[1]:2 – 30, 2003. [6](#), [31](#)
- [81] JENS KOCH, ANDREW A. HOUCK, KARYN LE HUR, AND S. M. GIRVIN. Time-reversal-symmetry breaking in circuit-qed-based photon lattices. *Phys. Rev. A*, **82**:043811, Oct 2010. [3](#), [57](#), [62](#), [66](#)
- [82] JENS KOCH AND KARYN LE HUR. Superfluid-mott-insulator transition of light in the jaynes-cummings lattice. *Phys. Rev. A*, **80**:023811, Aug 2009. [56](#)
- [83] MARKUS KÖNIG, HARTMUT BUHMANN, LAURENS W. MOLENKAMP, TAYLOR HUGHES, CHAO-XING LIU, XIAO-LIANG QI, AND SHOU-CHENG ZHANG. The quantum spin hall effect: Theory and experiment. *Journal of the Physical Society of Japan*, **77**[3]:031007, 2008. [6](#)
- [84] J M KOSTERLITZ. *J. Phys. C: Solid State Phys.*, **7**:1046, 1974. [52](#)
- [85] TILL D. KÜHNER, STEVEN R. WHITE, AND H. MONIEN. One-dimensional bose-hubbard model with nearest-neighbor interaction. *Phys. Rev. B*, **61**:12474–12489, May 2000. [62](#)
- [86] ARIJIT KUNDU AND BABAK SERADJEH. Transport signatures of floquet majorana fermions in driven topological superconductors. *Phys. Rev. Lett.*, **111**:136402, Sep 2013. [2](#), [32](#)
- [87] CHRISTIAN KURTSIEFER, SONJA MAYER, PATRICK ZARDA, AND HARALD WEINFURTER. Stable solid-state source of single photons. *Phys. Rev. Lett.*, **85**:290–293, Jul 2000. [57](#)
- [88] MAHMOUD LABABIDI AND ERHAI ZHAO. Nearly flat andreev bound states in superconductor-topological insulator hybrid structures. *Phys. Rev. B*, **86**:161108, Oct 2012. [1](#), [6](#)
- [89] C. LANG, D. BOZYIGIT, C. EICHLER, L. STEFFEN, J. M. FINK, A. A. ABDUMALIKOV, M. BAUR, S. FILIPP, M. P. DA SILVA, A. BLAIS, AND A. WALLRAFF. Observation of resonant photon blockade at microwave frequencies using correlation function measurements. *Phys. Rev. Lett.*, **106**:243601, Jun 2011. [65](#)
- [90] K. T. LAW, PATRICK A. LEE, AND T. K. NG. Majorana fermion induced resonant andreev reflection. *Phys. Rev. Lett.*, **103**:237001, Dec 2009. [2](#), [31](#)

- [91] EDUARDO J. H. LEE, XIAOCHENG JIANG, MANUEL HOUZET, RAMON AGUADO, CHARLES M. LIEBER, AND SILVANO DE FRANCESCHI. Spin-resolved andreev levels and parity crossings in hybrid superconductor/semiconductor nanostructures. *Nature Nanotechnology*, **9**:79, 2014. [2](#), [31](#), [70](#)
- [92] P. J. LEEK, M. BAUR, J. M. FINK, R. BIANCHETTI, L. STEFFEN, S. FILIPP, AND A. WALLRAFF. Cavity quantum electrodynamics with separate photon storage and qubit readout modes. *Phys. Rev. Lett.*, **104**:100504, Mar 2010. [4](#), [69](#)
- [93] G. LEPERT, TRUPKE M., HARTMANN M. J., PLENIO M. B., AND E. A. HINDS. Arrays of waveguide-coupled optical cavities that interact strongly with atoms. *New Journal of Physics*, **13**:113002, 2011. [3](#), [56](#), [71](#)
- [94] MACIEJ LEWENSTEIN, ANNA SANPERA, VERONICA AHUFINGER, BOGDAN DAMSKI, ADITI SEN(De), AND UJJWAL SEN. Ultracold atomic gases in optical lattices: mimicking condensed matter physics and beyond. *Advances in Physics*, **56**[2]:243–379, 2007. [3](#), [56](#)
- [95] JIE LIU, JIAN WANG, AND FU-CHUN ZHANG. Controllable nonlocal transport of majorana fermions with the aid of two quantum dots. *Phys. Rev. B*, **90**:035307, Jul 2014. [71](#)
- [96] XIONG-JUN LIU AND ALEJANDRO M. LOBOS. Manipulating majorana fermions in quantum nanowires with broken inversion symmetry. *Phys. Rev. B*, **87**:060504, Feb 2013. [32](#), [46](#), [51](#)
- [97] ALEJANDRO M. LOBOS, ROMAN M. LUTCHYN, AND S. DAS SARMA. Interplay of disorder and interaction in majorana quantum wires. *Phys. Rev. Lett.*, **109**:146403, Oct 2012. [32](#), [51](#), [52](#), [53](#)
- [98] E. LUCERO, R. BARENDTS, Y. CHEN, J. KELLY, M. MARIANTONI, A. MEGRANT, P. O’MALLEY, D. SANK, A. VAINSENER, J. WENNER, T. WHITE, Y. YIN, A. N. CLELAND, AND J. M. MARTINIS. Computing prime factors with a josephson phase qubit quantum processor. *Nature Physics*, **8**:719, 2012. [3](#), [57](#)
- [99] ROMAN M. LUTCHYN, JAY D. SAU, AND S. DAS SARMA. Majorana fermions and a topological phase transition in semiconductor-superconductor heterostructures. *Phys. Rev. Lett.*, **105**:077001, Aug 2010. [31](#)

- [100] ROMAN M. LUTCHYN AND JACOB H. SKRABACZ. Transport properties of topological superconductor-luttinger liquid junctions: A real-time keldysh approach. *Phys. Rev. B*, **88**:024511, Jul 2013. [2](#), [32](#)
- [101] GERALD D. MAHAN. *Many-Particle Physics*. Plenum Press, 1990. [36](#), [37](#), [40](#), [76](#), [77](#), [79](#), [81](#), [82](#), [84](#)
- [102] D. MARCOS, A. TOMADIN, S. DIEHL, AND P. RABL. Photon condensation in circuit quantum electrodynamics by engineered dissipation. *New Journal of Physics*, **14**:055005, 2012. [68](#)
- [103] M. MARIANTONI, H. WANG, R. C. BIALCZAK, M. LENANDER, E. LUCERO, M. NEELEY, A. D. O'CONNELL, D. SANK, M. WEIDES, J. WENNER, T. YAMAMOTO, Y. YIN, J. ZHAO, J. M. MARTINIS, AND A. N. CLELAND. Photon shell game in three-resonator circuit quantum electrodynamics. *Nature Physics*, **7**:287, 2011. [3](#), [57](#)
- [104] JENS MARTIN, SHAHAL ILANI, BASILE VERDENE, JURGEN SMET, VLADIMIR UMANSKY, DIANA MAHALU, DIETER SCHUH, GERHARD ABSTREITER, AND AMIR YACOBY. Localization of fractionally charged quasi-particles. *Science*, **305**:980, Aug 2004. [1](#), [6](#)
- [105] JOHN M. MARTINIS, S. NAM, J. AUMENTADO, AND C. URBINA. Rabi oscillations in a large josephson-junction qubit. *Phys. Rev. Lett.*, **89**:117901, Aug 2002. [62](#)
- [106] YIGAL MEIR AND NED S. WINGREEN. Landauer formula for the current through an interacting electron region. *Phys. Rev. Lett.*, **68**:2512–2515, Apr 1992. [2](#), [32](#), [41](#)
- [107] KLAUS MØLMER AND YVAN CASTIN. Monte carlo wavefunctions in quantum optics. *Quantum and Semiclassical Optics: Journal of the European Optical Society Part B*, **8**[1]:49, 1996. [99](#)
- [108] KLAUS MØLMER, YVAN CASTIN, AND JEAN DALIBARD. Monte carlo wavefunction method in quantum optics. *J. Opt. Soc. Am. B*, **10**[3]:524–538, Mar 1993. [99](#)
- [109] V. MOURIK, K. ZUO, S. M. FROLOV, S. R. PLISSARD, E. P. A. M. BAKKERS, AND L. P. KOUWENHOVEN. Signatures of majorana fermions in hybrid superconductor-semiconductor nanowire devices. *Science*, **336**:1003, 2012. [2](#), [6](#), [31](#), [70](#)

- [110] KYOKO NAKADA, MITSUTAKA FUJITA, GENE DRESSELHAUS, AND MILDRED S. DRESSELHAUS. Edge state in graphene ribbons: Nanometer size effect and edge shape dependence. *Phys. Rev. B*, **54**:17954–17961, Dec 1996. [7](#)
- [111] V. NALITOV, A. D. SOLNYSHKOV, D. AND G. MALPUECH. Polariton \mathbb{Z} topological insulator. *Phys. Rev. Lett.*, **114**:116401, Mar 2015. [71](#)
- [112] P. D. NATION, J. R. JOHANSSON, M. P. BLENCOWE, AND FRANCO NORI. *Colloquium* : Stimulating uncertainty: Amplifying the quantum vacuum with superconducting circuits. *Rev. Mod. Phys.*, **84**:1–24, Jan 2012. [57](#)
- [113] CHETAN NAYAK, STEVEN H. SIMON, ADY STERN, MICHAEL FREEDMAN, AND SANKAR DAS SARMA. Non-abelian anyons and topological quantum computation. *Rev. Mod. Phys.*, **80**:1083–1159, Sep 2008. [1](#), [7](#)
- [114] M. NEELEY, R. C. BIALCZAK, M. LENANDER, E. LUCERO, M. MARIANTONI, A. D. O’CONNELL, D. SANK, H. WANG, M. WEIDES, J. WENNER, Y. YIN, T. YAMAMOTO, A. N. CLELAND, AND J. M. MARTINIS. Generation of three-qubit entangled states using superconducting phase qubits. *Nature*, **467**:570, 2010. [3](#), [57](#)
- [115] P. NEUMANN, J. BECK, M. STEINER, F. REMPP, H. FEDDER, P. R. HEMMER, J. WRACHTRUP, AND F. JELEZKO. Single-shot readout of a single nuclear spin. *Science*, **329**:542, 2010. [57](#)
- [116] P. NEUMANN, N. MIZUOCHI, F. REMPP, P. HEMMER, H. WATANABE, S. YAMASAKI, V. JACQUES, T. GAEBEL, F. JELEZKO, AND J. WRACHTRUP. Multipartite entanglement among single spins in diamond. *Science*, **320**:1326, 2008. [69](#)
- [117] S. NGUYEN, H. D. GERACE, I. CARUSOTTO, D. SANVITTO, E. GALOPIN, A. LEMAÎTRE, I. SAGNES, J. BLOCH, AND A. AMO. Acoustic black hole in a stationary hydrodynamic flow of microcavity polaritons. *Phys. Rev. Lett.*, **114**:036402, Jan 2015. [71](#)
- [118] A. NUNNENKAMP, J. KOCH, AND S. M. GIRVIN. Synthetic gauge fields and homodyne transmission in jaynescumming lattices. *New Journal of Physics*, **13**:095008, 2011. [3](#), [57](#), [62](#), [66](#)

- [119] YUVAL OREG, GIL REFAEL, AND FELIX VON OPPEN. Helical liquids and majorana bound states in quantum wires. *Phys. Rev. Lett.*, **105**:177002, Oct 2010. [1](#), [6](#), [31](#)
- [120] T. P. ORLANDO, J. E. MOOIJ, LIN TIAN, CASPAR H. VAN DER WAL, L. S. LEVITOV, SETH LLOYD, AND J. J. MAZO. Superconducting persistent-current qubit. *Phys. Rev. B*, **60**:15398–15413, Dec 1999. [58](#), [59](#)
- [121] BORJA PEROPADRE, DAVID ZUECO, FRIEDRICH WULSCHNER, FRANK DEPPE, ACHIM MARX, RUDOLF GROSS, AND JUAN JOSÉ GARCÍA-RIPOLL. Tunable coupling engineering between superconducting resonators: From sidebands to effective gauge fields. *Phys. Rev. B*, **87**:134504, Apr 2013. [66](#)
- [122] FALKO PIENKA, GRAHAM KELLS, ALESSANDRO ROMITO, PIET W. BROUWER, AND FELIX VON OPPEN. Enhanced zero-bias majorana peak in the differential tunneling conductance of disordered multisubband quantum-wire/superconductor junctions. *Phys. Rev. Lett.*, **109**:227006, Nov 2012. [2](#)
- [123] M. B. PLENIO AND P. L. KNIGHT. The quantum-jump approach to dissipative dynamics in quantum optics. *Rev. Mod. Phys.*, **70**:101–144, Jan 1998. [3](#), [67](#)
- [124] J. RAFTERY, D. SADRI, S. SCHMIDT, H.E. TÜRECI, AND A.A. HOUCK. Observation of a dissipation-induced classical to quantum transition. *Phys. Rev. X*, **4**:031043, Sep 2014. [3](#), [56](#), [71](#)
- [125] N. READ AND DMITRY GREEN. Paired states of fermions in two dimensions with breaking of parity and time-reversal symmetries and the fractional quantum hall effect. *Phys. Rev. B*, **61**:10267–10297, Apr 2000. [1](#), [6](#), [31](#)
- [126] S. SARKOZY, F. SFIGAKIS, K. DAS GUPTA, I. FARRER, D. A. RITCHIE, G. A. C. JONES, AND M. PEPPER. Zero-bias anomaly in quantum wires. *Phys. Rev. B*, **79**:161307, Apr 2009. [43](#)
- [127] SATOSHI SASAKI, M. KRIENER, KOUJI SEGAWA, KEIJI YADA, YUKIO TANAKA, MASATOSHI SATO, AND YOICHI ANDO. Topological superconductivity in $\text{Cu}_x\text{Bi}_2\text{Se}_3$. *Phys. Rev. Lett.*, **107**:217001, Nov 2011. [6](#), [70](#)
- [128] MASATOSHI SATO AND SATOSHI FUJIMOTO. Topological phases of noncentrosymmetric superconductors: Edge states, majorana fermions, and non-abelian statistics. *Phys. Rev. B*, **79**:094504, Mar 2009. [17](#)

- [129] MASATOSHI SATO AND SATOSHI FUJIMOTO. Existence of majorana fermions and topological order in nodal superconductors with spin-orbit interactions in external magnetic fields. *Phys. Rev. Lett.*, **105**:217001, Nov 2010. [6](#)
- [130] MASATOSHI SATO, YOSHIRO TAKAHASHI, AND SATOSHI FUJIMOTO. Non-abelian topological order in *s*-wave superfluids of ultracold fermionic atoms. *Phys. Rev. Lett.*, **103**:020401, Jul 2009. [31](#)
- [131] MASATOSHI SATO, YOSHIRO TAKAHASHI, AND SATOSHI FUJIMOTO. Non-abelian topological orders and majorana fermions in spin-singlet superconductors. *Phys. Rev. B*, **82**:134521, Oct 2010. [1](#), [6](#), [19](#), [20](#), [21](#), [23](#), [24](#), [31](#)
- [132] MASATOSHI SATO, YUKIO TANAKA, KEIJI YADA, AND TAKEHITO YOKOYAMA. Topology of andreev bound states with flat dispersion. *Phys. Rev. B*, **83**:224511, Jun 2011. [1](#), [6](#), [7](#), [13](#)
- [133] JAY D. SAU, B. I. HALPERIN, K. FLENSBERG, AND S. DAS SARMA. Number conserving theory for topologically protected degeneracy in one-dimensional fermions. *Phys. Rev. B*, **84**:144509, Oct 2011. [32](#), [46](#)
- [134] JAY D. SAU, ROMAN M. LUTCHYN, SUMANTA TEWARI, AND S. DAS SARMA. Generic new platform for topological quantum computation using semiconductor heterostructures. *Phys. Rev. Lett.*, **104**:040502, Jan 2010. [1](#), [6](#), [31](#)
- [135] JAY D. SAU, SUMANTA TEWARI, ROMAN M. LUTCHYN, TUDOR D. STANESCU, AND S. DAS SARMA. Non-abelian quantum order in spin-orbit-coupled semiconductors: Search for topological majorana particles in solid-state systems. *Phys. Rev. B*, **82**:214509, Dec 2010. [2](#)
- [136] S. SCHMIDT AND G. BLATTER. Strong coupling theory for the jaynes-cummings-hubbard model. *Phys. Rev. Lett.*, **103**:086403, Aug 2009. [56](#)
- [137] S. SCHMIDT, D. GERACE, A. A. HOUCK, G. BLATTER, AND H. E. TÜRECI. Nonequilibrium delocalization-localization transition of photons in circuit quantum electrodynamics. *Phys. Rev. B*, **82**:100507, Sep 2010. [56](#)
- [138] SEBASTIAN SCHMIDT AND JENS KOCH. Circuit qed lattices: Towards quantum simulation with superconducting circuits. *Annalen der Physik*, **525**[6]:395–412, 2013. [3](#)

- [139] ANDREAS P. SCHNYDER AND SHINSEI RYU. Topological phases and surface flat bands in superconductors without inversion symmetry. *Phys. Rev. B*, **84**:060504, Aug 2011. [1](#), [6](#), [7](#)
- [140] R. J. SCHOELKOPF AND S. M. GIRVIN. Wiring up quantum systems. *Nature*, **451**:664, 2008. [57](#)
- [141] D. I. SCHUSTER, A. A. HOUCK, J. A. SCHREIER, A. WALLRAFF, J. M. GAMBETTA, A. BLAIS, L. FRUNZIO, J. MAJER, B. JOHNSON, M. H. DEVORET, S. M. GIRVIN, AND R. J. SCHOELKOPF. Resolving photon number states in a superconducting circuit. *Nature*, **445**:515, 2007. [4](#), [69](#)
- [142] K. SENGUPTA, IGOR ŽUTIĆ, HYOK-JON KWON, VICTOR M. YAKOVENKO, AND S. DAS SARMA. Midgap edge states and pairing symmetry of quasi-one-dimensional organic superconductors. *Phys. Rev. B*, **63**:144531, Mar 2001. [2](#)
- [143] L. Y. L. SHEN AND J. M. ROWELL. Zero-bias tunneling anomalies—temperature, voltage, and magnetic field dependence. *Phys. Rev.*, **165**:566–577, Jan 1968. [41](#), [43](#)
- [144] Ö. O. SOYKAL AND CHARLES TAHAN. Toward engineered quantum many-body phonon systems. *Phys. Rev. B*, **88**:134511, Oct 2013. [4](#), [69](#)
- [145] E. M. STOUDENMIRE, JASON ALICEA, OLEG A. STARYKH, AND MATTHEW P.A. FISHER. Interaction effects in topological superconducting wires supporting majorana fermions. *Phys. Rev. B*, **84**:014503, Jul 2011. [32](#), [33](#)
- [146] YUKIO TANAKA, YOSHIHIRO MIZUNO, TAKEHITO YOKOYAMA, KEIJI YADA, AND MASATOSHI SATO. Anomalous andreev bound state in noncentrosymmetric superconductors. *Phys. Rev. Lett.*, **105**:097002, Aug 2010. [1](#), [6](#)
- [147] SUMANTA TEWARI AND JAY D. SAU. Topological invariants for spin-orbit coupled superconductor nanowires. *Phys. Rev. Lett.*, **109**:150408, Oct 2012. [6](#), [13](#), [22](#)
- [148] D. J. THOULESS, M. KOHMOTO, M. P. NIGHTINGALE, AND M. DEN NIJS. Quantized hall conductance in a two-dimensional periodic potential. *Phys. Rev. Lett.*, **49**:405–408, Aug 1982. [6](#)
- [149] A. TOMADIN, V. GIOVANNETTI, R. FAZIO, D. GERACE, I. CARUSOTTO, H. E. TÜRECI, AND A. IMAMOGLU. Signatures of the superfluid-insulator phase transition in laser-driven dissipative nonlinear cavity arrays. *Phys. Rev. A*, **81**:061801, Jun 2010. [4](#), [69](#)

- [150] YAROSLAV TSERKOVNYAK, BERTRAND I. HALPERIN, OPHIR M. AUSLAENDER, AND AMIR YACOBY. Interference and zero-bias anomaly in tunneling between luttinger-liquid wires. *Phys. Rev. B*, **68**:125312, Sep 2003. [43](#)
- [151] DIMITRIS I. TSOMOKOS, SAHEL ASHHAB, AND FRANCO NORI. Using superconducting qubit circuits to engineer exotic lattice systems. *Phys. Rev. A*, **82**:052311, Nov 2010. [3](#), [68](#)
- [152] J. TWAMLEY AND S. D. BARRETT. Superconducting cavity bus for single nitrogen-vacancy defect centers in diamond. *Phys. Rev. B*, **81**:241202, Jun 2010. [58](#), [59](#)
- [153] D. L. UNDERWOOD, W. E. SHANKS, JENS KOCH, AND A. A. HOUCK. Low-disorder microwave cavity lattices for quantum simulation with photons. *Phys. Rev. A*, **86**:023837, Aug 2012. [3](#), [57](#), [62](#), [69](#)
- [154] W. G. VAN DER WIEL, S. DE FRANCESCHI, T. FUJISAWA, J. M. ELZERMAN, S. TARUCHA, AND L. P. KOUWENHOVEN. The kondo effect in the unitary limit. *Science*, **289**:2105, 2000. [41](#), [43](#)
- [155] D. VAN OOSTEN, P. VAN DER STRATEN, AND H. T. C. STOOF. Quantum phases in an optical lattice. *Phys. Rev. A*, **63**:053601, Apr 2001. [63](#)
- [156] D. VAN OOSTEN, P. VAN DER STRATEN, AND H. T. C. STOOF. Mott insulators in an optical lattice with high filling factors. *Phys. Rev. A*, **67**:033606, Mar 2003. [63](#)
- [157] A. VEDYAYEV, N. RYZHANOVA, N. STRELKOV, AND B. DIENY. Spontaneous anomalous and spin hall effects due to spin-orbit scattering of evanescent wave functions in magnetic tunnel junctions. *Phys. Rev. Lett.*, **110**:247204, Jun 2013. [71](#)
- [158] G. E. VOLOVIK. *Exotic Properties of Superfluid ^3He* . World Scientific, 1992. [6](#)
- [159] G.E. VOLOVIK. Flat band in the core of topological defects: Bulk-vortex correspondence in topological superfluids with fermi points. *JETP Letters*, **93**[2]:66–69, 2011. [7](#)
- [160] A. WALLRAFF, D. I. SCHUSTER, A. BLAIS, L. FRUNZIO, R.-S. HUANG, J. MAJER, S. KUMAR, S. M. GIRVIN, AND R. J. SCHOELKOPF. Strong coupling of a

- single photon to a superconducting qubit using circuit quantum electrodynamics. *Nature*, **431**:162, 2004. [3](#), [56](#), [69](#), [71](#)
- [161] FA WANG AND DUNG-HAI LEE. Topological relation between bulk gap nodes and surface bound states: Application to iron-based superconductors. *Phys. Rev. B*, **86**:094512, Sep 2012. [14](#)
- [162] LUZIE WEITHOFER, PATRIK RECHER, AND THOMAS L. SCHMIDT. Electron transport in multiterminal networks of majorana bound states. *Phys. Rev. B*, **90**:205416, Nov 2014. [71](#)
- [163] XIAO-GANG WEN. Topological order: From long-range entangled quantum matter to a unified origin of light and electrons. *ISRN Condensed Matter Physics*, **2013**:198710. [1](#)
- [164] J. R. WILLIAMS, A. J. BESTWICK, P. GALLAGHER, SEUNG SAE HONG, Y. CUI, ANDREW S. BLEICH, J. G. ANALYTIS, I. R. FISHER, AND D. GOLDHABER-GORDON. Unconventional josephson effect in hybrid superconductor-topological insulator devices. *Phys. Rev. Lett.*, **109**:056803, Jul 2012. [6](#), [70](#)
- [165] ROLAND WINKLER. *Spin-Orbit Coupling Effects in Two-Dimensional Electron and Hole Systems*. Springer-Verlag Berlin Heidelberg, 2003. [8](#)
- [166] CHRIS L. M. WONG, JIE LIU, K. T. LAW, AND PATRICK A. LEE. Majorana flat bands and unidirectional majorana edge states in gapless topological superconductors. *Phys. Rev. B*, **88**:060504, Aug 2013. [1](#), [6](#), [22](#), [31](#)
- [167] W. L. YANG, ZHANG-QI YIN, Z. X. CHEN, SU-PENG KOU, M. FENG, AND C. H. OH. Quantum simulation of an artificial abelian gauge field using nitrogen-vacancy-center ensembles coupled to superconducting resonators. *Phys. Rev. A*, **86**:012307, Jul 2012. [3](#), [56](#), [71](#)
- [168] J. Q. YOU AND F. NORI. Atomic physics and quantum optics using superconducting circuits. *Nature*, **474**:589, 2011. [57](#)
- [169] JIA-BIN YOU, A. H. CHAN, C. H. OH, AND VLATKO VEDRAL. Topological quantum phase transitions in the spincinglet superconductor with rashba and dresselhaus (110) spincorbid couplings. *Annals of Physics*, **349**:189, 2014. [31](#), [33](#)

- [170] JIABIN YOU, C. H. OH, AND VLATKO VEDRAL. Majorana fermions in s -wave noncentrosymmetric superconductor with dresselhaus (110) spin-orbit coupling. *Phys. Rev. B*, **87**:054501, Feb 2013. [6](#), [31](#), [33](#)
- [171] Y. YU, S. HAN, X. CHU, S.-I. CHU, AND Z. WANG. Coherent temporal oscillations of macroscopic quantum states in a josephson junction. *Science*, **296**:889, 2002. [62](#)
- [172] A. M. ZAGOSKIN, S. ASHHAB, J. R. JOHANSSON, AND FRANCO NORI. Quantum two-level systems in josephson junctions as naturally formed qubits. *Phys. Rev. Lett.*, **97**:077001, Aug 2006. [62](#)
- [173] A. ZAZUNOV, A. LEVY YEYATI, AND R. EGGER. Coulomb blockade of majorana-fermion-induced transport. *Phys. Rev. B*, **84**:165440, Oct 2011. [2](#), [32](#)
- [174] X. ZHU, S. SAITO, A. KEMP, K. KAKUYANAGI, S.-I. KARIMOTO, H. NAKANO, W. J. MUNRO, Y. TOKURA, M. S. EVERITT, K. NEMOTO, M. KASU, N. MIZUOCHI, AND K. SEMBA. Coherent coupling of a superconducting flux qubit to an electron spin ensemble in diamond. *Nature*, **478**:221, 2011. [57](#)
- [175] BJÖRN ZOCHER AND BERND ROSENOW. Modulation of majorana-induced current cross-correlations by quantum dots. *Phys. Rev. Lett.*, **111**:036802, Jul 2013. [2](#), [32](#)